Understanding the Lunar Deformations: Insights from Impact Cratering, Magmatism, and Tectonism

A thesis submitted in partial fulfilment of
the requirements for the degree of

Doctor of Philosophy

by

Kimi Khungree Basumatary
(Roll No. 19330009)

Under the guidance of

Dr. Vijayan S
Associate Professor
Planetary Sciences Division
Physical Research Laboratory, Ahmedabad, India.

Discipline of Earth Sciences
Indian Institute of Technology, Gandhinagar
2024

Dedicated

to

"My Family"

"Everyone who helped make this journey possible"

"Those who gaze beyond the surface into unseen realms"

Declaration

I declare that this written submission represents my ideas in my own words, and where others' ideas or words have been included, I have adequately cited and referenced the original sources. I also declare that I have adhered to all principles of academic honesty and integrity and have not misrepresented, fabricated, or falsified any idea, data, fact, or source in my submission. I understand that any violation of the above will be cause for disciplinary action by the Institute and can also evoke penal action from the sources that have thus not been properly cited or from whom proper permission has not been taken when needed.

Date: 21-04-2025

(Signature)
Kimi Khungree Basumatary
(Roll No. 19330009)

Certificate

I hereby certify that **Ms. Kimi Khungree Basumatary** (Roll no: 19330009) conducted the research presented in the thesis titled **"Understanding the Lunar Deformations: Insights from Impact Cratering, Magmatism, and Tectonism"** under my supervision. I confirm that this work has not been submitted elsewhere for any other degree. Having thoroughly examined this dissertation, I believe it meets the necessary standards in terms of scope and quality for the award of the Doctor of Philosophy degree.

Date: 21-04-2025

(Signature)
Dr. Vijayan S
Associate Professor
Planetary Sciences Division,
Physical Research Laboratory,
Ahmedabad, India.
(Thesis Supervisor)

List of Publications

Thesis Related Publications

1. **Kimi, K. B.**, Vijayan, S., Sharini, K. S., Harish, Tuhi, S., Chavan, A., & Priya, R. K. S. (**2025**). Recent tectonic activity in and around the Posidonius crater, Moon. **Journal of Geophysical Research: Planets**, 130, e2024JE008446. https://doi.org/10.1029/2024JE008446

2. **Kimi, K. B.**, Harish, K. S. Sharini, Anil Chavan, Vijayan, S. ”Deformation of the Gruithuisen region lava tube under compressional stress on the Moon.” **Geology** 52, no. 8 (**2024**): 625-630. https://doi.org/10.1130/G52143.1

3. **Kimi, K. B.**, Harish, Vijayan, S. ”Mare filled craters on the Moon.” **Icarus**, 390 (**2023**): 115298. https://doi.org/10.1016/j.icarus.2022.115298

Other Publications

1. Vijayan, S., **Kimi, K. B.**, Anil Chavan, R. Aditi, U. Thahira, V. Rama Subramanian, Rishitosh K. Sinha et al. ”Chandrayaan-3 landing site evolution by South Pole-Aitken basin and other impact craters.” **Icarus** 425 (**2025**): 116329. https://doi.org/10.1016/j.icarus.2024.116329

2. Harish, **Kimi, K. B.**, S. Tuhi, S. Baliyan, N. Mangold, S. Vijayan, and M. R. El-Maarry. ”Shallow subsurface basalt layer along Cerberus Fossae, Mars: Insights from SHARAD, HiRISE, and CRISM analysis.” **Icarus** 391 (**2023**): 115343. https://doi.org/10.1016/j.icarus.2022.115343

3. Vijayan, S., Harish, **Kimi, K. B.**, S. Tuhi, K. Vigneshwaran, R. K. Sinha, S. J. Conway, B. Sivaraman, and Anil Bhardwaj. ”Boulder fall Ejecta: present day activity on Mars.” **Geophysical Research Letters** 49, no. 1 (**2022**): e2021GL096808. https://doi.org/10.1029/2021GL096808

4. Tuhi, S., Harish, **Kimi, K. B.**, K. Vigneshwaran, K. S. Sharini, R. K. S. Priya, and S. Vijayan. ”Ma’adim Vallis, Mars: Insights into episodic and late-stage water activity from an impact crater.” **Icarus** 387 (**2022**): 115214. https://doi.org/10.1016/j.icarus.2022.115214

Acknowledgements

The accomplishment of this thesis would not have been possible without the assistance and encouragement of numerous individuals. I wish to extend my heartfelt gratitude to each one of them.

First and foremost, I would like to express my heartfelt gratitude to my supervisor, Dr. Vijayan S., for his unwavering support, guidance, and mentorship throughout the entire journey of completing my thesis. His knowledge, support, and valuable perspectives have played a crucial role in influencing the focus and excellence of my research. Furthermore, I am grateful for his conviction in my abilities and continuous encouragement to explore challenging ideas, which have served as a source of encouragement and inspiration throughout this journey.

I am deeply thankful to my teammates—Dr. Harish, Dr. Anil Chavan, K.S. Sharini, S. Tuhi and Rishav Sahoo for engaging in insightful discussions, even during unconventional hours, and for their valuable assistance in my research.

I extend my sincere thanks to the Doctoral Scientific Committee (DSC) members—Prof. Anil D. Shukla, Dr. Amit Basu Sarbadhikari, and Dr. Neeraj Srivastava for their review and invaluable feedback on my research work.

I am extremely grateful to Swagatika, Birendra, Vineet, Mansi, Jeet, Vikas, Belligraham, and Usha for standing by me through thick and thin. I am also grateful for the wonderful circle of friends, seniors, and juniors—Santunu, Neha, Saumya, Kshitij, Gourav, Bijoy, Vardan, Tania, Bharti, Ajayeta, Yogesh, Satyam, Tanu, Atif, Amit, Partha, Alka, Shivani, Subham, Deepali, Akansha, Supriya, Siddhartha, Deva, Narendra, Varsha, Kiran, Trinesh, *Aditya, and Dibyendu. After long days of work, being able to unwind by hanging out and chatting with them adds an extra layer of joy to this journey.*

I cherish my family for their boundless love, understanding, and encouragement. Their unwavering belief in my abilities and their sacrifices have been the cornerstones of my academic pursuit. I also extend my gratitude to my cherished pet, Julee, for being a vital part of my life and adding joy to my happy moments.

I am thankful to Dr. Samir V. Dani for his attentive care and medical advice during my recovery.

I would like to extend my gratitude to everyone who has played a role, big or small, in this academic endeavour. Your support has been invaluable, and I am truly thankful for the collective effort that has contributed to the completion of this thesis.

(Kimi Khungree Basumatary)

Abstract

The lunar crust has undergone significant deformation and shaping primarily due to impact cratering, magmatism, and tectonism since its formation. These processes contribute to deformation both individually and through their interactions. Previous studies have examined interactions such as the formation of floor-fractured craters (FFCs) resulting from the interaction between impact craters and magmatism; localized tectonism controlled by magmatism in impact basins; and tectonism in impact basins leading to magma eruptions. These studies have provided valuable insights into complex surface deformations and subsurface structures. This thesis work focuses on the interactions necessary to understand the resulting complex surface deformations and subsurface structures.

Significant milestones have been achieved in lunar science, including human landings, robotic missions, and orbital exploration. Extensive efforts have been dedicated to unravelling the mysteries of the lunar surface and subsurface. Despite these concerted efforts, our understanding of surface and subsurface deformation remains incomplete. A significant portion of the lunar subsurface remains wrapped in mystery. Surface and subsurface deformation are primarily linked to impact cratering, magmatism, and tectonism. Investigating the interactions between these processes is crucial for comprehending surface deformation and the dynamics of the lunar subsurface on various scales, from major to minor. However, studies on these interactions are relatively scarce. This study is motivated by the outlook that these interactions have significantly influenced the complex deformation of lunar surfaces and offer an indirect approach to uncovering subsurface dynamics across different scales.

First, the interaction between impact craters and magmatism was explored by examining craters filled with mare, known as mare-filled craters. Morphometric analysis was employed to achieve this objective. A total of 324

mare-filled craters, whose diameter ranges from ~4 km to ~270 km, were investigated. The study revealed that 1) crater morphology varies depending on the extent of lava infilling and intrusion; 2) impact-induced fractures, possibly associated with dike and deep-seated fractures, facilitate the ascent of magma to the crater floors; and 3) potential sites for shallow, stalled magma reservoirs were identified.

Second, the interaction of impact craters, magmatism, and tectonism was explored. For this study, a mare-filled Posidonius crater was selected. This choice is motivated by two primary factors: first, our prior investigation in a previous study has provided us with a comprehensive understanding of the interaction between impact craters and magmatism in the Posidonius crater; and second, the presence of unique tectonic features—wrinkle ridges and lobate scarps resulting from tectonism along with mare infilling within this crater. The coexistence of these features in the Posidonius crater makes it an ideal location for extensive examination and analysis of the complex interaction among these three geological processes. A morphometric analysis was employed to achieve this objective. This study revealed that 1) the deep-seated fractures likely deformed the western floor and served as a pathway for the multiple stages of volcanism (~3.1 Ga) and intrusive magmatism, leading to slumping on the crater's eastern wall; 2) these fractures plausibly reactivated, forming these tectonic features–wrinkle ridges, lobate scarps, splay faults, and deformed small-size craters, during the Eratosthenian period and continuing into the Copernican period; 3) small-scale graben on the western floor were formed by flexural bending resulting from the reactivation of this fault rather than the previously proposed magma intrusion uplift; and 4) Rimae Posidonius is possibly shaped by complex tectonic adjustments.

Third, the interaction between magmatism, particularly a volcanic feature such as a lava tube, and tectonism was investigated. The Gruithuisen region was chosen for investigation because it contains collapsed pit chains and wrinkle ridges, both of which indicate the presence of lava tubes and tectonic activity in the area. A combination of numerical simulations and morphometric analysis was employed to achieve this objective. This study revealed: 1) the occurrence of unique morphological features in a lava tube due to deformation caused by varying compressional tectonic stress, leading to insights into potential morphological changes in lunar lava tubes under

compressional tectonic stress; and 2) the resemblance of an intact lava tube to a wrinkle ridge, emphasising the importance of exercising caution when differentiating between a lava tube and a wrinkle ridge.

Overall, this thesis work advances the understanding of the interactions among impact cratering, magmatism, and tectonism, providing new insights into associated complex surface deformations and subsurface features, such as impact fractures, shallow magma reservoirs, splay faulting, and lava tube deformation. Its implications extend beyond lunar exploration, presenting a valuable case for studying similar phenomena on other planetary bodies. This research holds particular significance for scholars seeking to unravel the complexities of such interactions and will contribute to upcoming lunar expeditions.

Keywords: The Moon, Geological Interactions, Deformation, Mare-Filled Craters, Wrinkle ridge, Lobate scarp, Small-scale graben, Lava tube.

Contents

List of Figures

List of Tables

Chapter 1

Introduction

Complex geological deformations due to impact cratering, magmatism, and tectonism have played a key role in shaping the evolutionary path of planetary surfaces over time. However, comprehending such complex deformation over time is particularly challenging on the Earth, given its active plate tectonics, which continuously recycles plates alongside fluvial erosion. Similarly, Mars presents difficulties due to past fluvial erosion and substantial dust coverage, and other planetary bodies like Mercury and Venus are hindered by data availability. Conversely, the Moon, characterised by its single-plate structure (Solomon, 1978), lacks plate recycling, fluvial erosion, and extensive dust cover, has retained a detailed record of these deformations and offers a unique platform for investigating complex deformation processes over approximately four billion years (Maurice et al., 2020) since its formation. Enhanced by comprehensive data gathered from manned and unmanned missions, the Moon offers a podium for advancing our understanding of complex geological deformations.

The lunar crust has undergone complex deformation through different geological processes since its formation. These include both exogenic processes, such as impact cratering (Melosh, 1989), and endogenic processes, like magmatism (Wilson and Head III, 1981; Wilson and Head, 2017). Furthermore, the combination of endogenic and exogenic tectonic processes has also shaped the Moon's surface (Heiken et al., 1991; Watters et al., 2015). This chapter will discuss these three geological processes: impact cratering, magmatism, and tectonism on the Moon and their interactions that have prominently shaped the lunar surface. Following this, the motivations and objectives of the thesis, the study area chosen, and the thesis outline will be discussed in detail.

1.1 Impact Cratering

The lunar surface is engraved by more than two million impact craters larger than 1 km in diameter (Robbins, 2019). Overall, the Moon exhibits a wide range of crater sizes, from micrometre-scale to large impact basins measuring up to ∼2500 km in diameter. The size and morphology of these craters are determined by a combination of the gravitational force, target properties, projectile properties and velocity (Cintala et al., 1977; Melosh, 1989; Bray et al., 2008; Silber et al., 2017). These impact craters are classified into three types based on their morphological features: simple craters, complex craters, and basins. Simple craters typically exhibit bowl-shaped depressions with flat floors (Melosh, 1989; Melosh and Ivanov, 1999). With increasing diameter, simple craters evolve into complex craters, which are characterised by terraced walls, peaks, and generally flat floors (Melosh, 1989; Melosh and Ivanov, 1999). On the Moon, craters with diameters of ⩽15 km typically exhibit the characteristics of simple craters, and the transition from simple to complex craters occurs at ∼15 km to 25 km in diameter (Melosh, 1989; Melosh and Ivanov, 1999; Krüger et al., 2018). The depth of both the simple and complex craters increases with an increase in crater diameter, although the depth of complex craters increases at a slower rate compared to simple craters (Melosh, 1989; Melosh and Ivanov, 1999). The craters with inner ring mark the transition from craters to basins, which start at ∼140 km in diameter on the Moon (Hartmann and Wood, 1971; Spudis, 1993; Baker et al., 2011). Basins are further categorised into three categories based on their morphological features: the central-peak basin, whose central peak is surrounded by a ring and occurs within the diameter range of ∼140-175 km; the peak-ring basin, which has a ring but lacks a central peak and occurs at a range of ∼175- 450 km; and the multiring basin, which has multiple rings and is identified at diameters ⩾400 km on the Moon (Melosh, 1989; Heiken et al., 1991).

The process of formation of impact craters, known as impact cratering, involves transforming the projectile's kinetic energy into shock waves and their propagation through the target, rearward into the projectile, and release waves or rarefaction waves propagation (Melosh, 1989). The cratering process is divided into three distinct stages, each dominated by different mechanisms: contact and compression, excavation, and modification (Melosh, 1989). The following subsections delve into the details of impact cratering:

1.1.1 Contact and Compression Stage

This stage is the first stage of the cratering process, where the projectile travelling at a speed of a few kilometres per second comes into contact with the target surface. As soon as the projectile hits the surface, it starts to penetrate the target, transferring most of the projectile's kinetic energy rapidly to the target. The kinetic energy transforms into shock waves. These shock waves propagate forward into the target material and rearward into the projectile. Within the target material, the shock wave induces particle motion that accelerates the impacted materials radially outward and downward. Simultaneously, the shock waves travelling backwards decelerate the projectile. As the shock wave reaches free surfaces, such as the rear of the projectile or the ground surface, release waves initiate and travel from the back/rear to the front of the projectile, unloading the projectile from the high-pressure states, which can completely shatter, vaporise, or melt the projectile. The moment the release wave reaches the front of the projectile and starts to enter the adjacent target material, the contact/compression stage ends (Melosh, 1989; Heiken et al., 1991; French, 1998; Osinski and Pierazzo, 2013).

1.1.2 Excavation Stage

During this stage, the transient crater is formed through complex interactions between the shock waves and the ground surface. As the contact and compression stage end, the projectile is surrounded by a hemispherical envelope of shock waves that rapidly expand through the target rock. This envelope extends both upward and downward from the point of impact, creating a symmetric excavation flow. In the upper zone, material moves dominantly upward and outward, while at lower levels, it moves downward and outward. This movement quickly forms a bowl-shaped depression called the transient crater, or transient cavity, in the target. On the other hand, shock waves that travel upward and intersect the ground surface are reflected downward as rarefaction or release waves, unloading the target from the high-pressure states and causing shattering and fracturing of the target rock, which is an interest of this study. Fracturing includes both concentric and radial fractures (Polanskey and Ahrens, 1990; Ai, 2006; Senft and Stewart, 2007; Kumar and Kring, 2008). During the reflection of the wave, a portion of the energy from the shock waves is converted into kinetic energy, which ejects rock fragments outward from the impact site. However, there comes a point where the shock and release wave energy can no longer excavate or displace the target rock, and the growth of the transient crater ceases, and the excavation stage ends (Melosh, 1989; Heiken et al., 1991; French, 1998; Osinski and Pierazzo, 2013).

1.1.3 Modification Stage

After the end of the excavation stage, the modification stage begins once the transient crater reaches its maximum size. In this stage, the impact-related changes are influenced by gravity and rock mechanics rather than the shock waves that form the transient crater. The shock waves decay into low-pressure elastic stress waves and no longer play a role in crater development. The modification stage is often considered to end when the significant impact debris ceases falling. However, the modification processes, such as uplift, collapse, and fracturing, continue due to other geological processes—including magmatism and tectonism—along with gravity (Melosh, 1989; Heiken et al., 1991; French, 1998; Osinski and Pierazzo, 2013). This thesis focuses on the modified/ deformed craters on the Moon due to magmatism and tectonic processes. Further details regarding this are in Chapter–3 & 4.

1.2 Magmatism

The collective process of magma generation, ascent, and solidification is known as magmatism (Wilson and Head III, 1981; Marsh and Watts, 2007; Wilson and Head, 2017). Within the Moon, the primary mechanism for magma generation is attributed to heat resulting from the radioactive decay of uranium (U), thorium (Th), and potassium (K), as well as the accretionary heat causing the melting of host rocks (Shearer et al., 2006). The initiation of magma ascent is driven by the buoyancy of magma, which is less dense than the surrounding rocks, or by excess pressure within the magma source, in both cases exerting pressure at the top of the magma source region, initiating the ascent (Wilson and Head, 2017). These magmas are suggested to ascend through various means, including porous flow at ~1 m/year, propagation through brittle dike fractures at a rate of ~4 to 70 m/second, or a combination of porous flow in the asthenosphere and propagating dike in the lithosphere within the Moon (Wilson and Head III, 1981; Richter and McKenzie, 1984; Beck et al., 2006; Shearer et al., 2006; Havlin et al., 2013; Wilson and Head, 2017). Magma that is everywhere buoyant in its host rocks would inevitably reach the surface and can erupt until the supply of magma ceases (Wilson and Head, 2017). However, if the magma is not positively buoyant at all depths, specifically in the crust, it will accumulate and solidify at the subsurface, where neutral buoyancy is achieved (Wilson and Head, 2017). Alternatively, the negatively buoyant magma dike can rely on excess pressure to reach the surface (Wilson and Head, 2017). Most mare basalts, with densities ranging from ~2775 to 3025 kg/m³, exhibit negative buoyancy within the lunar crust, which is approximately 2550 kg/m³ (Wieczorek et al., 2001, 2013). As a result, the excess pressure in the magma source region facilitates the ascent of magma towards the surface (Wilson and Head, 2017). This excess pressure depends on factors such as the vertical extent of the molten rock region (h), the difference in density between the surrounding rocks and the molten rock (ρ_{rock}- ρ_{melt}), and the gravity at that depth (g) (Wilson and Head, 2017). The excess pressures of at least 20–30 MPa are suggested to be present in mantle melts at or below the crust-mantle interface to drive magma to the lunar surface (Wilson and Head, 2017). In addition to the influence of excess pressure, factors like the presence of volatiles and the depth of the source region, where the magma is stalled/ formed, also affect the likelihood of magma ascent towards the surface. Deeper source regions increase the chances of magma eruption (Wilson and Head, 2017). Furthermore, the stress conditions of the surrounding rocks play a crucial role. Tensile stress promotes magma eruption, while compressive stress impedes it (Wilson and Head, 2017).

The process of magmatism, discussed in the preceding paragraph, where magma generates, ascends, and solidifies at the surface is known as volcanism, while accumulation underneath the surface is called plutonism (Wilson and Head, 2017). The dark regions on the surface of the Moon, known as maria, are a product of volcanism resulting from the flowing of lava (Head, 1975). These dark regions cover ~16%-17% of the lunar surface, widely on the nearside and ~1% on the farside (Head, 1975; Nelson et al., 2014). Besides Maria, sinuous rilles, numbering 194 in total, represent another prominent volcanic feature on the lunar surface (Hurwitz et al., 2013). The suggested hypotheses for rille formation include lava flow forming levees as lava cools, directing flow in a constructed channel (Spudis et al., 1988;

Komatsu and Baker, 1992) as well as erosion by lava flow either on the surface, forming channels (Carr, 1974; Williams et al., 2000; Hurwitz et al., 2012) or in subsurface forming lava tubes that subsequently collapsed to form sinuous rille (Greeley, 1971; Hurwitz et al., 2013). Apart from the mare and sinuous rille, this research endeavour is interested in exploring lava tubes. Despite considerable advancements in lunar research, the detailed investigation of lava tubes remains challenging and relatively less explored. The formation of lava tubes can occur through several processes, such as the overcrusting of lava flow channels, where lateral shelf accretion creates a roof over the channel (Peterson et al., 1994). Another method involves over-crusting by welding together solidified lava pieces (slabs) and surrounding rocks (lithoclasts) that float downstream, forming a roof over the flowing lava channel (Peterson et al., 1994). Inflation is another mechanism where pressure from flowing lava builds up beneath a hardened/cooled lava surface, causing the lava to bulge upward to form a lava tube (Hon et al., 1994; Peterson et al., 1994). Inflation can also occur when the front of the flow cools, halts, thickens, and widens, resulting in internal pressure buildup as lava continues to flow steadily but cannot extend beyond the front. This leads to inflation spreading backwards, forming tubes (Calvari and Pinkerton, 1998). Moreover, lava tubes can also develop when lava inflates along deep layers from previous flows (Tonello, 2017) or along fractures and eruptive fissures (Cushing et al., 2015). This inflation erodes downward, enlarging the conduit and creating a tube (Cushing et al., 2015; Tonello, 2017). This thesis aimed to explore the deformation of volcanic features such as sinuous rilles and lava tubes caused by tectonism, as well as the influence of cratering on magmatism, the specifics of which are elucidated in Chapter–3, 4 & 5.

1.3 Tectonism

The process of deformation of the crust of a planetary body is known as tectonism, driven by either exogenic or endogenic forces (Heiken et al., 1991; Watters et al., 2015). Impact cratering is an example of an exogenic force contributing to tectonism (Heiken et al., 1991). Impact cratering deforms the crust by creating variously shaped and sized impact craters, which were discussed in section 1.1. Furthermore, the shock and elastic waves generated during impacts can create new fractures/ faults or reactivate preexisting fractures (Heiken et al., 1991). Magmatism, as discussed in section 1.2, is an example of an endogenic force contributing to tectonism. When extrusion and intrusion occur at the surface and subsurface, it deforms the crust by causing uplifting/ doming, fracturing, and subsidence (Heiken et al., 1991).

The deformation of the lunar crust can also occur by endogenic forces arising from changes in the thermal stress state (Solomon and Chaiken, 1976; Binder and Lange, 1980). As per lunar thermal history models, the Moon's interior remained hot until approximately 3.6–3.8 billion years ago, forcing the Moon to expand, which caused tensional stress in the lunar crust (Solomon and Chaiken, 1976; Binder and Lange, 1980; Solomon and Head, 1980). This tensional stress leads to the formation of normal faulting and large linear openings on a scale of kilometres called grabens, which possibly served as magma plumbing systems for the nearside mare volcanism (Andrews-Hanna et al., 2014). Subsequently, over time, the gradual cooling of the Moon's interior resulted in contraction, generating compressional stress on the lunar crust (Solomon and Chaiken, 1976; Binder and Lange, 1980). This stress is evident in the form of thrust faults, characterised by surface features known as wrinkle ridges and lobate scarps (Watters et al., 2010; Williams et al., 2019). Wrinkle ridges are linear to sinuous features observed on lunar mare (Plescia and Golombek, 1986), while lobate scarps are linear to arcuate features found primarily on lunar highlands, with only a small percentage occurring (∼3%) on lunar mare regions (Watters, 1993; Watters et al., 2015). Approximately 5945 wrinkle ridges have been globally mapped by Thompson et al. (2017), while around 3200 lobate scarps have been mapped by Watters et al. (2015).

In addition to deformation resulting from endogenic thermal stress changes, the lunar crust deformation is influenced by the exogenic forcing arising from Earth's gravitational interaction with the Moon (Melosh, 1980; Collins et al., 2009; Watters et al., 2015). The Moon's gravitational pull on Earth induces tidal bulges in the Earth's oceans (Melosh, 1980; Collins et al., 2009; Watters et al., 2015). These bulges generate tidal forces that decelerate the Moon's orbital motion and rotation (despinning) (Melosh, 1980; Collins et al., 2009; Watters et al., 2015). Consequently, the Moon's orbital energy is gradually converted into gravitational potential energy, leading to orbital recession and exerting stresses at a range of ∼20–40 kPa on the lunar crust (Melosh, 1980; Collins et al., 2009; Watters et al., 2015). Similar to Earth's tidal bulges caused by the Moon's gravitational interaction, the Moon also experiences gravitational forces exerted by Earth, resulting in solid-body tides (Collins et al., 2009; Watters et al., 2015). These Earth-induced stress solid-body tides vary on the Moon's crust, with compressional stress ($\leqslant$5 kPa) at apogee and extensional stresses at perigee; these periodic variations in stress experienced by the lunar crust are known as durinal tidal stress (Collins et al., 2009; Watters et al., 2015). Currently, these stresses are insufficient to generate tectonic activity in the lunar crust, based on strength envelopes for near-surface lunar regolith, stresses of $\sim$2–7 MPa are least required to develop shallow thrust faults (Williams et al., 2000; Watters et al., 2015). However, supported by the observation of preferred/ non-random orientations of lobate scarps (Watters et al., 2015) and wrinkle ridges (Nypaver and Thomson, 2022), these stresses are found to influence tectonic patterns in the model study of Watters et al. (2015). The current stress on the lunar crust is suggested to be a combination of global contraction, orbital recession stress, and diurnal tidal stress at apogee (Watters et al., 2015). Global contraction stresses are estimated to be around $\sim$2 MPa, causing tectonic activity, while orbital recession stresses and diurnal stresses influence the orientations of tectonic features (Watters et al., 2015). Additionally, regional variations in stress, induced by differences in material strength and mare-filled impact basins, introduce complexities to the lunar terrain, consequently impacting the orientations of tectonic features (Watters et al., 2015; Lu et al., 2019).

Wrinkle ridges and lobate scarps are surface expressions of movement along the underlying thrust fault during compressional stress. The movement under compressional stress causes uplift and flexural bending, resulting in deformation features such as wrinkle ridges and lobate scarps (Watters et al., 2012). Consequently, the upliftment and flexural bending may generate localised extensional stress, leading to the development of another type of tectonic deformational feature—small-scale grabens (Watters et al., 2012). This thesis focuses on understanding how these tectonic forces deform the impact craters and volcanic features on the Moon, shedding light on their role in shaping lunar terrain. Further information is provided in Chapter–4 & 5.

1.4 Interaction of Cratering, Magmatism, and Tectonism

As discussed in the preceding sections, the lunar crust has undergone deformation due to three primary processes: impact cratering, magmatism, and tectonism. These processes contribute to surface and sub-surface deformation individually and also interact with one another, leading to complex surface and sub-surface deformation. The following subsections discuss the previously studied complex interactions that have contributed to surface deformation.

1.4.1 Magmatism: Reshaping the Crater's Floor

Lunar floor-fractured craters are the result of the interaction of magmatism and impact craters. They are characterised by their shallow floors compared to typical craters observed on the Moon and display a variety of floor fracture patterns, including radial, concentric, and polygonal (Schultz, 1976; Jozwiak et al., 2012). In total, there are 170 lunar craters that exhibit these unique characteristics (Jozwiak et al., 2012). Based on the morphologic and morphometric studies, the accepted hypothesis for the formation of FFCs is magmatic intrusion (Schultz, 1976; Jozwiak et al., 2012, 2015). The FFCs are formed when a propagating dike encounters the breccia region, which has a lower density than the surrounding crustal material, causing the dike to slow down and eventually stop its upward propagation (Wichman and Schultz, 1995; Jozwiak et al., 2015; Wilson and Head, 2018; Walwer et al., 2021). Despite the cessation of upward magma movement, significant pressure can accumulate at the dike's tip (Wichman and Schultz, 1995; Jozwiak et al., 2015; Wilson and Head, 2018; Walwer et al., 2021). If this pressure exceeds the surrounding pressure from the weight of the rock (lithostatic pressure), the magma can start moving horizontally instead of continuing upward, forming a flat intrusion known as a sill (Wichman and Schultz, 1995; Jozwiak et al., 2015; Wilson and Head, 2018; Walwer et al., 2021). The sill continues to propagate horizontally until it reaches the edge of the crater floor region (Wichman and Schultz, 1995; Jozwiak et al., 2015; Wilson and Head, 2018; Walwer et al., 2021). Here, the surrounding rock, the presence of the crater wall and rim, increases the overlying pressure significantly (Wichman and Schultz, 1995; Jozwiak et al., 2015; Wilson and

Head, 2018; Walwer et al., 2021). This increased pressure, combined with the lithostatic pressure, causes the sill to pinch off and stop spreading further (Wichman and Schultz, 1995; Jozwiak et al., 2015; Wilson and Head, 2018; Walwer et al., 2021). In the centre of the crater, where the sill lies beneath the breccia lens, it experiences relatively lower overburden pressure due to the less dense breccia material and the absence of excavated crustal material resulting from the impact event (Wichman and Schultz, 1995; Jozwiak et al., 2015; Wilson and Head, 2018; Walwer et al., 2021). Consequently, the sill tends to grow upward more at the crater's centre than its edges, leading to crater floor deformation by uplift and fracturing of the crater floor (Jozwiak et al., 2015).

1.4.2 Cratering Influencing the Magmatism

Adding to the hypothesis of FFC formation through magma intrusion discussed in section 1.4.1, Thorey and Michaut (2014); Michaut and Pinel (2018) study reveals that the impact craters can influence magma intrusion/extrusion. During the cratering process–excavation stage, the unloading of material from the surface leads to a reduction in the pressure on the rocks surrounding the crater (Michaut and Pinel, 2018). This reduction in pressure provides extra pressure to magma beneath the surface, allowing it to move upwards through the crust (Michaut and Pinel, 2018). In cases where the crust is thin and the crater is large, the pressure reduction on surrounding rocks is significant, providing additional pressure for magma to ascend to the surface and erupt (Michaut and Pinel, 2018). Conversely, if the crater is small or the crust is thick, the pressure reduction due to the cratering may not be sufficient to provide additional pressure for magma to erupt, resulting instead in intrusions below the surface and FFC formation (Michaut and Pinel, 2018).

An alternate mechanism by which cratering influences magmatism is through the generated fractures during impact events. Previous studies have suggested the formation of ring faults within the lunar crust during the formation of impact basins (Hartmann and Kuiper, 1962; Andrews-Hanna et al., 2018). Andrews-Hanna et al. (2018) specifically studied the Orientale basin and found that these deep-rooted ring faults extend from the surface down to at least the base of the crust/ the crust-mantle interface. Typically, these faults are normal faults, providing pathways for magma to ascend and leading to the eruption and infilling of mare materials within the Orientale basin (Nahm et al., 2013) and other large lunar impact basins.

1.4.3 Impact Basins and Magmatism: Governing Localized Tectonism

The infilling of lunar basins with mare basalt leads to subsidence at the basin centre. The weight of the thick mare deposits exerts pressure on the lithosphere beneath, causing it to bend and sink downward. This subsidence results in the formation of wrinkle ridges, which appear in circular patterns within the basin. These wrinkle ridges form as a result of the lithosphere accommodating the downward pressure, creating a compressional region. Meanwhile, extensional features like large-scale grabens emerge on the basin's periphery. These grabens occur as the lithosphere experiences pulled-apart/ extensional stress along the periphery due to subsidence-induced stresses and global extensional horizontal stress. Thus, the interaction between magma infilling, subsidence, and resulting stress patterns produces both compressional and extensional tectonic features within and around mare-filled lunar basins (Melosh, 1978; Solomon and Head, 1980).

1.4.4 Tectonism in Impact Basins: Influencing Magmatism

The impact basin ring's normal faults, which were initially involved in mare infilling (Hartmann and Kuiper, 1962; Nahm et al., 2013; Andrews-Hanna et al., 2018), can be reactivated under compressional stress, leading to the formation of thrust faults (Zhang et al., 2023). These reactivated faults act as pathways for magma ascent from deeper reservoirs towards the lunar surface (Zhang et al., 2023). The presence of magma weakens the faults, making them more susceptible to slipping and complete reactivation under prevailing compressional stress (Zhang et al., 2023). The compressional stress facilitating the reactivation of faults causes folding, resulting in wrinkle ridge and anticline structures–upward folding structures where the oldest rocks are situated in the centre (Zhang et al., 2023). Within these anticlines, magma ascending along the reactivated faults can accumulate (Zhang et al., 2023). The accumulation of magma and flexural bending of the wrinkle ridges can cause local extensional stresses at the crestal zone of an anticline or wrinkle ridge (Zhang et al., 2023). These extensional stresses may cause magma to leak onto the lunar surface, where it erupts and solidifies (Zhang et al., 2023).

1.5 Motivation and Key Objectives

In previous sections 1.1–1.3, the geological processes that have individually played a role in deforming the lunar crust (Wilson and Head III, 1981; Melosh, 1989; Watters et al., 2015; Wilson and Head, 2017) were discussed. Subsequently, in section 1.4, their complex interaction, unravelling how their interplay has further influenced deformation (Hartmann and Kuiper, 1962; Schultz, 1976; Melosh, 1978; Solomon and Head, 1980; Jozwiak et al., 2012; Nahm et al., 2013; Jozwiak et al., 2015; Michaut and Pinel, 2018; Andrews-Hanna et al., 2018; Zhang et al., 2023) were discussed. Studying such surface deformations resulting from interactions has provided valuable insights into subsurface structures, unveiling the presence of fractures and faults (Nahm et al., 2013; Zhang et al., 2023), as well as various magmatic intrusions like sills and laccoliths (Schultz, 1976; Jozwiak et al., 2012).

Over the years, there has been a remarkable advancement in lunar exploration, significantly advancing our understanding of subsurface structures. However, despite these achievements, there still need to be avenues for further progress. The Gravity Recovery and Interior Laboratory (GRAIL) mission, while groundbreaking, is constrained by resolution limitations; it can detect large-scale variations in gravity but faces challenges in detecting smaller-scale features or anomalies, e.g., magma intrusions associated with FFCs $\leqslant$20 km in diameter are unresolvable (Jozwiak et al., 2017). Similarly, data from an orbiter like the Kaguya Lunar Radar Sounder (LRS) offers coarse resolution. Additionally, data gathered by the Ground Penetrating Radar (GPR) onboard the Chang-E 3 rover is restricted to localised regions. Therefore, studying the deformation influenced by complex interactions, as discussed in the above section, offers valuable insights by providing a means to understand subsurface structures at large and small scales. The outlook that these interactions have significantly influenced the complex deformation of lunar surfaces and serve as an indirect approach to uncovering subsurface dynamics at large and small scales has motivated us to pursue this study.

The primary objectives of this thesis are to gain a comprehensive understanding of the complex deformation occurring on the lunar surface and the associated underlying subsurface structures by studying the interaction of three geological processes: impact, magmatism, and tectonism. A detailed outline of the specific sub-goals undertaken to achieve these main objectives is included in the introduction of each chapter (3, 4 & 5).

1.6 Strategic Selection of Study Areas

The selection of the study areas was based on the presence of deformational features arising from geological processes, including impact, magmatism, and tectonism. We specifically looked for areas where two or more types of deformational features were present, each linked to different geological processes. This approach ensured that the chosen area exhibited evidence of being influenced by two or more geological processes. Once this condition was fulfilled, the area was selected for further examination of the interaction processes.

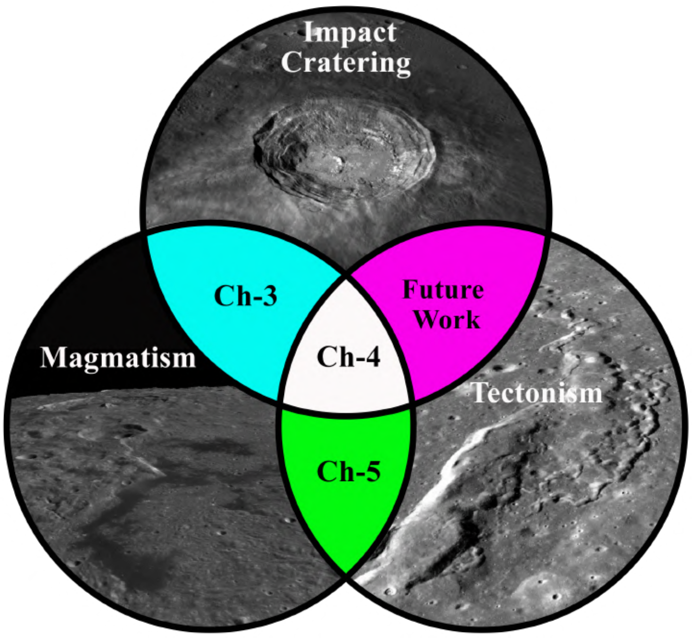

Figure 1.1: The schematic illustrates surface expressions of geological processes: a fresh impact crater for impact cratering, a dark mare patch for magmatism, and a wrinkle ridge for tectonism. Interaction zones between these processes are highlighted in different colours and labelled according to the chapters where they are explained in detail.

In this thesis, three primary areas were focused: first, Mare-filled craters, characterised by lava infillings on the crater floor, provide evidence of both cratering and magmatism processes (Kimi et al. (2023), Chapter–3). Secondly, the Posidonius crater exhibits deformational features such as lava infillings and wrinkle ridges within its floor, showcasing evidence of three geological processes: impact, magmatism, and tectonism (Chapter–4). Thirdly, the Gruithuisen region, which has collapsed lava tubes, indicates volcanic activity, alongside wrinkle ridges indicative of tectonic activity (Chapter–5).

1.7 Thesis Organization

The thesis is organised into six chapters (Figure 1.1). Chapter–1: provides a concise overview of previous studies relevant to the thesis. It thoroughly discusses three geological processes—impact cratering, magmatism, and tectonism—alongside their associated features. It then proceeds with a discussion of the interactions among these processes, followed by a discussion on the motivation and objectives of this study. The chosen study area is introduced, and the chapter concludes with an outline of the thesis. In Chapter–2, detailed information is presented regarding the datasets utilised and the software and methodology employed in this thesis. Chapter–3 provides detailed insight into Mare-filled craters, focusing on the interaction of impact crater–related fractures and magmatism. Chapter–4 offers a thorough exploration of Posidonius crater, focusing on the interaction of impact crater, magmatism, and tectonism. Chapter–5 provides an in-depth examination of the deformation of the Gruithuisen region lava tube, focusing on the interaction between a volcanic feature–lava tube and tectonism. Chapter–6 summarises the results obtained from the three preceding chapters, along with the principal conclusions drawn from this thesis. It also explores future perspectives on impact cratering and tectonism. Additionally, it outlines several relevant scientific questions that have surfaced during the research process and can be pursued in the near future.

Chapter 2

Methodology

To understand the complex interaction processes, this study employed morphometric analysis and 3D simulation. This chapter discusses the details of the datasets and the software used for morphometric analysis and 3D simulation. The initial section discusses the selected imagery and topography datasets relevant to the morphometric analysis, followed by a detailed discussion of the software used in the morphometric analysis and simulation.

2.1 Orbiter Datasets

Over the decades, the evolution of lunar datasets has progressed significantly, transitioning from early telescopic imagery to advanced orbiters. Initially, researchers relied on telescopes for observations, limiting the resolution and coverage of the lunar surface. However, the emergence of lunar exploration, notably through orbiter missions, ushered in a new era marked by the availability of abundant high-resolution imagery, topography datasets, and global coverage. In this study, the finest-resolution images and topography datasets from orbiters currently available were used.

2.1.1 Imagery Data

2.1.1.1 Lunar Reconnaissance Orbiter Camera (LROC)

The Lunar Reconnaissance Orbiter (LRO), with six scientific instruments onboard, includes the Lunar Reconnaissance Orbiter Camera (LROC), which comprises two Narrow Angle Cameras (NACs) and a Wide Angle Camera (WAC). The NACs employ push-broom scanning technology to acquire high-resolution monochrome images at a spatial resolution of ~0.5–2 m/pixel (Robinson et al., 2010). The georeferenced NAC images available at the Planetary Image Locator Tool (PILOT) (https://pilot.wr.usgs.gov/) were used to investigate smaller features.

The WAC, on the other hand, is designed for multispectral imaging and operates in a 7-wavelength push-frame imaging mode with five visible wavelength filters (415 nm, 566 nm, 604 nm, 643 nm, and 689 nm) and two ultraviolet (UV) filters (320 and 360 nm) (Robinson et al., 2010). It has a spatial resolution of ~100 m/pixel for visible imaging and ~400 m/pixel for UV imaging (Robinson et al., 2010). This study used a global mosaic WAC image of spatial resolution ~100 m/pixel at a wavelength of 643 nm (Speyerer et al., 2011) available at https://astrogeology.usgs.gov/search?pmi-target=moon to examine large-scale features.

2.1.1.2 Terrain Mapping Camera-2 (TMC-2)

The Chandrayaan-2 is an integrated orbiter-lander-rover mission. The Chandrayaan-2 Orbiter is equipped with eight different scientific equipment, including the Terrain Mapping Camera-2 (TMC-2), which datasets were utilised in this study. The TMC-2 operates in push-broom mode, capturing panchromatic images within the wavelengths of 400–850 nm at a spatial resolution of ~5 m/pixel (Chowdhury et al., 2020). The data for this study were sourced from archives at the Indian Space Science Data Centre (ISSDC), accessible via https://pradan.issdc.gov.in/ch2/.

2.1.1.3 Terrain Camera (TC)

Initially known as SeLenological and Engineering Explorer (SELENE), now recognised as Kaguya, it is equipped with fifteen scientific instruments, which include a Terrain Camera (TC) capable of high-resolution stereo imaging, achieving a spatial resolution of ~10 m/pixel (Haruyama et al., 2008). The TC employs push-broom scanning technology to capture panchromatic images with a range filter operating within the wavelengths of 430–850 nm (Haruyama et al., 2008). The data used in this study were obtained from the archives available at the PDS Geosciences Node–Orbital Data Explorer, accessible via the following link: https://ode.rsl.wustl.edu/moon/index.aspx.

2.1.2 Topography Data

2.1.2.1 Lunar Orbiter Laser Altimeter (LOLA)

The Lunar Orbiter Laser Altimeter (LOLA) onboard the Lunar Reconnaissance Orbiter (LRO) is utilised to measure the topography of the lunar surface by determining the distances of the round-trip time of laser pulses travelling from the spacecraft to the lunar surface and back (Smith et al., 2010a,b). LOLA operates at a wavelength of 1064.4 nm, emitting laser pulses consistently at a repetition rate of 28 Hz (Smith et al., 2010a). It utilises a multi-beam setup, splitting the laser beam into five distinct outputs, providing comprehensive surface coverage (Smith et al., 2010a). The along-track spatial resolution is ~20 m globally, while the cross-track resolution is ~1.8 km at the equator and ~160 m at 85° latitude (Smith et al., 2010b). The vertical precision of LOLA measurements is ~10 cm, with an accuracy of ~1 m (Smith et al., 2010b; Mazarico et al., 2012). These measurements are then transformed into a Digital Elevation Model (DEM) using Generic Mapping Tools software (Neumann et al., 2011; Wessel et al., 2013). The resulting DEM from LOLA was utilised in this study, accessible at https://astrogeology.usgs.gov/search?pmi-target=moon.

2.1.2.2 SLDEM2015

The LRO–Lunar Orbiter Laser Altimeter (LOLA) and SELENE/Kaguya–Terrain Camera (TC) data were co-registered to create an improved lunar digital elevation model (DEM) known as SLDEM2015, covering latitudes within 60°N/S (Barker et al., 2016). LOLA offers advantages in mapping lunar terrain in regions with poor illumination; however, they have a few–kilometer gap in coverage, particularly near the equator (Barker et al., 2016). On the other hand, Kaguya–TC stereo imaging provides denser surface coverage than LOLA, especially near the equator (Barker et al., 2016). Therefore, co-registering Kaguya–TC imagery enhances the coverage of the LOLA dataset (Barker et al., 2016). SLDEM2015 has a spatial resolution of ~59 m/pixel at the equator and a vertical resolution of ~3 to 4 m (Barker et al., 2016). In the study, SLDEM2015 data up to 60°N/S and LOLA data above 60°N/S, were utilised. The SLDEM2015 utilised in this study is accessible at https://astrogeology.usgs.gov/search?pmi-target=moon.

2.1.2.3 NAC-DTM

The NAC-Digital Terrain Model (DTM) is created from sets of stereo images captured by LROC-NACs (Henriksen et al., 2017). Currently, NACs-DTMs offer the highest accuracy among all topography datasets, with the vertical and horizontal precision of the DTMs being finer than the size of each pixel in the images (∼2 to 5 m) (Henriksen et al., 2017). However, their availability is limited. Therefore, in this study, NACs-DTMs, which were accessible, were utilised. The NACs-DTMs employed in this research are available at https://wms.lroc.asu.edu/lroc.

2.2 Software and Methods

2.2.1 ArcGIS

Arc Geographic Information System (ArcGIS) is a comprehensive geographic information system (GIS) software developed by Environmental Systems Research Institute (Esri). This includes sophisticated applications like ArcMap and ArcScene, which help in geographical data processing and visualisation activities. In this thesis, ArcMap 10.4 was employed for conducting detailed morphometric analysis of various geological features associated with impact cratering, magmatism, and tectonism. Additionally, ArcScene was utilised for creating 3D visualisations, enhancing the understanding of the three-dimensional aspects of these geological features.

2.2.2 Craters Tools and Stats

The absolute age of rocks from planetary bodies other than Earth can only be determined by the radiometric dating of meteorite samples and samples returned by missions. However, this method is constrained by the availability of meteorite samples and the budgetary limitations of missions. Therefore, to address these limitations, researchers developed a relative age dating method known as crater size-frequency distribution (CSFD), which provides an alternative approach to understanding the age of planetary surfaces based on cratering processes. This method is based on the cumulative concept that older surfaces have accumulated a greater number of impact craters over time than younger surfaces (Baldwin, 1971; Hartmann, 1973; Kneissl et al., 2011). To quantify ages using this concept, crater frequency measurements of 1 km-diameter were conducted on orbiter images of the areas where the Apollo and Luna missions gathered samples. The absolute radiometric ages derived from these returned samples were subsequently correlated with the image-based cumulative frequency of crater per area (km^{-2}), resulting in an empirical relationship referred to as the crater chronological function (CF) (Eq: 2.1) (Neukum and Wise, 1976; Neukum, 1983).

$$logN(1) = 5.44 \times 10^{-14}(e^{6.93t} - 1) + 8.38 \times 10^{-4}t \tag{2.1}$$

where N(1) represents the cumulative frequency of impact craters per km^{-2} at diameters equal to 1 kilometre, while t denotes the age measured in billions of years (Ga).

$$logN = \sum_{i=0}^{11} a_i(logD)^i \tag{2.2}$$

where N is the cumulative frequency of impact craters per km^{-2}, a_i is one of eleven production function coefficients, and D is the crater diameter.

The age (t) of the unknown surface can be determined using the crater chronological function (Eq: 2.1), given the cumulative frequency of impact craters per km^{-2} (N) for an unknown surface. Previous studies have correlated N and impact craters of various diameters (D) on various surfaces. Their studies suggested the distribution of craters follows a standard distribution pattern across all surfaces on the Moon. The empirical relationship derived from this correlation between N and D is referred to as the crater production function (PF) (Eq: 2.2) (Neukum et al., 1975; Neukum and Wise, 1976; Neukum, 1984). These two empirical relationships, the CF (Eq: 2.1) and the PF (Eq: 2.2), can be solved graphically to determine the age.

In this study, CraterTools (Kneissl et al., 2011), a software extension for ArcMap, was used to digitise and measure impact craters of various diameters as well as their corresponding areas. The CraterStats software (Michael and Neukum, 2010) was then used to fit the CSFD obtained using CraterTools to a known crater PF (Eq: 2.2). This was followed by the fitting of the CSFD for a certain crater size range to find the best fit with the CF in order to determine an age.

2.2.3 Ansys

Finite Element Analysis (FEA) was used in this study to investigate the deformation of the geological feature. FEA is a numerical approach for solving complicated physical problems by breaking down the structure into a finite number of smaller elements. These elements are joined at nodes, resulting in a mesh that roughly approximates the structure's shape. The ANSYS software was selected for this investigation because of its robust ability to handle complex simulations and produce reliable findings. The built-in Static Structural and Eigenvalue Buckling modules of ANSYS were utilised in the study. These modules help assess the structural response under various stress conditions and identify potential buckling deformation modes, providing valuable insights into the system's deformation.

Chapter 3

Mare-Filled Craters:

Insights from Cratering & Magmatism Interaction

3.1 Introduction

The deformation of crater floors by magmatism provides valuable insights into subsurface structures, revealing various magmatic intrusions such as sills and laccoliths (Schultz, 1976; Jozwiak et al., 2012). Examples of such deformation include mare-filled craters (Schultz, 1976; Schultz and Orphal, 1978) and floor-fractured craters (FFCs) (Schultz, 1976; Schultz and Orphal, 1978; Jozwiak et al., 2012). These craters represent the interaction between impact cratering and magmatism and are commonly found on the Moon and other planetary bodies (Wichman and Schultz, 1993; Bamberg et al., 2014; Buczkowski et al., 2018).

Schultz (1976) classified FFCs into six classes based on the observed characteristics, which were re-examined by Jozwiak et al. (2012). FFCs are characterised by radial, concentric, and polygonal floor fractures and generally have anomalous shallow floors (Schultz, 1976; Jozwiak et al., 2012). Both studies focused mainly on floor fractures in the craters and classified them accordingly. Schultz (1976) suggested infilling occurred through pre-existing deep-seated fractures, and Jozwiak et al. (2015) instead proposed infilling through over-pressurised dikes. Adding to Jozwiak et al. (2015), Michaut and Pinel (2018) proposed that the lava infilling on the floors is due to impact cratering, which causes surface unloading, resulting in over-pressurisation of magma stalled at depth. Michaut and Pinel (2018) studied FFCs with/without infilling and mare-filled craters without fractured floors. They found that lava infilling is preferred in larger-sized craters due to the unloading of more surface material than in smaller ones.

Previous studies have mainly focused on floor fracture craters; however, there has been a lack of detailed studies on the craters filled with mare and FFCs that are mare-filled, known as mare-filled craters. Consequently, a comprehensive study of mare-filled craters is necessary, as it also provides valuable information about the subsurface structures and the deformation of craters. This study aims to understand the following:

1. The extent of lava infilling in the craters to understand the volume occupied by the lava and associated morphological variations.

2. Global distribution for identifying the hotspots of mare-filled craters.

3. Small-size mare-filled craters for identifying potential sites for past shallow magma reservoirs.

4. The ages of the floor of mare-filled craters to gain insight into the period of mare-infilling activity.

3.2 Methodology

3.2.1 Datasets

The Lunar Reconnaissance Orbiter Camera (LROC) Wide Angle Camera (WAC) global mosaic image of spatial resolution ~100 m/pixel (Robinson et al., 2010) was used for exploring and identifying mare-filled craters. High–resolution images from the LROC-Narrow Angle Camera (NAC) with spatial resolution ~0.5–2 m/pixel (Robinson et al., 2010), Chandrayaan (CH2) Terrain Mapping Camera (TMC–2) with spatial resolution ~5 m/pixel (Chowdhury et al., 2020) and Selenological and Engineering Explorer (SE LENE)-Terrain Camera (TC) with spatial resolution ~10 m/pixel (Haruyama et al., 2008) were used for detailed observations and crater size-frequency distribution (CSFD) measurements. The topographic measurements of the mare-filled craters were carried out using the Lunar Orbiter Laser Altimeter (LOLA) with a spatial resolution of ~118 m/pixel and a vertical resolution of ~1 m (Smith et al., 2010b) and the merged LOLA and SELENE–TC digital elevation model (DEM) of spatial resolution of ~59 m/pixel with vertical resolution ~3–4 m (SLDEM2015) (Barker et al., 2016). The SLDEM2015 data was used up to 60°N/S due to limited coverage and LOLA data above 60°N/S latitude.

3.2.2 Identification and Classification of mare-filled craters

First, the dark mare plains were separated from the highlands using global mare boundaries (Nelson et al., 2014). Then craters, whose floors are filled with mare and have clear visible rims, were scouted using a global LROC-WAC mosaic (Robinson et al., 2010). Mare-infilled craters with enclosed/unbreached rims were only mapped, ensuring a more reliable investigation into subsurface magma infilling. We encountered several craters whose rims were breached, and lava entered the crater from the surroundings or vice-versa; such craters were excluded from this study. Additionally, the crater catalogue from Robbins (2019) was used in this study as a reference for mare-filled crater attributes (latitude, longitude, and diameter). In this survey, craters of diameters $\leqslant$ 1 km were excluded due to the low spatial resolution of LOLA (Smith et al., 2010b) and SLDEM2015 (Barker et al., 2016) data. A few anomalous rim breach mare-filled craters were included in this study because they are isolated from the surrounding mare. For example, craters centred at 55.7°S, 103.0°E and 55.2°S, 104.0°E rims breached into one another but are isolated from the surrounding mare. The identified mare-filled craters are investigated in detail and classified into five classes based on characteristics such as crater floor topography, mare-infilling depth within craters, terraced crater walls, central peak, and fractures. A summary of the characteristics of mare-filled craters for each class is provided in Table 3.1.

3.2.3 Measurements and Calculations

3.2.3.1 Morphometric analysis of mare-filled craters

For morphometric analysis of mare-filled craters, a contour map with 15 m intervals was constructed using SLDEM2015 (Barker et al., 2016)/ LOLA (Smith et al., 2010b). Then, for crater rim elevations (H_r), the highest elevation on the contours along the rim was traced, and elevations of the rim were extracted. While tracing the mare-filled craters' rims, the rims degraded by superposed craters were excluded. Spurious, high-elevated rims of the crater are also excluded. From the extracted crater rim elevations (H_r), an average rim elevation (H_{ar}) was calculated. Then, crater floor

Table 3.1: Characteristics of the mare-filled crater classes.

Class	Characteristics
1a	Mare-filled craters with nearly flat floors and absent central peaks and fractures.
1b	Mare-filled craters with nearly flat floors, with terraces, and wide crater walls lack central peaks and fractures.
2	Mare-filled craters with nearly flat floors, terraces, wide crater walls, and central peaks lack fractures.
3	Mare-filled craters with floor fractures. Few craters have a terrace, wide crater walls and central peaks, uplifted/subsided floors or both.
4	Mare-filled craters' floors vary from nearly flat to non-flat floors with uplifted/ subsided floors or both. Few have a central peak, extensive ejecta mantling on the floor, contain slump materials from walls, terraces and wide walls, and rims highly degraded.

Table 3.2: Equations used in the study

Description	Formula	Equation
Crater Depth (< 15 km)	$0.196 \times \text{Diameter}^{1.01}$	Eq. 3.1
Crater Depth ($\geqslant 15$ km)	$1.044 \times \text{Diameter}^{0.301}$	Eq. 3.2
Floor Diameter (< 20 km)	$0.031 \times \text{Diameter}^{1.765}$	Eq. 3.3
Floor Diameter (20-140 km)	$0.187 \times \text{Diameter}^{1.249}$	Eq. 3.4
Volume of Conical Frustum (km^3)	$\frac{\pi \times h \times (R_1^2 + R_2^2 + (R_1 \times R_2))}{3}$	Eq. 3.5
Central Peak Heights (km)	$0.032 \times \text{Diameter}^{0.900}$	Eq. 3.6
Central Peak Heights (km)	$0.005 \times \text{Diameter}^{1.297}$	Eq. 3.7
Central Peak Diameter (km)	$0.22 \times \text{Diameter}$	Eq. 3.8
Central Peak Diameter (km)	$0.138 \times \text{Diameter}^{1.053}$	Eq. 3.9
Volume of Cone (km^3)	$\frac{\pi \times r^2 \times h}{3}$	Eq. 3.10

elevations were derived by measuring the maximum and minimum elevations of the mare-filled crater floors (H_f) using contour lines. Some mare-filled craters classified in classes 3 and 4 were partially filled; in such instances, only the crater floor filled with mare was used to measure floor elevation. Also, some craters's floors in these two classes were uplifted and subsided; for example–the Pitatus (29.9°S, 14°W), the crater with the most complex floor morphology, only the northern floor for the calculations was considered in this study, assuming it was unaffected by modification (intrusion and subsidence). Then, an average floor elevation (H_{af}) was calculated using maximum and minimum floor elevations. From the calculated H_{ar}, H_{af} was subtracted to derive the average crater depth (H). For the exposed central peak height (H_{cp}) calculation, the maximum contour elevation (H_{max}) of the central peak was measured and subtracted from the H_{af}. These steps were followed to quantify all mare-filled crater morphologies. The mare-filled crater diameters were sourced from the Robbins (2019) crater catalogue, which was used to compute primary/expected crater depths (H_p) using Pike's empirical relationship (Pike, 1974) (Table 3.2 Eqs. 3.1 and 3.2). Finally, the mare thicknesses of mare-filled craters were obtained by subtracting the estimated average crater depth from the expected crater depths (Pike, 1974).

3.2.3.2 Volume estimation of mare-filled craters

For the estimation of the volume of mare-infilling, the available global mare boundaries map given by Nelson et al. (2014) was used to outline the area of mare units of mare-filled craters. In cases where there were no available mare boundaries, the mare unit area was measured. From the measured and obtained (Nelson et al., 2014) mare unit areas of classes 1a and 1b, the average radius was calculated assuming the area of mare units to be a circle; then, the radius of the expected crater floors is calculated using Pike (1977) empirical formula (Table 3.2 Eqs. 3.3 and 3.4). From the calculated parameters (mare thickness, radius of mare units, and radius of crater floor), the approximate volume of mare-infillings was calculated using the formula of the conical frustum (Table 3.2 Eq. 3.5). Craters approximately $\geqslant$15 km have a central peak; thus, using the empirical formulas of expected peak height (Table 3.2 Eq. 3.6 and 3.7) and expected peak diameter (Table 3.2 Eq. 3.8 and 3.9) given by Pike (1977); Krüger et al. (2018), the volume of peaks was estimated by considering it as a cone (Table 3.2 Eq. 3.10).

Then the volume of peaks was subtracted from the volume of mare-infilled for a more accurate estimate of the volume of infilling. The volume was calculated only for classes 1a and 1b, as class 2 has partially exposed central peaks, and classes 3 & 4 have complex modifications like upliftment and subsidence. Additionally, the infilling in classes 3 and 4 does not fully cover the crater floor, complicating calculations. Therefore, this study focused on class 1a and 1b scenarios, using the geometry of a conical frustum to determine the volume of infilling in these craters.

3.2.4 Crater Size-Frequency Distributions

The model ages of mare units of mare-filled craters were derived using crater size-frequency distribution (CSFD) and fitting them into the production and chronology functions of Neukum et al. (2001). In ArcGIS 10.4, high-resolution images were imported, then mare units for counting craters were demarcated using existing global mare boundaries (Nelson et al., 2014) followed by crater counting and measurements using CraterTools (Kneissl et al., 2011). While counting the craters, secondary craters and pits were avoided, which contributed to errors. The exported CSFD in .scc format was then imported and fitted using CraterStats-II (Michael and Neukum, 2010) for obtaining ages. In this study, mare-filled craters of smaller diameters, $<$10 km, were not dated because there were fewer impact craters to count, which contributed to a large statistical error in the CSFD analysis.

3.3 Results

3.3.1 Mare-filled crater classes

The five characteristics of mare-filled craters with examples are described below, including their elevation profile and a plot of the frequency distribution.

Class 1a mare-filled craters have nearly flat floors, lava infilling within the crater inundates the walls, and they lack central peaks and fractures. Some craters host small wrinkle ridges on the floor. In this class, 33 mare-filled craters were identified, with diameters ranging from $\sim$8 km to $\sim$103 km. An example of this class is the Billy crater (13.8°S, 50.2°W) (Figures 3.1a and b), and a frequency size distribution plot is shown in Figure 3.1c.

Class 1b mare-filled craters have nearly flat floors with wide and terraced crater walls but miss central peaks and fractures. A distinguishable difference between class 1b and class la is the presence of wider and terraced crater walls with relatively less infilling in class 1b. In this class, 39 mare-filled craters were identified with diameters ranging from ~7 km to ~93 km. An example of class 1b mare-filled craters is the Lomonosov (27.3°N, 98.3°E) (Figures 3.2a and b). A frequency size distribution plot for this class is in Figure 3.2c.

Class 2 mare-filled craters have nearly flat floors, wide and terraced crater walls, distinguishable central peaks, and lack fractures. The most notable feature in this class is the central peak. All the craters in this class contain a central peak, whereas class 1 craters do not have a peak. A total of 24 class 2 mare-filled craters were identified, and the diameter ranged from ~18 km to ~234 km. An example of class 2 mare-filled crater is the Maksutov crater (40.8°S, 168.6°W) (Figures 3.3a and b), and the frequency size distribution plot is in Figure 3.3c.

Class 3 mare-filled craters are similar to craters mapped by Jozwiak et al. (2012) with fractured floors; few of these craters have terraces and wide walls, and ~35% of craters contain central peaks. Some crater floors of this class have mare deposits only adjacent to the fractures, and variation in the mare-infilling area is observed. Fractured floors are the most distinctive feature of this class. A total of 46 Class 3 mare-filled craters were identified, and their diameter ranges between ~15 km and ~204 km. An example for this class is the Lavoisier E crater (40.9°N, 80.4°W) (Figures 3.4a and b). It has a fractured floor and contains a central peak of ~610 m (Figure 3.4b). A frequency size distribution plot for class 3 is shown in Figure 3.4c.

Class 4 mare-filled craters consist of diverse morphological features within the floor, ranging from flat to non-flat, extensively mantled by ejecta and collapse/uplift. Few of them contain slump materials, terraced walls, and highly degraded craters' rims from subsequent impact cratering. Nearly 11% of the craters in this class have central peaks. A total of 182 class 4 mare-filled craters were identified, and their diameter ranges from ~4 km to ~270 km. An example of a class 4 mare-filled crater is shown in Figure 3.5. The Nishina crater (44.6°S, 170.8°W) has a flat floor profile, extensively ejecta-mantled floor, and degraded crater rim (Figures 3.5a&b).

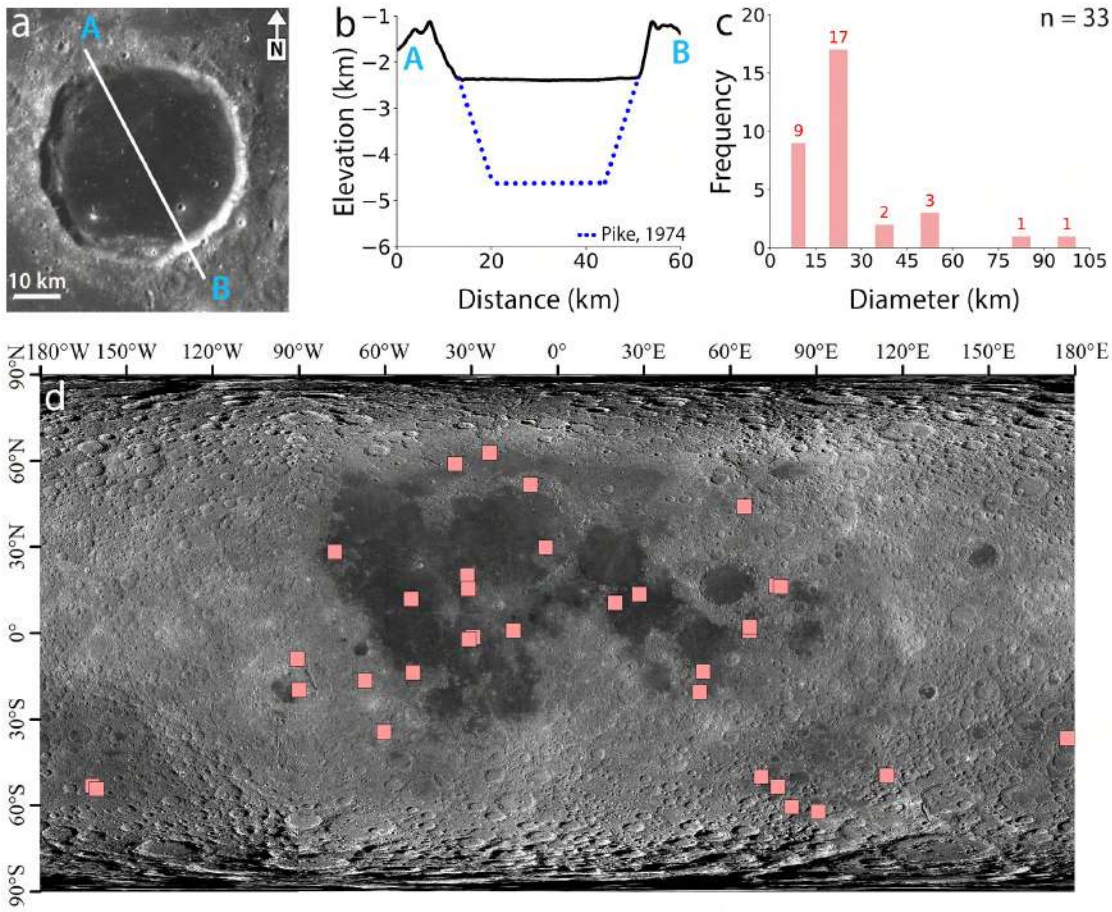

Figure 3.1: Class 1a mare-filled craters: a-b) the Billy crater (13.8°S, 50.2°W), and its topographic profile (solid black) and the expected crater depth (dotted blue), c) size frequency distribution, and d) global distribution of class 1a mare-filled craters.

The Neper crater (8.8°N, 84.6°E) is an example of a non-flat floor crater. It has an uplifted convex-up crater floor profile (Figures 3.5c and d). Another example of the non-flat floor crater centred at 43.4°S, 162°E is shown in Figure 3.5e. It has a collapsed/subsided crater floor profile (Figure 3.5f). A frequency size distribution plot for class 4 is shown in Figure 3.5g.

3.3.2 Mare-filled crater distributions

The global distribution of mare-filled craters shows that ~60% of the mare-filled craters are located on the nearside and ~40% on the farside (Figure 3.6a). They are predominantly located at the periphery of the lunar mare and mare-filled impact basins, some within the mare/mare-filled impact basins and a few in the highlands. Clusters of mare-filled craters are observed in the north-western region of the Oceanus Procellarum, Mare Australe, the superpose regions of Mare Crisium and Mare Smythii, and

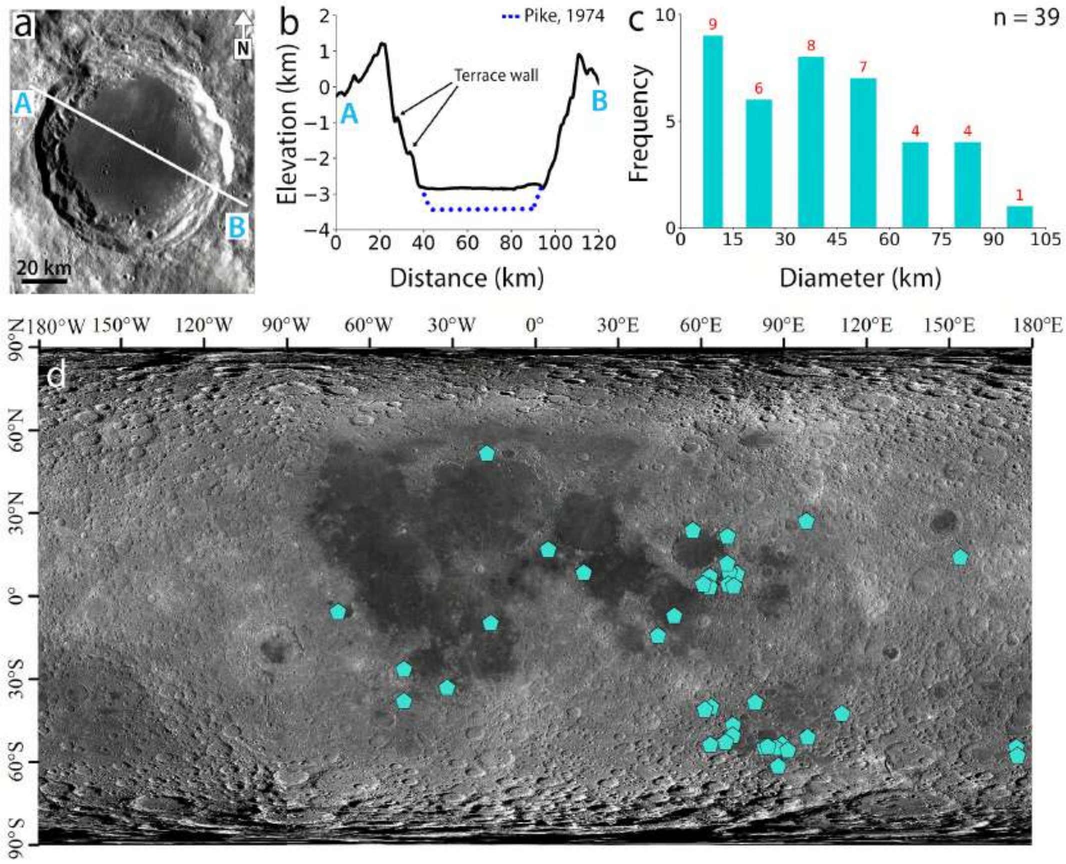

Figure 3.2: Class 1b mare-filled craters: a-b) the Lomonosov crater (27.3°N, 98.3°E), and topographic profile in solid black and the expected crater depth (dotted blue), c) size frequency distribution, and d) global distribution of class 1b mare-filled craters.

between Mare Nectaris and Mare Fecunditatis. The superpose regions of Mare Nectaris and Mare Fecunditatis host all five types of mare-filled craters classes. Among the clusters, Mare Australe contains the maximum mare-filled craters and lacks class 3 mare-filled craters. A total of 324 mare-filled craters were identified, and among them, smaller diameter craters are relatively higher in frequency than larger diameter craters (Figure 3.6b). The smallest mare-filled crater diameter observed is ~4 km (class 4), and the largest is ~270 km (class 4). This study found that out of the 324 identified mare-filled craters, ~20% are simple craters. The identified simple craters are widely distributed within the nearside mare regions. The size-frequency distribution of mare-filled craters shows that both simple and complex craters have been modified by mare-infilling.

Global distributions of individual classes of mare-filled craters are shown in Figures: 3.1d, 3.2d, 3.3d, 3.4d, and 3.5h. Class 1a type mare-filled craters

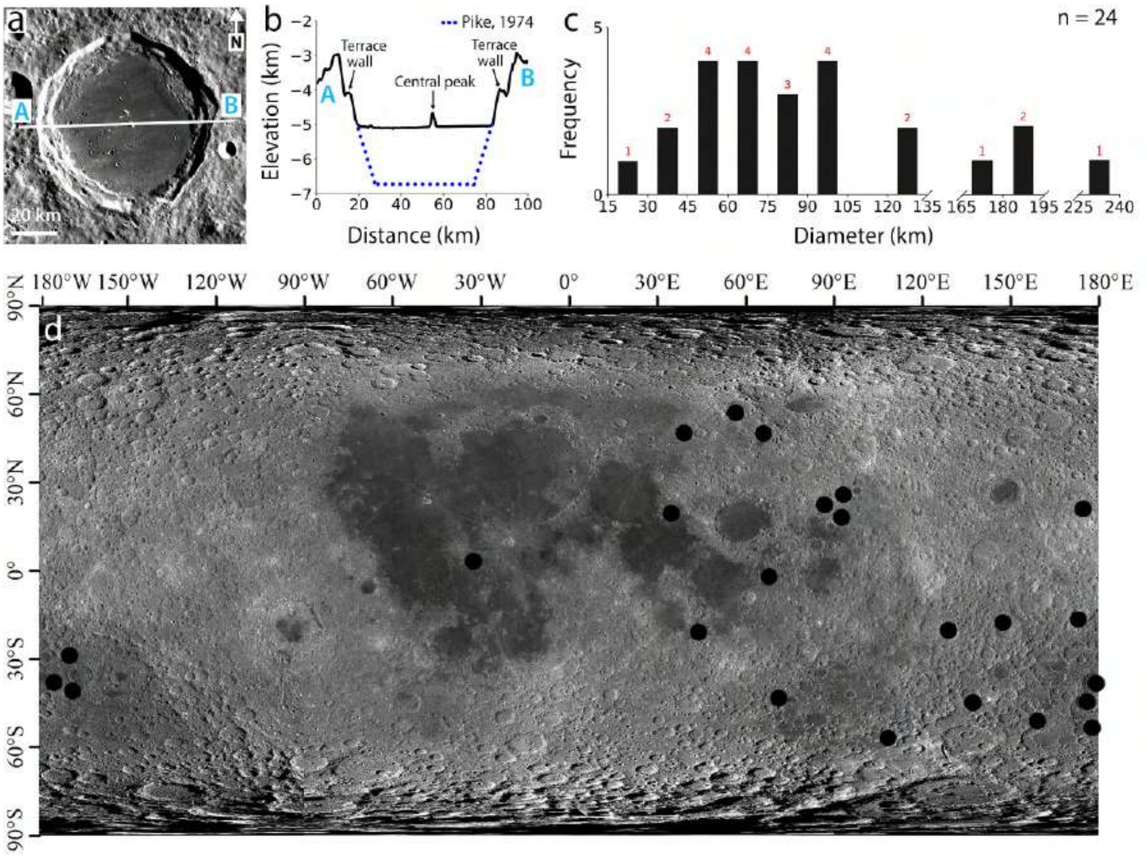

Figure 3.3: Class 2 mare-filled craters: a-b) the Maksutov crater (40.8°S, 168.6°W), and its topographic profile (solid black) and the expected crater depth (dotted blue), c) the size-frequency distribution, and d) the global distribution of class 1b mare-filled craters.

are predominantly located within the lunar mare/mare-filled impact basins rather than the periphery of mare/mare-filled impact and the highland regions (Figure 3.1d). Contrary to class 1a, class 1b mare-filled craters are mostly found at the periphery of these regions (Figure 3.2d). Class 2 mare-filled craters are mostly distributed in the highland regions and the periphery of mare/mare-filled impacts, and a very few within the lunar mare/mare-filled impact basins (Figure 3.3d). Class 1b and class 2 mare-filled craters are distributed mainly in the eastern regions of the Moon. Class 3 mare-filled craters have a similar distribution as class 1b, mostly located at the periphery of mare/mare-filled impact than the other locations (Figure 3.4d). Class 4 mare-filled craters are extensively distributed across the periphery of mare/mare-filled impact basins and within the lunar mare/mare-filled impact basins and highland regions (Figure 3.5h).

Overall, the distribution of mare-filled craters shows that nearly 50% of craters are present at the periphery of the lunar mare/mare-filled basins

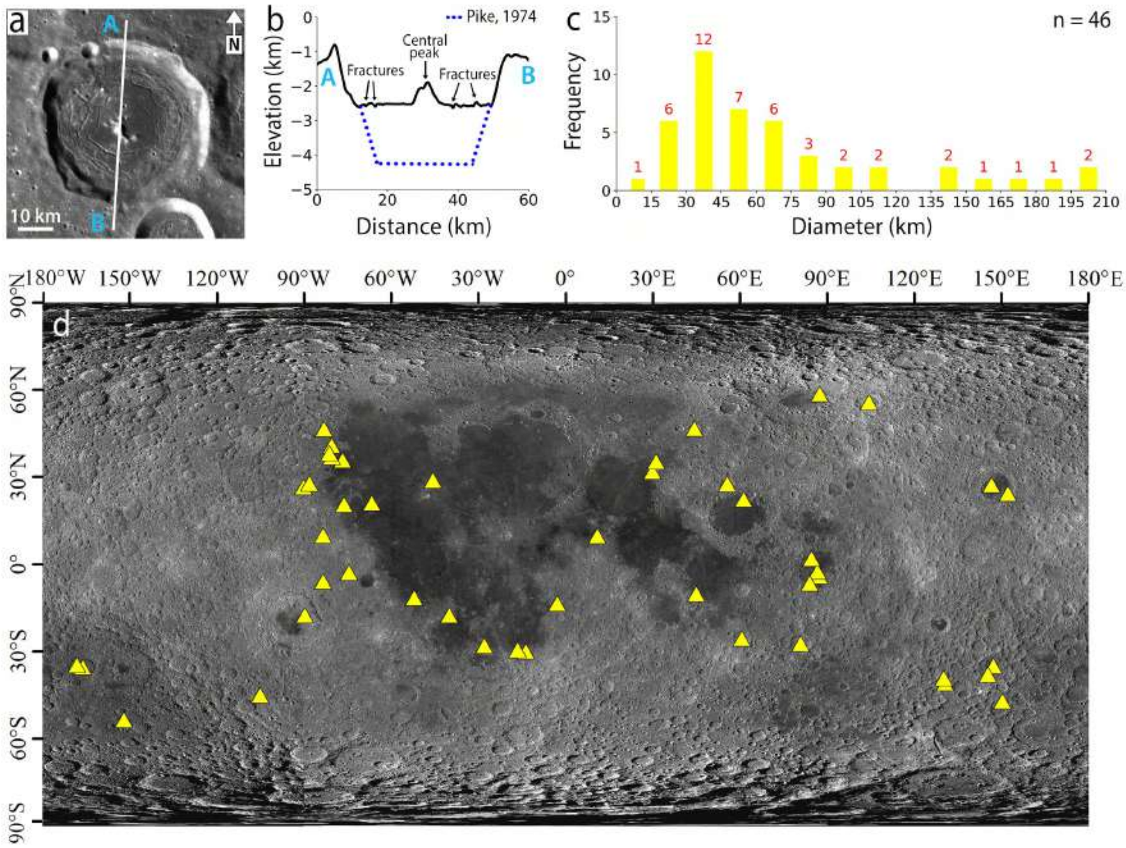

Figure 3.4: Class 3 mare-filled craters: a) the Lavoisier E crater (40.9°N, 80.4°W); b) the topographic profile of the Lavoisier E crater (solid black) and the expected crater depth (dotted blue); c) the size-frequency distribution; and d) the global distribution of class 3 mare-filled craters.

and ∼20% within the mare/basins. The majority of the mare-filled craters are classified in class 4, and this class has the highest number of craters distributed within and at the periphery of the mare/mare-filled basins.

3.3.3 Depths of mare-filled craters

The depth-to-diameter plots of the different mare-filled crater classes and expected crater depths calculated using Pike (1974) empirical relationship for each mare-filled crater are shown in Figure 3.7. The mare-filled craters are shallower than fresh/ normal craters, and this study reveals that ∼79% of the craters in class 1a have depths <1 km, followed by classes: 4 (∼54%), 3 (∼30%), 1b (∼13%), and 2 (∼4%). A total of 145 mare-filled craters have depths <1 km. The maximum crater depth observed within the identified mare-filled crater is ∼4 km (Diameter(D) ∼133 km, class 2), the minimum is ∼97 m (D ∼7 km, class 4), and an average of ∼1 km.

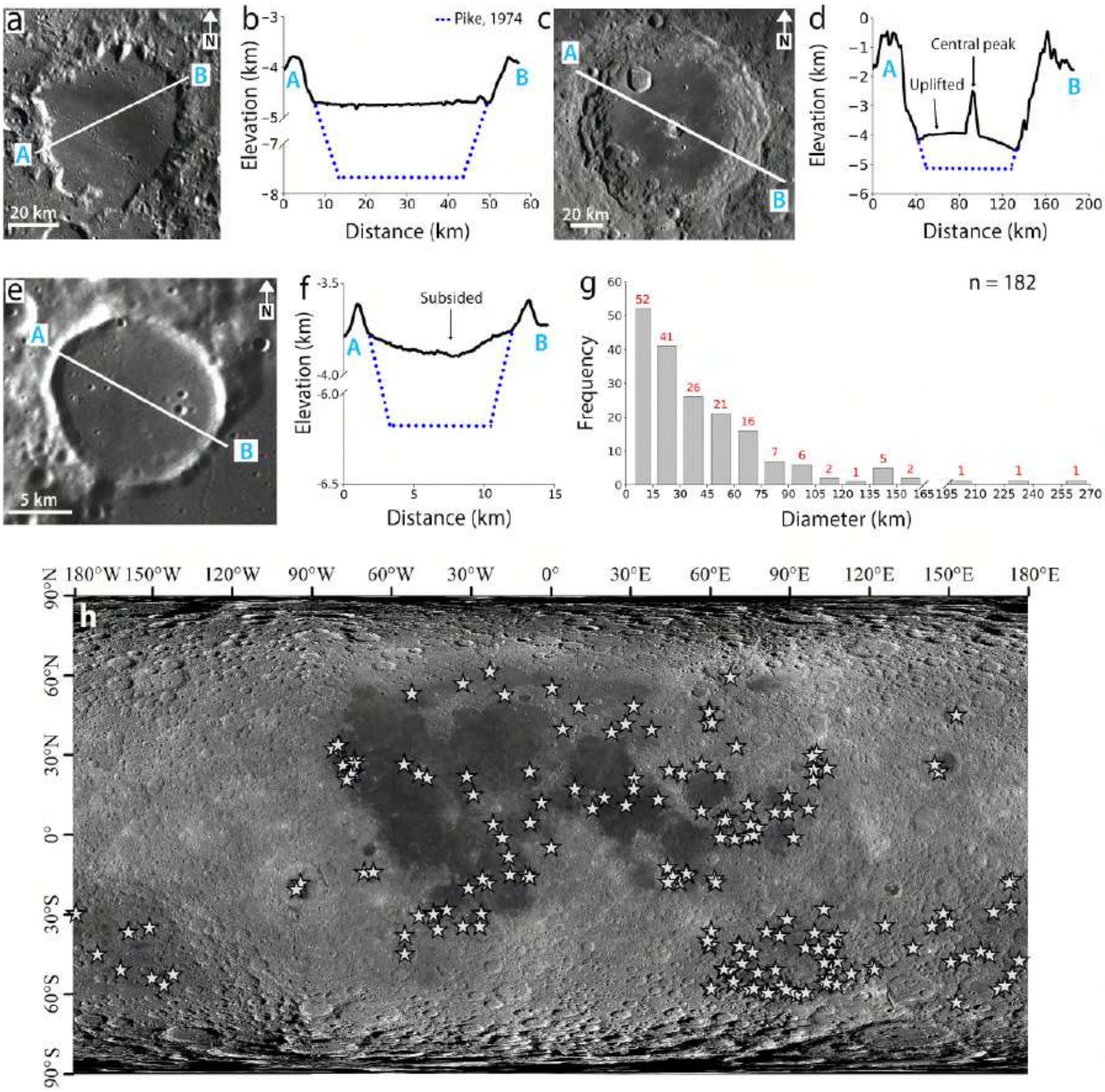

Figure 3.5: Class 4 mare-filled craters: a) the Nishina crater (44.6°S, 170.8°W), b) topographic profiles (solid black) and expected crater depths (dotted blue), c) the Neper crater (8.8°N, 84.6°E), d) topographic profiles (solid black) and expected crater depths (dotted blue), and e) the crater centred at 43.4°S, 162.0°E, f) topographic profiles (solid black) and expected crater depths (dotted blue), g) size frequency distribution, and h) global distribution of class 4 mare-filled craters.

These new mare-filled craters study confirm that they typically differ from fresh/ normal craters in their depth-to-diameter ratio, and infilling varies among the craters and the regions. Similar shallower depths were observed in previous FFCs studies (Schultz, 1976; Jozwiak et al., 2012).

3.3.4 Central peak heights of mare-filled craters

Among the identified 324 mare-filled craters, ∼253 mare-filled craters have crater diameters >15 km; therefore, these craters are within the size range where they could feature central peaks, but only ∼24% feature them. Central peaks are observed in all 24 class 2 craters, 17 class 3 craters, and 20 in class 4 mare-filled craters. The maximum peak height is ∼3270 m (class 2), and the minimum height is ∼25.5 m (class 2). The mare-filled crater diameter to central peak heights plot up to 150 km diameter is shown in Figure 3.8, along with the expected central peak heights calculated using empirical relationships given by Pike (1977); Krüger et al. (2018) (Table 3.2 Eqs. 3.6 and 3.7). Peak heights are smaller than expected, and in two cases, they are higher than the estimates, which belong to classes 3 and 4.

3.3.5 Model ages of mare-filled craters

Total 23 mare units were dated from class 1a, 28 from class 1b, 12 from class 2, and 3 from class 3. A total of 66 mare units were dated, and 65 were obtained from previous studies Hiesinger et al. (2003, 2011); Morota et al. (2011); Whitten et al. (2011); Pasckert et al. (2015); Greenhagen et al. (2016); Shirley et al. (2016); Pasckert et al. (2018); Thesniya et al. (2020) where 7 mare units ages belong to class 1a, 5 to class 1b, 12 to class 2, 9 to class 3, and 32 to class 4. In this study, mare units of class 4 were not dated. Only three craters from class 3 were dated because mare-filled craters in these two classes (3&4) are extensively modified by upliftment, subsidence, fracturing of crater floors, ejecta mantling and slump materials from walls. The spatial distribution of model ages obtained in this study and obtained ages from the previous study is shown in Figure 3.9a.

Using CSFD, the obtained ages of mare units of mare-filled craters range from ∼4 Ga to ∼1.7 Ga (Figure 3.9a, Table AI-1). The maximum and minimum area dated are ∼3482 sq. km (class 1a) and ∼34 sq. km (class 1a), respectively. The ages obtained in this study (66) and from previous studies (65) of mare units are sorted in 0.5 Ga bins and plotted, showing an asymmetrical distribution in mare-infilling ages (Figure 3.9b). There is more than one mare unit in a few of the mare-filled craters. In such a scenario, previous studies reported more than one mare unit age for a

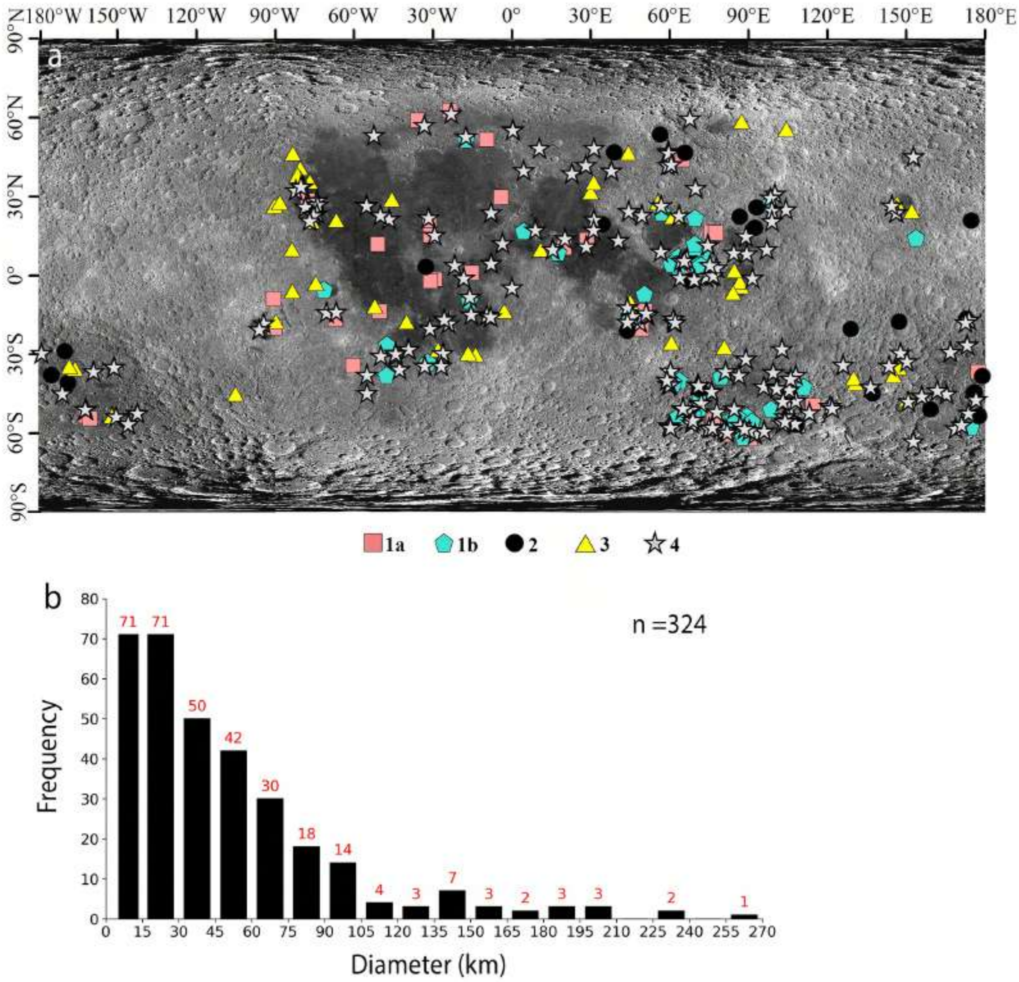

Figure 3.6: a) The global distribution of five different classes of mare-filled craters identified in this study; and b) size-frequency distribution.

mare-filled crater; in this study, the youngest ages reported were considered because we are interested in late-stage infilling ages. In this study, 47 mare units show kink/step in the crater size-frequency distribution in the cumulative crater frequency (N_{cum}) plot, indicating the resurfacing of the mare units by lava eruption (Neukum and Horn, 1976) or due to the formation of new craters that destroyed the old craters at the same rate (Hirabayashi et al., 2017). Also, the frequency plot (Figure 3.10) of lava infilled volume $\geqslant$1100 km^3 for classes 1a and 1b mare-filled craters suggests multiple episodes of lava filling/ resurfacing as it is greater than the estimated dike volume of a single episode of lava filling, which ranges from 102 km^3 to 103 km^3 in the nearside (Head and Wilson, 2017; Wilson and Head, 2018). Examples of mare-filled craters with multiple episodes of resurfacing on the nearside and the regions of the basin with similar crustal thickness to the nearside are Plato, Archimedes, Cruger, Billy, Petrov, Brisbane E, Abbe, Jeans U, Harlan, Lyot L, Hess, and Jeans. This study observed that 27 mare-filled craters have a volume $\leqslant$102 km^3 which is less than the expected ranges (102 km^3 to 103 km^3), suggesting a single episode of resurfacing. Therefore, from the frequency plot, this study expects that single episodes of resurfacing were more frequent in mare-filled craters than multiple episodes.

3.4 Discussion

3.4.1 Mare-filled and Fresh craters

Mare-filled craters are compared with similar diameter fresh/unmodified craters and among themselves. This comparison is aimed at investigating the variation in mare-filled crater morphology, the complex processes occurring in mare-filled craters, and how they vary with respect to location and crater sizes. In this study, impact craters that are not affected by endogenic, post-modification processes are called fresh/ unmodified craters. Mare-filled craters are morphologically modified craters through magmatism and contain lava infilling on their floors. For example, the Herodotus crater floor covered with mare material lacks a central peak. In contrast, the Aristarchus unmodified crater has a terraced wall, central peak, slump materials, and impact melt on the crater floor. Their difference in crater depths is observed in profiles; Herodotus has a shallower crater depth of ~2 km than the Aristarchus crater (Figure 3.11). Infilled magma material within the Herodotus crater may have buried its central peak.

Another example, the Kopff crater (class 3) with floor fracture, is compared with the nearby fresh Maunder crater (Figure 3.12). The Maunder crater has a terraced crater wall, a central peak, slump materials, and impact melt on the crater floor, while the Kopff crater has a fractured floor, no central peak, no wall terraces and is ~2 km shallower than the Maunder crater (Whitten et al., 2011). Similarly, due to the lava infilling the simple crater of similar diameter, the Harpalus G (53.6°N, 52.3°W, class 4) is ~0.7 km shallower than the Harpalus H (53.8°N, 53.3°W, unmodified) crater. The craters measured in this study are relatively shallower than the fresh ones due to the mare-filling/ intrusion.

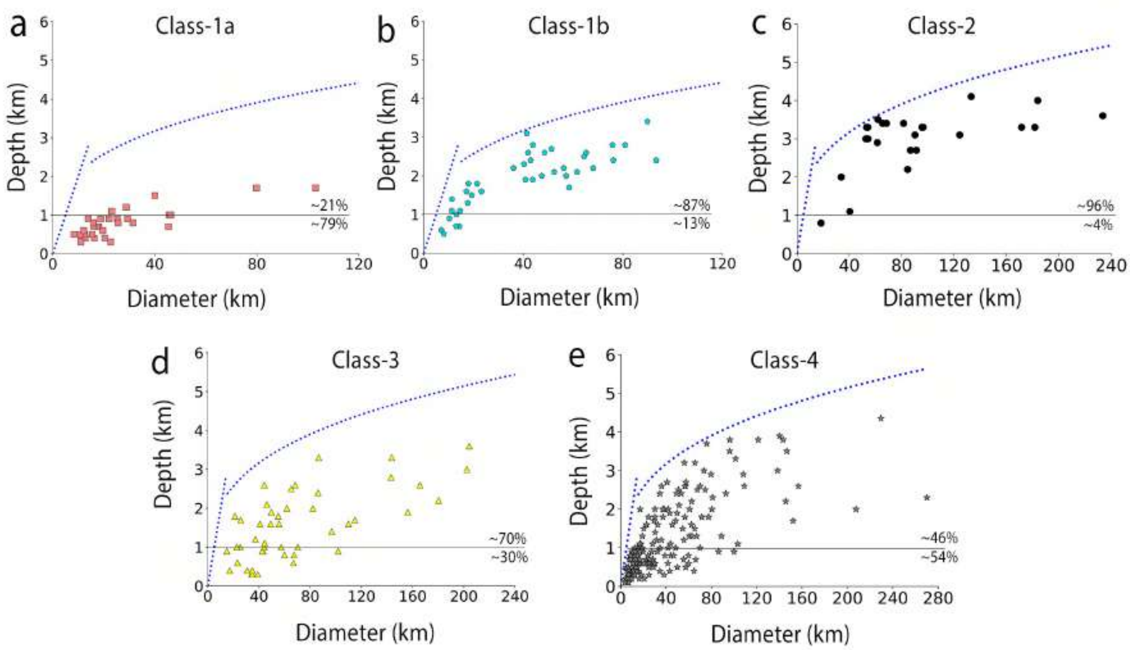

Figure 3.7: Measured crater depth to diameter and the expected crater depths (dotted blue) of five mare-filled crater classes: a) class 1a, b) class 1b, c) class 2, d) class 3, and e) class 4.

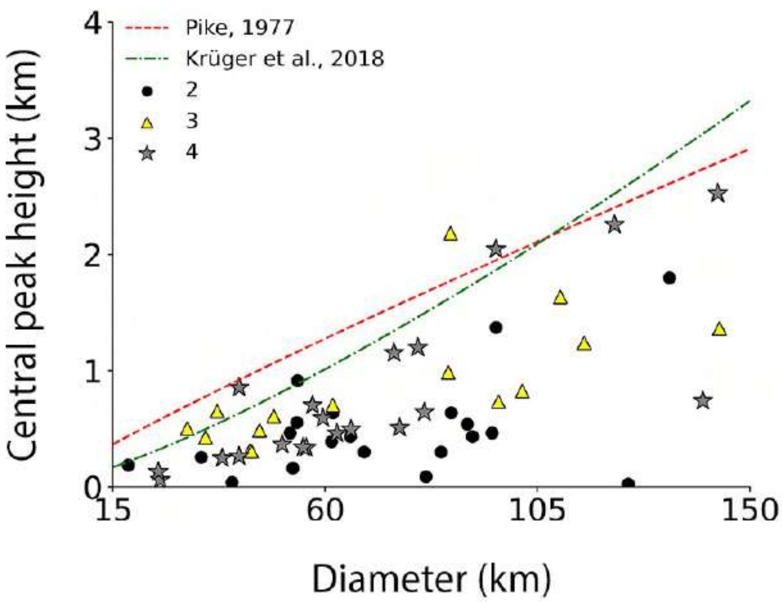

Figure 3.8: Central peak height to crater diameter of classes 2, 3, and 4 and the expected peak height by Pike (1977) (dash red) and Krüger et al. (2018) (dash green).

3.4.2 Class 1a and 2

The main difference between class 1a and 2 mare-filled craters is that class 2 mare-filled craters have a central peak and terraced wall along with mare-infilling. For example, class 1a (Lansberg C) and class 2 (Kunowsky) have similar diameters. They have a nearly flat floor; however, the Kunowsky ($\sim$ 1.8 Ga) has an exposed central peak and terrace wall, and the Lansberg C ($\sim$2.0 Ga) has a shallower crater depth and no central peak (Figure 3.13). The classes 1a and 2, as shown in Figure 3.7 a and c, indicate that $\sim$79% of mare-filled craters in class 1a have crater depths $<$1 km, and $\sim$96% mare-filled craters in class 2 have crater depths $>$1 km, suggesting mare-filled craters categorised in class 1a have relatively shallower depths/ higher infilling than class 2, and that central peaks are entirely buried in class 1a (Schultz, 1976). However, the class 2 mare-filled crater's central peaks are exposed, and few crater walls appear wider than class 1a because of relatively less lava infilling. Besides lava infilling in both classes, a few mare-filled craters contain wrinkle ridges. Other features, like fractures, were not observed in either class. Therefore, the magmatism processes are possibly the same in both classes; only the level of lava infilling varies where class 1a mare-filled craters have relatively higher infilling than the mare-filled craters in class 2.

3.4.3 Class 1a and 3

Mare-filled craters in class 3 have more complex crater floor morphologies than classes 1a, 1b, and 2 craters. Class 3 mare-filled craters are floor-fractured craters (FFCs) formed due to shallow magma intrusion (Jozwiak et al., 2012, 2015). Magma starts intruding when it reaches neutral buoyancy (Head and Wilson, 2017; Wilson and Head, 2017). FFCs are characterised by radial, concentric, and polygonal floor fractures, and these fractures are observed within the crater floor and have shallow crater depth (Schultz, 1976; Jozwiak et al., 2012). However, along with fractures, few FFCs have mare deposits on the floors of the craters (Schultz, 1976; Jozwiak et al., 2012). In this study, FFCs with mare-infilling were only considered. A comparative example of class 1a and 3 mare-filled craters—the Billy and the Hansteen—of similar diameter nearby is shown in Figure 3.14. Example of class 1a: the Billy crater floor appears smooth, nearly flat, and lacks fractures. However, class 3, Hansteen mare-filled crater, has a partially

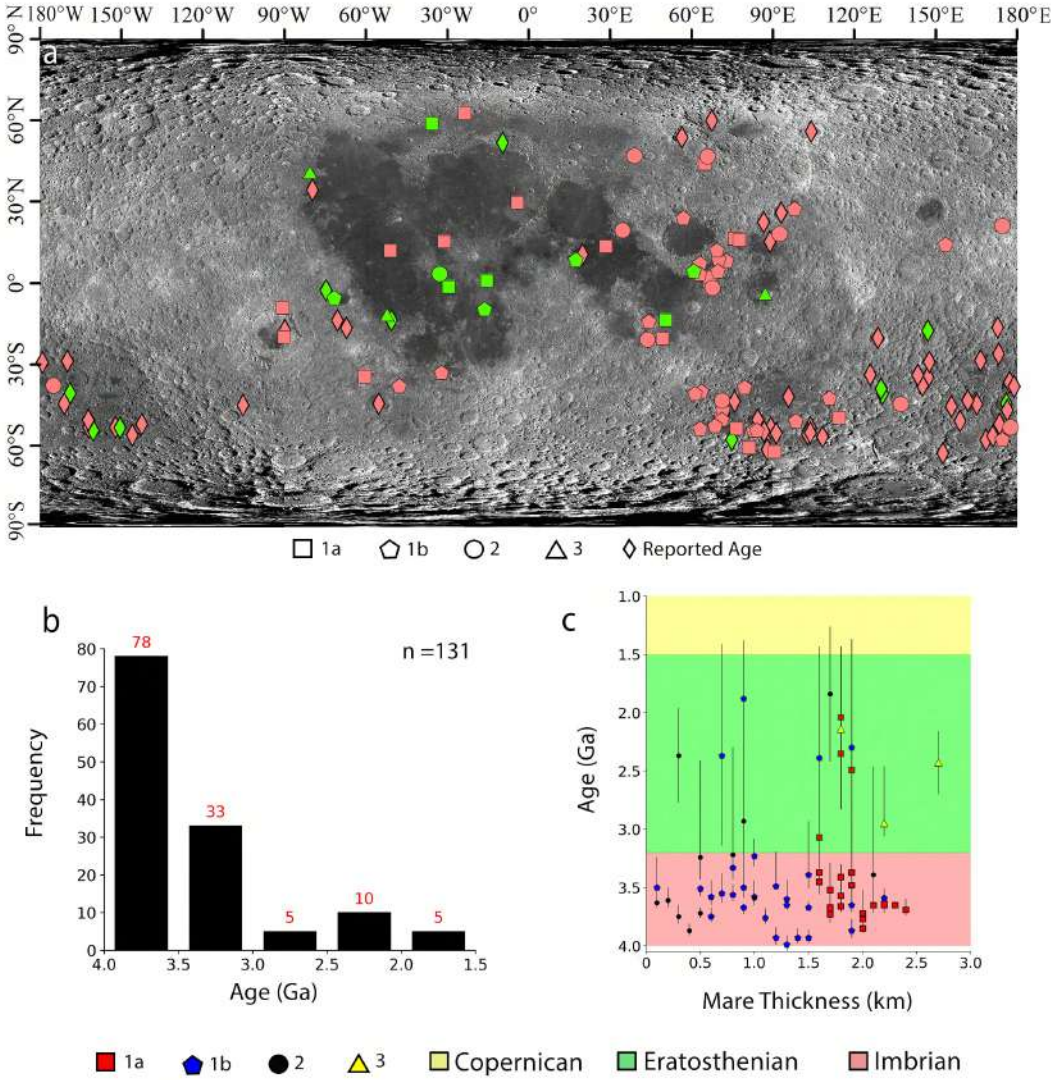

Figure 3.9: a) Locations of CSFD analysis in this study along with previously reported ages; b) Age frequency distribution; c) Measured model ages vs. mare thickness of 66 mare-filled craters.

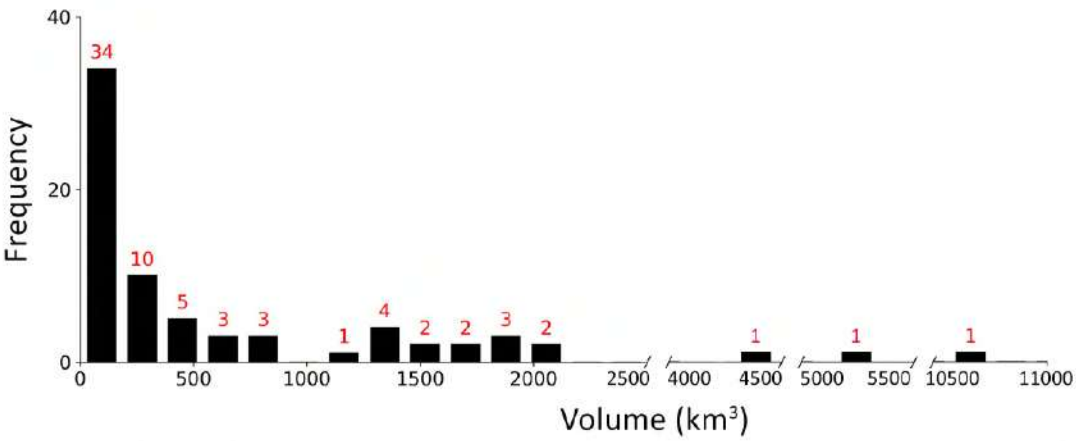

Figure 3.10: Frequency plot of lava volume for classes 1a and 1b mare-filled craters.

infilled and fractured floor. The mare-infilling floor is ~450 m deeper than the fractured floor, suggesting modification of FFCs by mare-infilling starts from a lower elevated area. Mare-infilling floor inundated areas in classes 1a, 1b, 2, and 4 increase with increasing diameters; however, class 3 does not show such an increasing relationship (Figure AI-2), possibly due to the presence of fractures. The fracturing of the crater floor creates undulating surfaces, which possibly restrict the spread of mare on the floor, resulting in the confined region of the crater floors. The presence of fractures and mare-infilling in class 3 mare-filled crater floor suggests class 3 craters are not only affected by the intrusion but also by the extrusion process, indicating a more complex scenario than class 1a. These craters (class 3) are typical examples of multiple magmatism processes that occurred within the same crater, which are described in detail in the following section.

3.4.4 Mare Modified-Floor Fractured Craters (MM-FFC)

Jozwiak et al. (2012) reported 170 FFCs, and out of those, this study identified and analysed 35 FFCs with mare-infilling. These 35 FFCs belong to classes 1, 2, 3, 4a, 5, and 6 of the Jozwiak et al., 2012 classifications (Table AI-1). Jozwiak et al. (2012) reported mare materials within classes 1 and 6, but we have noticed mare deposits in almost all the classes. In this study, the mare-infilled FFCs studied by Jozwiak et al. (2012) were re-examined and inferred the following: two FFCs of class 2, eighteen in class 3, two in class 4a, and one in class 5 Jozwiak et al. (2012) classified FFCs are mare-infilled FFCs. Apart from these 35 FFCs, in this study, 11 additional FFCs with mare-infilling were newly reported.

Schultz (1976) study suggested that mare-infilling and inundation of fractures in FFCs is the last stage of modification, but all FFCs did not evolve to the last stage, and infilling can occur at any stage (Schultz (1976): Figure 10). The observations of the cross-cutting relationship of infilling and fractures in some craters by this study (Figures 3.15a-c) suggest fracturing occurred first, followed by mare-infilling in the last stage, the same as Schultz (1976) study. Class 3 craters with <100% mare floor area coverage in the plot of the mare floor area coverage vs. depth plot (Figure AI-3) also suggest that all FFCs did not evolve to the last stage. Acknowledging the suggested concept of Schultz (1976) and from this study, examples of mare-modified FFCs with different mare-covered surface areas in percentage

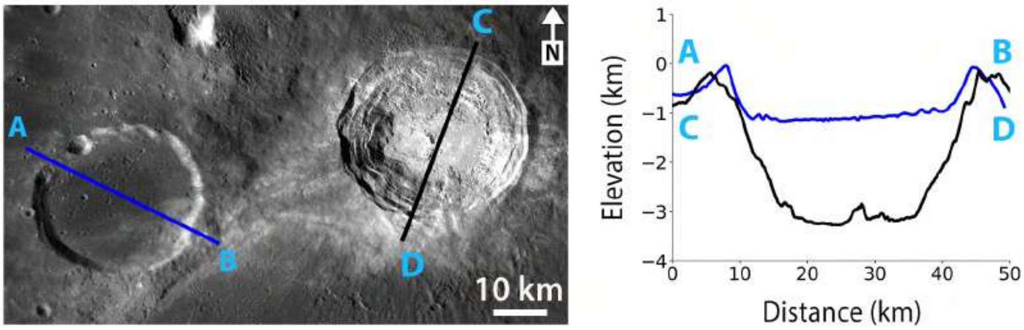

Figure 3.11: An example of a mare-filled crater and an unmodified crater. A significant crater depth difference is observed in the Herodotus (23.2°N, 49.8°W, solid blue) mare-filled crater (class 4), and the fresh Aristarchus crater (23.7°N, 47.5°W, solid black).

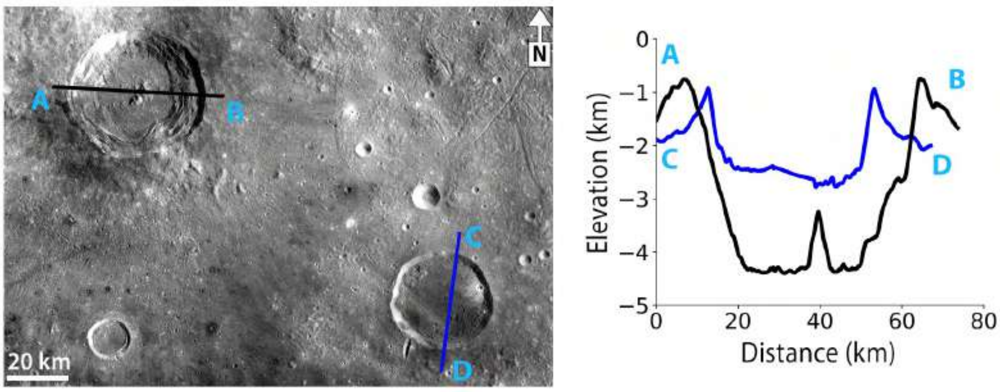

Figure 3.12: An example of a mare-filled crater and an unmodified crater. A significant crater depth difference was observed in the Kopff (17.4°S, 89.7°W, solid blue) mare-filled crater (class 3) and the fresh Maunder crater (14.5°S, 93.9°W, solid black).

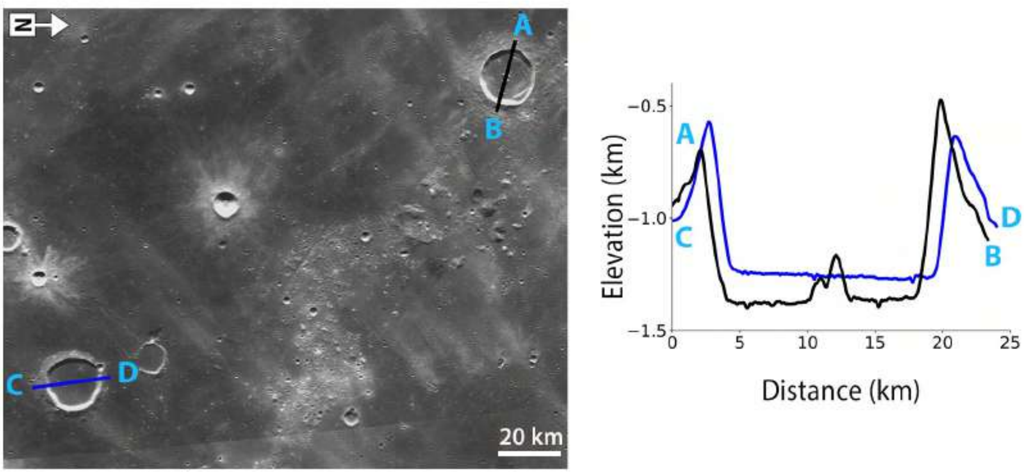

Figure 3.13: An example of mare-filled craters with and without a central peak: the Lansberg C (1.5°S, 29.2°W, class 1a, solid blue) and the Kunowsky (3.2°N, 32.5°W, class 2, solid black).

are shown in Figure 3.15. We calculated the area percentage of Mare Modified–FFC (MM–FFC) by dividing the mapped mare-covered area by the crater floor area. On arranging these four craters in increasing order of surface area covered by mare-infilling, the Fenyi crater is trailed by the Schubert C crater, the inner Gerard Q crater, and then the Warmer crater. Irrespective of their size, these examples were considered to show how mare surface areas gradually increased and fractures covered areas decreased. From this observation, this study expects that some of the mare-filled craters (class 1a) may be earlier FFC craters that completely resurfaced over time (example Figure 3.14).

The zone of shallow depth/highly infilled and ⩾50% mare floor area (light blue coloured region, Figure AI-3) suggest that mare-modified FFCs in this zone are extensively altered by mare-infilling. These craters are potential examples where mare-infilling obliterated the floor fractures and fully resurfaced, and they could have formed mare-filled craters such as 1a, 1b, 2, and 4. However, it is also possible that mare deposits in mare-filled craters result directly from extrusion without prior floor fracturing caused by the intrusion process. The interesting observation made here suggests that the class 3 craters in this study are typical examples of episodic or multiple floor deformation magmatism (extrusion and intrusion) processes. The mare resurfacing within the FFC may have continued after the fracture formation, or it can happen after a time gap. Therefore, it indicates that these craters are potential targets to explore for multiple magmatism processes.

Schultz (1976) study also suggests that inundated floors of mare-modified FFCs can again be fractured due to subsidence caused by magma draining out from the magma reservoir (Schultz (1976): Figure 15). An example observed in this study is the Pitatus (29.9°S, 14°W) crater. This study also observed mare-filled craters associated with regional fractures such as the Gerard Q (46.6°E, 83.1°W) (Figure 3.15c). Therefore, this study expects crater floors can be fractured by intrusion/doming (Jozwiak et al., 2012, 2015), collapsed/subsidence of mare-filled crater floors (Schultz, 1976; Geshi et al., 2014; Anderson et al., 2019) and reactivation of existing regional fractures.

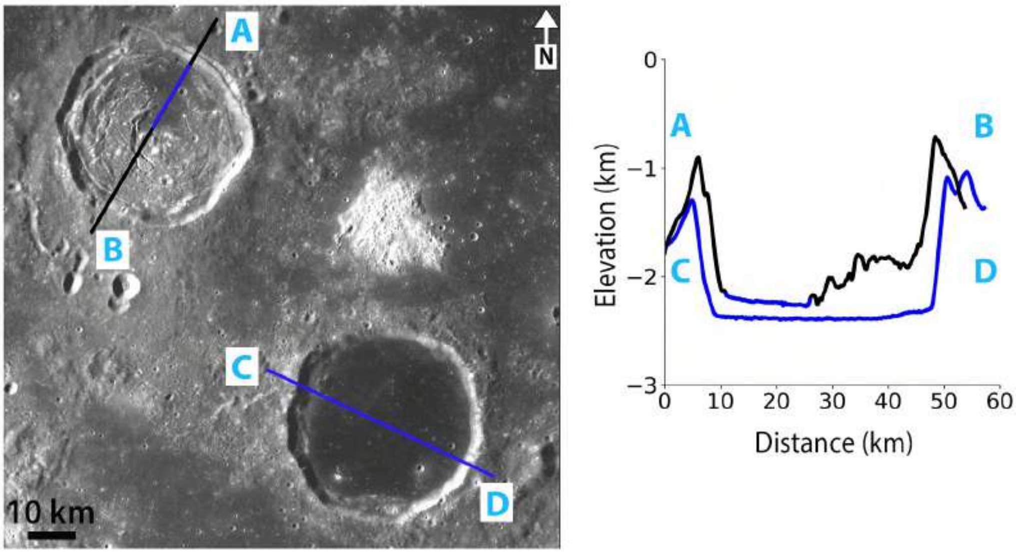

Figure 3.14: An example of mare-filled craters with a mare-inundated floor and a fractured partially filled floor is the Billy crater (13.8°S, 50.2°W, class 1a, solid blue) and the Hansteen crater (11.5°S, 52.0°W, class 3, solid black with a solid blue segment in the mare portion).

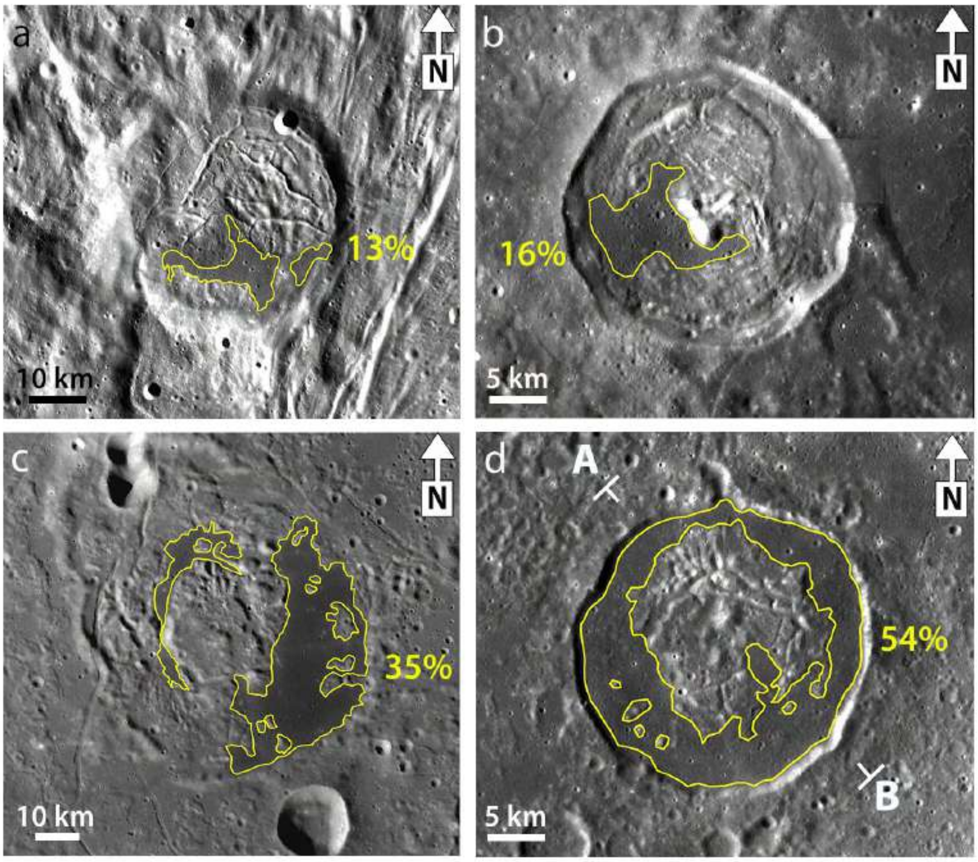

Figure 3.15: Examples of modification of FFCs by mare-infilling in different percentages. a) 13% of the Fenyi (45°S, 105°W), b) 16% of the Schubert C (1.9°N, 84.6°E), c) 35% of the Gerard Q (46.6°N, 83.1°W), and d) 54% of the Warmer (4.0°S, 87.4°E) floor area is modified by the mare.

3.4.5 Class 1a and 4

Class 4 mare-filled crater floors vary from nearly flat to concave down/uplifted and concave up/subsided, and some are mantled by thick ejecta layers. Class 4 mare-filled craters with a nearly flat floor are very similar to class 1a mare-filled craters, but due to thick ejecta mantling, they were classified in class 4, for example, the Nishina crater (Figure 3.5a). Some class 4 mare-filled crater floors are uplifted and subsided similar to class 3 mare-filled crater floors; for instance, the Neper and the crater centred at 43.4°S, 162.0°E (Figure 3.5c & e). This study expects the exact mechanism as class 3 for uplifted and subsided floors, but unlike class 3, class 4 does not have fractured floors. Class 4—the Fontenelle B crater with a non-flat floor located near class 1a—the Fontenelle D of a nearly flat floor crater is shown in Figure 3.16 and other craters shown in Figure 3.5c and e of class 4 compared to other examples shown for class 1a (example Figure 3.1a, Figure 3.13 & Figure 3.16) suggest class 4 mare-filled craters have undergone diverse post modification processes. Therefore, this study expects mare-filled craters to either preserve their infilling, like class 1a or undergo significant modification, like class 4.

3.4.6 Variations in Central Peak Heights

The mare-filled craters of different diameters with variations in central peak height are shown in Figure 3.17. Mare-filled craters belonging to class 2: the Joliot and the Al-Biruni, have crater diameters of ∼171 km, ∼81 km, and their measured peak height is ∼1950 m, ∼88 m (Figure 3.17a–c). A comparison of these craters shows peak heights are increasing with an increase in crater diameters (Pike, 1977; Krüger et al., 2018), but due to mare-filling, the measured peak heights protruding the mare are smaller than the expected peak heights calculated using empirical relationships (Pike, 1977; Krüger et al., 2018). Other examples of mare-filled craters from class 2 with a central peak are the Maksutov and the Rumford (Figure 3.17d–f). Their diameters are ∼85 km and ∼ 61 km, and their central peak heights are ∼300 m and ∼390 m. In this case, the Maksutov crater has a smaller peak height/ similar to the Rumford crater. The Maksutov (∼85 km) is larger than the Rumford (∼61 km), and it should have a greater peak height (Pike, 1977; Krüger et al., 2018), but it has not. Similarly, numerous measured central peak heights of larger diameter

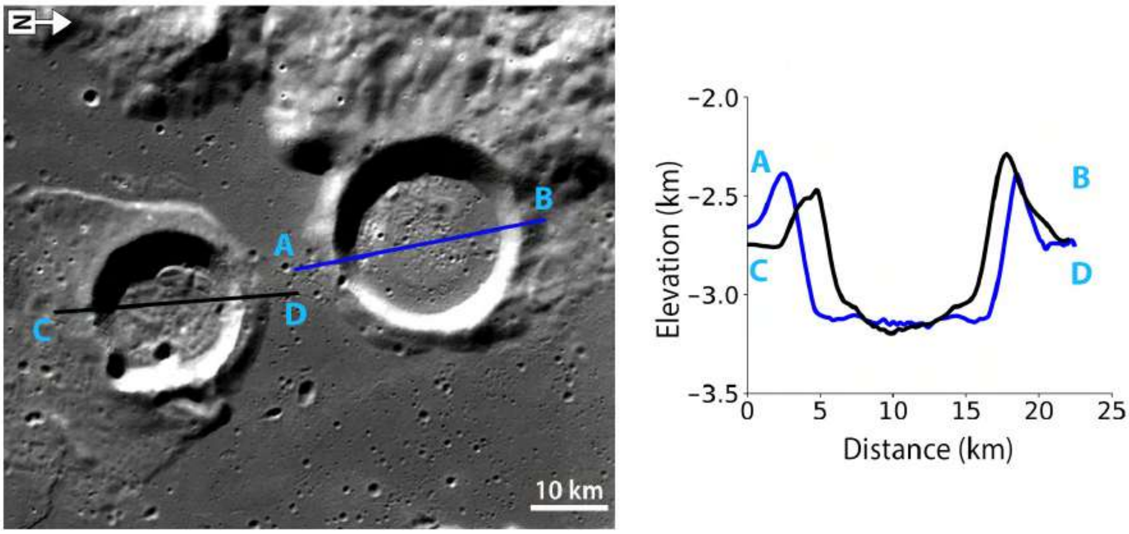

Figure 3.16: An example of mare-filled craters with a nearly flat floor and non-flat floor– the Fontenelle D (62.2°N, 23.4°W, class 1a, solid blue), – the Fontenelle B (62°N, 23°W, class 4, solid black).

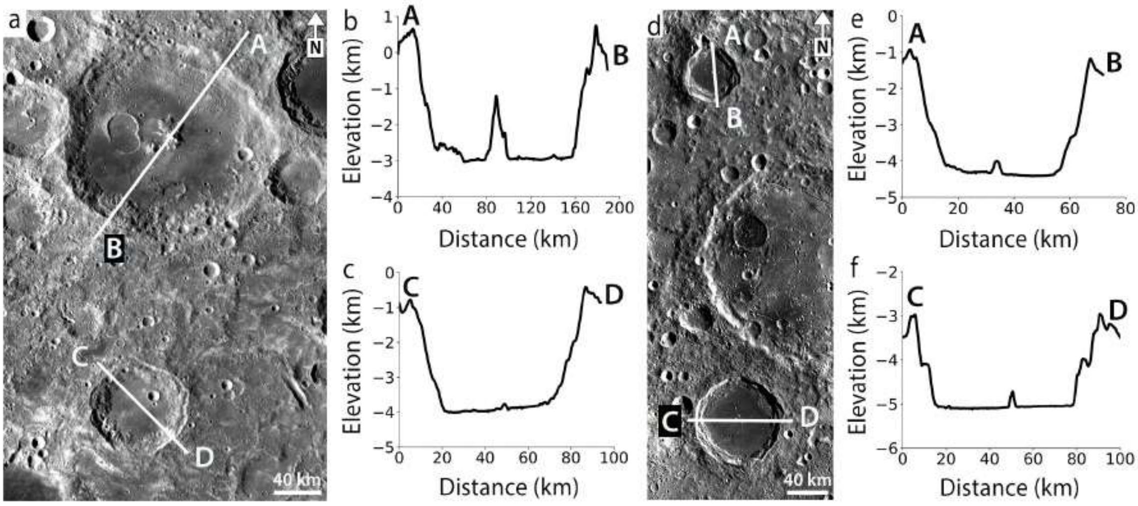

Figure 3.17: A comparative examples of variations in central peak heights of different diameters mare-filled craters: a-c) the Joliot (26°N, 93°E) vs. the Al-Biruni (18°N, 93°E) and their topographic profiles, d-f) the Maksutov(41°S, 169°W) vs. the Rumford(29°S, 170°W) and topographic profiles.

mare-filled craters (Figure 3.8) show similar heights with smaller diameter craters; therefore, this study expects that a massive amount of mare-filling buried a great extent of the central peak in the Maksutov and other mare-filled craters. Hence, this study supposes that the complete absence of peaks in complex craters in classes 1a, and 1b and some from classes 3 and 4 might be completely buried by the infilling magma material. Along with the buried central peak, a few craters with anomalously higher peak heights were observed than the expected height calculated by Pike (1977); Krüger et al. (2018) empirical formulas. Examples of the crater with a greater peak height, along with a schematic of the expected peak height, are shown in Figure 3.18. The Kunowsky crater has ∼1.5 km, the Warmer has ∼2.5 km, and the Jenner has ∼1 km greater peak height than the expected peak height. Such a scenario of anomalous peak height indicates the complex processes of peak modification post its formation.

3.4.7 Hotspots and Frequency Size Distribution

Mare-filled craters are predominantly located on the periphery of the lunar mare/mare-filled impact basins compared to other lunar mare and highlands (Figure 3.6a). Mare-filled craters have a similar distribution as floor fracture craters (FFCs) (Schultz, 1976; Jozwiak et al., 2012). Such distribution is observed when extensive mare-infilling within mare and mare impact basins buries the mare-filled craters, resulting in fewer of these in the mare region than the periphery (Jozwiak et al., 2015). A few mare-filled craters identified within mare regions/basins may be preserved or later formed after extensive mare-filling. Another possible reason for such distribution might be selective infilling on the periphery of the lunar mare/mare-filled impact basins. The existing fractures formed during impact basin formation can provide a pathway for mare-infilling in mare-filled craters located at basin rims (Nahm et al., 2013), and the periphery of the lunar mare generally coincides with the rims of the impact basins (Neumann et al., 2015).

The frequency distribution of mare-filled craters shows 71 mare-filled craters are simple craters (<15 km) (Figure 3.6b), suggesting mare-infilling processes also affect small diameter craters. The vertical depth of fractures associated with these simple craters should be relatively shorter than the vertical depth of impact fractures generated by the complex craters/ impact basins. Even with smaller/shorter fractures, these simple craters were able to bring the lava within the crater from the subsurface. Therefore, this study expects the fractures of these simple craters to intersect the pre-existing deep-rooted impact basin fractures, which contribute to mare-infilling, or these simple craters may possibly impact the pre-existing shallow source (e.g. sill), resulting in mare-filling. Though several craters are mare-filled in the lunar surface, the craters identified in this study merely represent intact rims, and possibly sourced from beneath the crater.

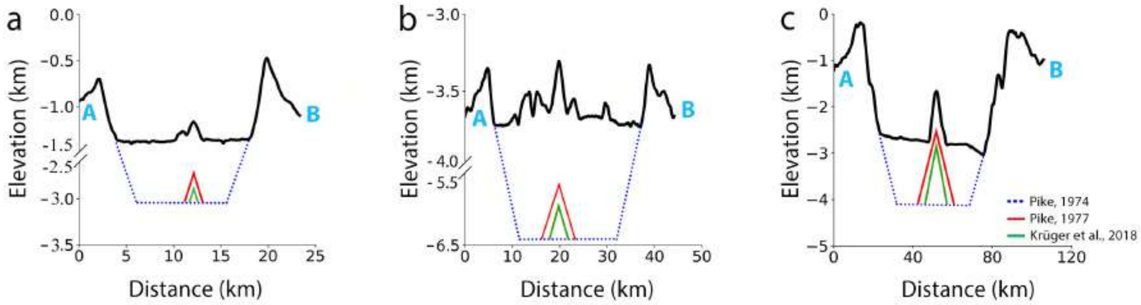

Figure 3.18: Topographic profiles of the mare-filled crater with a greater central peak height than the expected peak height obtained from Pike (1977) (solid red) and Krüger et al. (2018) (solid green) equations and the expected crater depth by Pike (1974) are in dotted blue. a) the Kunowsky topographic profile, for transect AB, refer to Figure 3.13, b) the Warmer topographic profile, for transect AB, refer to Figure 3.15d, and c) the Jenner (42°S, 96°E) topographic profile, for transect AB, refer to Figure AI-1.

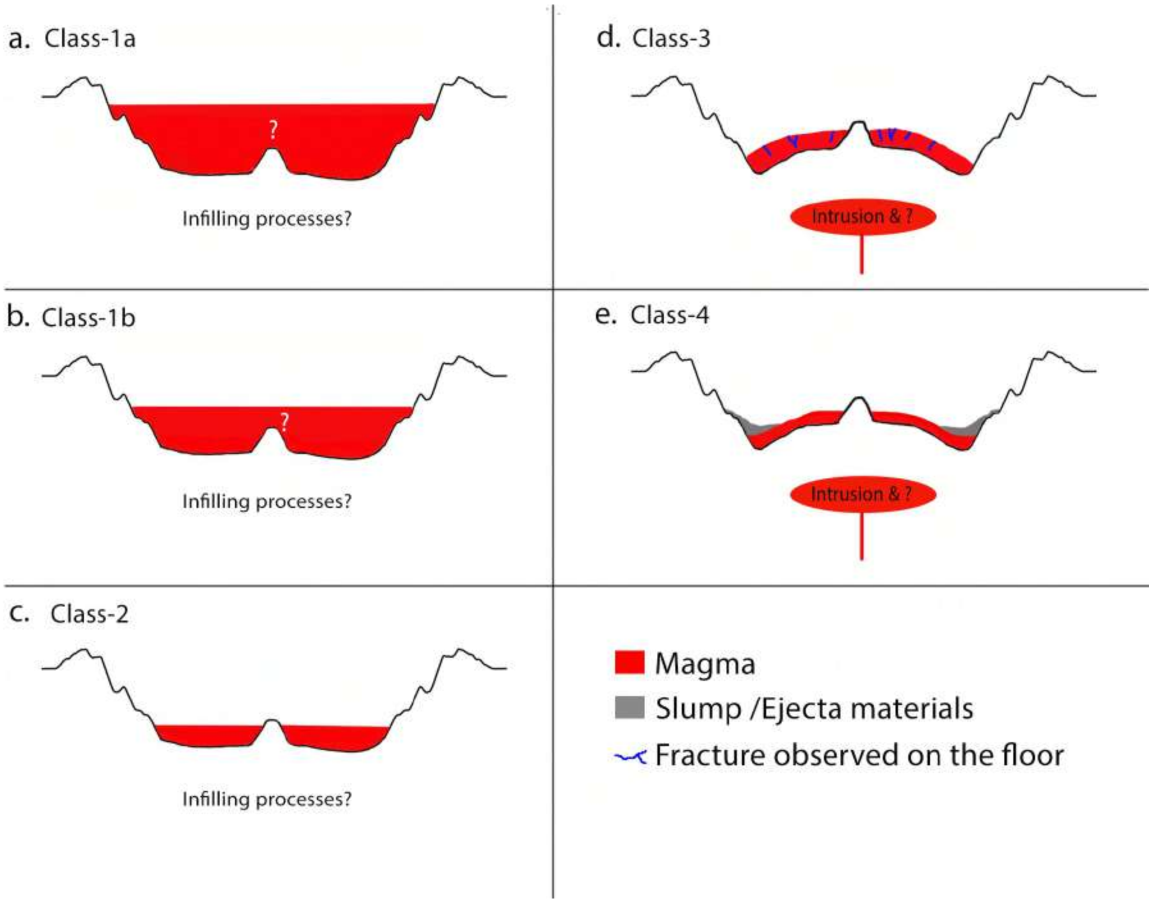

Figure 3.19: An illustration of the characteristics of five different classes of mare-filled craters of ⩾15 km in diameter: a) class 1a, b) class 1b, c) class 2, d) class 3, and e) class 4. Mare-filled craters in classes 1a, 1b, and 2 original floors are shown nearly flat for simplicity, but they can be non-flat, such as the floors of class 3 and some from class 4.

3.4.8 Diverse Ages of Mare Units within Mare-filled crater

Several earlier studies have dated the mare units (Hiesinger et al., 2003, 2011; Morota et al., 2011; Pasckert et al., 2015, 2018) and individual craters filled with mare units (Greenhagen et al., 2016; Shirley et al., 2016; Whitten et al., 2011; Thesniya et al., 2020). Within mare units, the ages are different, which is evidence of multiple episodic events occurring over the region. However, in unconfined mare units, distinguishing the boundary of the mare units for age estimation is tricky. In this study, those craters whose rims are not incised were selected, so the mare units are only from the subsurface, and this gives a hold to date the mare units more comprehensively. This study dated 66 mare units.

The ages obtained in MM-FFC intrigue the most; for example, the Warmer crater is an MM-FFC with mare units resurfacing nearly 54% of the crater floor. The CSFD measurement of the mare unit of the Warmer crater reveals an absolute model age of ~2.4 Ga, suggesting volcanism lasted up to ~2.4 Ga in this crater. However, the age of the FFC is relatively older than this mare unit. This reveals that within the same crater, the activity occurred possibly after the formation of the floor-fractured unit. In another example, the Hansteen floor fractured crater floor is resurfaced by mare unit nearly 18%. The obtained AMA of the mare unit of the Hansteen crater is ~3.0 Ga, indicating the infilling ceased at this age. The Billy crater (class 1a—fully infilled type) is located adjacent to the Hansteen crater. However, the AMA of the mare unit of the nearby Billy crater reported by Hiesinger et al. (2011) is ~1.7 Ga, suggesting the volcanism in this region did not cease at ~3 Ga. The two close-by craters with diverse floor morphology and differences in ages raise the question that class 1a Billy can be earlier an FFC, which plausibly got fully resurfaced by the mare unit. This scenario is consistent because our study shows that mare units resurface nearly 54% of FFC craters. In this regard, it is possible that some of the craters from classes 1a, 1b, 2, and 4 can be earlier FFC and later modified over time. Also, the close vicinity of the Billy and the Hansteen (Figure 3.14) provides an important location where the crater floors are modified at different temporal stages, providing magmatism occurring for an extended period over this region.

This study has also determined an age of ~2 Ga for the Sosigenes (8.7°N, 17.6°E) (Figure AI-4) mare-filled crater containing Irregular Mare Patches

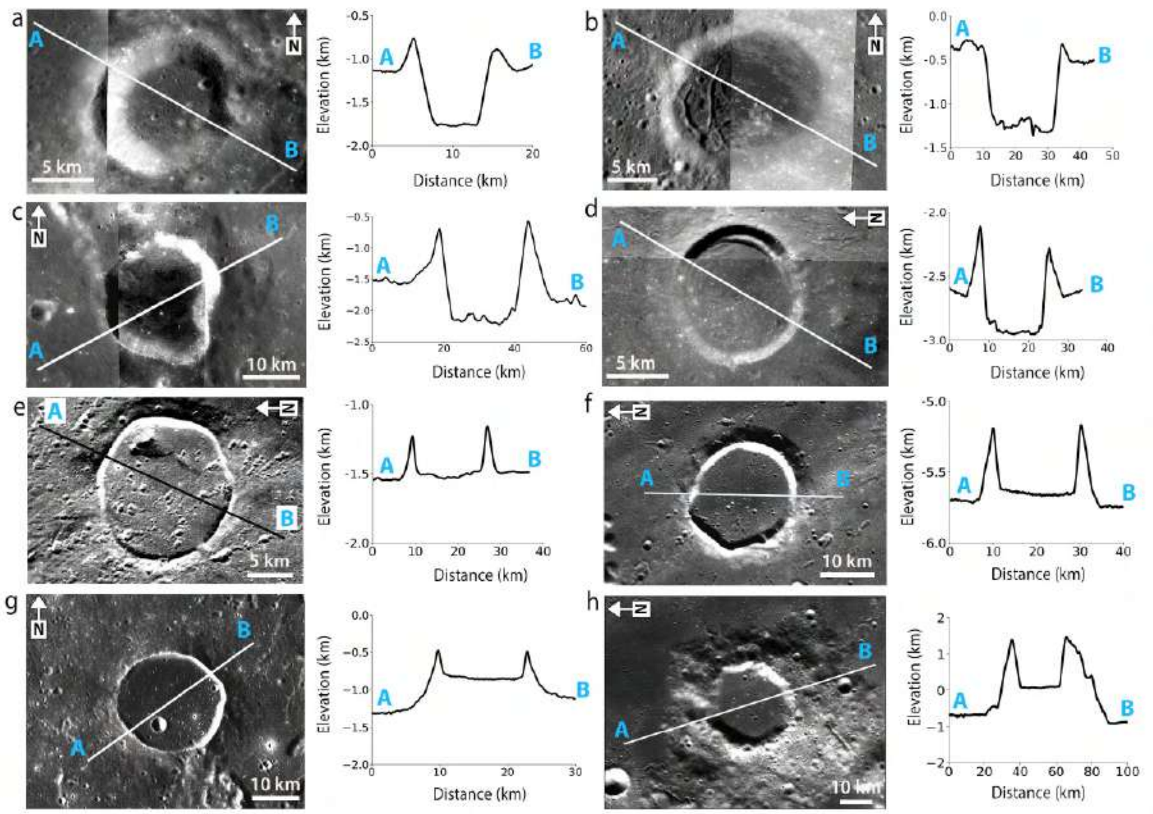

Figure 3.20: Variations in mare-infilling in craters to the surroundings mare are shown in topographic profiles with the Chandrayaan-2 TMC and LROC-WAC images. Examples of variations in mare-infilling in craters: a) the Liebig H (26.3°S, 47.4°W), b) the Crater centred at 26.6°N, 90.2°W, c) the Briggs A (27.1°N, 73.8°W), and d) the Hohmann (17.9°S, 94.3°W) have less infilling; e) the Aristarchus F (21.7°N, 46.6°W) and f) the Leibnitz X (36.7°S, 177.4°E) have similar infilling; g) the Jansen (13.6°N, 28.6°E) and h) the Biot B (20.4°S, 49.6°E) have higher infilling than the surrounding. (Please refer to Table AI-2 for Chandrayaan-2's TMC images IDs.)

(IMPs) (Strain and El Baz, 1980; Schultz et al., 2006; Braden et al., 2014). IMPs are suggested to be results of recent activity and dated younger than 100 million years (Strain and El Baz, 1980; Schultz et al., 2006; Braden et al., 2014).

The plot of absolute model ages (AMAs) vs. mare thickness of ages of mare units shows 52 Imbrian and 14 Eratosthenian mare units (Figure 3.9). The plots show a higher frequency of older mare units than the young mare units. The age data plots indicated that mare-infilling activity peaked in the Imbrian period and declined toward the Eratosthenian period, which is similar to the existing study of lunar mare basalts. The similarity of age distributions between this study and the Hiesinger et al. (2011) study suggests that mare units of mare-filled craters have also recorded the temporal variation of volcanic activity on the Moon like other mare units. In addition, the resurfaced FFCs are typical representative craters for their post-modification after the fracture formation. Such craters are the ones where comprehensive evidence for multiple activities is recorded.

3.4.9 Illustration of Mare-filled craters

Based on observed characteristics and morphometric study of mare-filled craters, we constructed a schematic model of different mare-filled crater classes shown in Figures 3.19, which involves infilling through different processes. Different mare-filled crater classes are observed depending on the amount of lava infilling. With the increasing amount of infilling from class 2 type mare-filled craters with partially buried central peaks, mare-filled craters can evolve into class 1b and class 1a type mare-filled craters with completely buried central peaks (Figures 3.19a-c). Along with different amounts of mare-infilling, mare-filled crater floors are affected by the intrusion (Figures 3.19d & e), which is shown in class 3 and 4 models. Mare-filled crater floors are also affected by subsidence (e.g., Pitatus, 29.9°S, 13.7°W (class 3) and Puiseux, 27.8°S, 39.2°W (class 4)), which are not shown in class 3 and class 4 schematic models to avoid the complications. This study expects infilling or intrusion to be followed by subsidence; it will occur at the end-stage of modification when infilled/ intruded magma cools, resulting in contraction of the volume and subsidence of the crater floor (Wilson and Head, 2018) or due to draining out of the magma (Schultz, 1976; Geshi et al., 2014; Anderson et al., 2019).

3.4.10 Settings and Possible scenarios of infilling in Mare-filled craters

The lava infilling in mare-filled craters varies significantly from simple to complex craters: infilling in some craters is 1) lower than their adjacent surroundings, 2) equivalent to the surrounding, or 3) higher than the surrounding terrain. These variations are more notable in the simple craters than in the complex craters due to their small size, whereas such diversity is not commonly found; however, most of the complex craters host mare-infilling lower than their surrounding units. The variations in mare-infilling within a simple crater are shown in Figure 3.20–example craters in Figures 3.20a-d have relatively less infilling than the surrounding craters in Figures 3.20e and 3.20f, which have similar levels. Such variation in

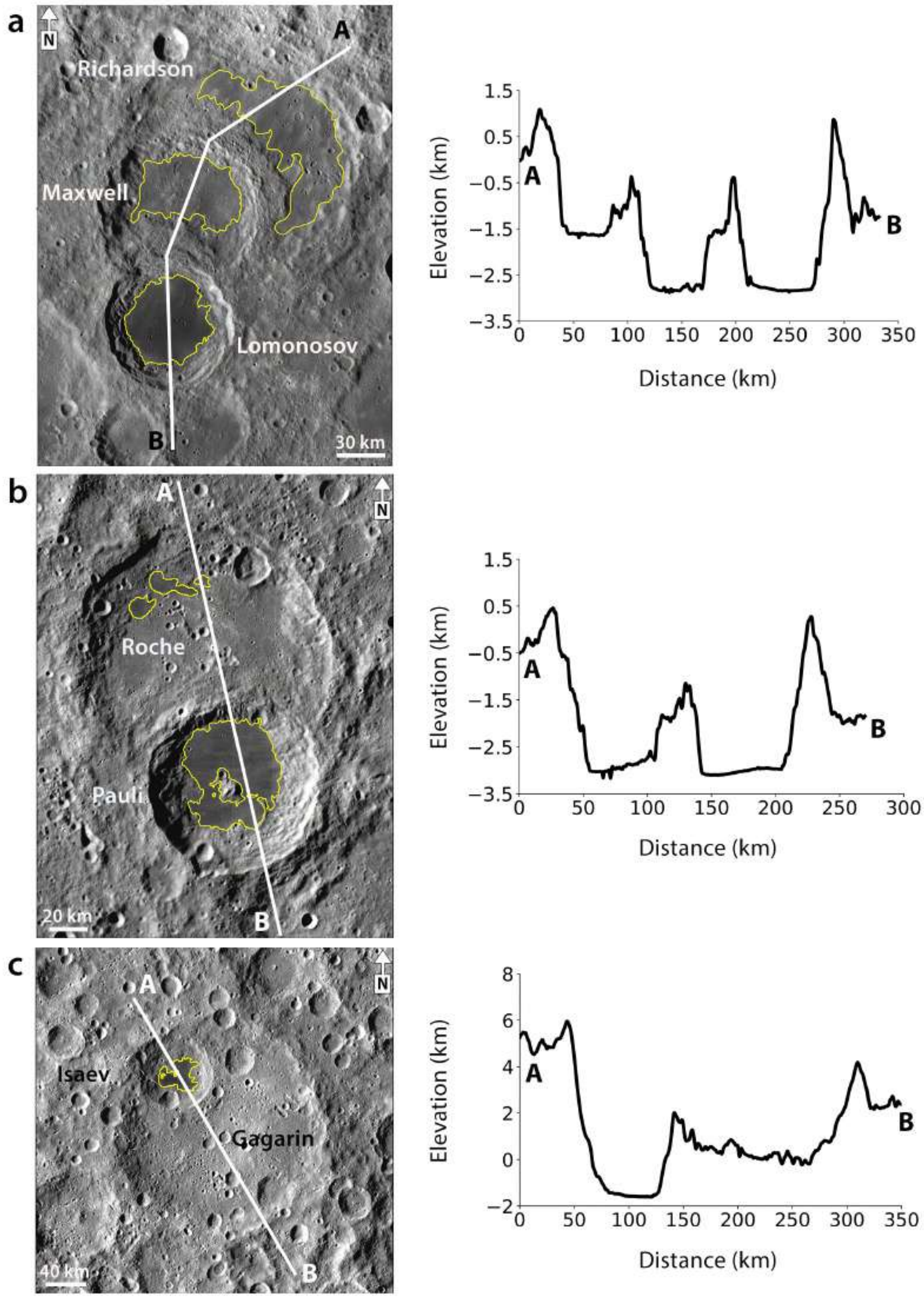

Figure 3.21: Examples of mare-filled craters located in the highlands are: a) the Lomonosov (27.3°N, 98.3°E) superpose the Maxwell (29.9°N, 98.5°E) crater, and the Maxwell superpose the Richardson (30.9°N, 99.9°E) mare-filled crater; b) the Pauli (44.8°S, 137.3°E) superpose on the Roche (42.4°S, 136.5°E) mare-filled crater; c) the Isaev (17.6°S, 147.5°E) mare-filled crater superposing on the Gagarin crater (19.7°S, 149.3°E). The crater depth varies; the underlying craters have shallow crater depths. Such shallow crater depth craters on highlands suggest mare-infilling/intrusion and are currently blanketed by ejecta materials.

infilling could be due to the variation in magma source volume. The crater in Figures 3.20g and 3.20h have higher mare-infilling than the surrounding, raising a question of how this mare erupts on this elevated surface, which is ~1 km above the surrounding mare. In such a case, this study expects a deep-seated fracture fed the crater, or the source was shallow, or the surrounding mare volume shrank more than the confined mare inside the crater.

The Moon has an average crustal thickness between 34 and 43 km, mare regions have a crustal thickness less than the average crustal thickness, and highlands have a greater or equal crustal thickness than average (Wieczorek et al., 2013). The thinner crustal thickness of mare regions will favour eruptions as the excess pressure required for magma to erupt on the surface is smaller than on thicker highlands crust and rims of impact basins, favouring intrusions (Jozwiak et al., 2015; Wilson and Head, 2017, 2018). Therefore, lava infilling is less likely in highland regions, but craters like the Tsiolkovskiy (D ~184 km), Compton (D ~165 km), and Kohlschutter (D ~58 km) located in highland regions have mare-infilling; therefore, this study expects the impact fractures present beneath the crater floor generated by impact processes (Schultz, 1976; Polanskey and Ahrens, 1990; Kumar, 2005; Edwards et al., 2014) plausibly played a role. Other examples of mare-infilled craters on the highlands through impact fractures are shown in Figure 3.21. The Lomonosov crater superposes the Maxwell, and the Maxwell superposes the Richardson mare-filled crater (Figure 3.21a), suggesting the Richardson crater formed earlier, followed by the Maxwell, then the Lomonosov. The absence of a basin and its fractures near these craters indicated that impact fractures created during the Richardson crater formation probably penetrated pre-existing shallow magma sources resulting from intrusion, followed by the Maxwell and Lomonosov impact fractures resulting in the infilling of the craters. The topographic profile of these three craters suggests that the youngest crater, the Lomonosov, has less mare-infilling, whereas the oldest crater among them, the Richardson, has the highest mare-infilling or higher thickness (Table AI-1), suggesting that the older crater had higher infilling in this region. Another possible example of infilling through impact fractures is the Pauli crater superpose on the Roche crater located near the South pole Aitken (SPA) basin (Figure 3.21b). The underlying Roche crater has relatively less mare coverage than the superpose Pauli crater. Again, this study expected the Roche crater fractures to encounter a pre-existing intruded shallow magma source followed by a superposed Pauli crater. In another example, the Isaev crater superposes the Gagarin crater near the SPA basin (Figure 3.21c). Unlike the Isaev and other examples, the Gagarin crater floor is not covered with the mare, but their crater floor depth is relatively shallower than the Isaev crater. Therefore, this study expects the mare within the floor of the Gagarin craters to be completely blanketed by ejecta materials from subsequent impacts. Along with the evidence of mare-infilling through the impact fractures encountering pre-existing intruded shallow magma sources, such craters also suggest that those blanketed by ejecta material with shallow crater floor depths in highland regions can host mare-infilling within them or that such craters provide a pathway for the magma to intrude within the superpose craters.

A study by Michaut and Pinel (2018) of mare-filled craters and FFCs with mare and without mare deposits on the crater floor shows craters with mare deposits on the floors are larger in size than the other FFCs with non-mare-deposits. Their study suggests that crater size controls magma's ability to reach the surface; the larger the crater size, the larger the unloading of surface material, resulting in a decrease in the pressure of its encasing rocks, which satisfies the additional internal excess pressure required for magma to ascent and erupt on the surface. However, the numerical simulations of Ivanov and Melosh (2003) suggest that even a 250–300 km diameter crater cannot raise mantle material by decompression. Hence, preferential magma ascending and stalling in the crust and surface eruption in <250 km diameter FFCs is dubious. Michaut and Pinel (2018) study mostly considered craters of diameter >20 km. The smallest and only crater with a diameter of <15 km is centred at 19.9°N, 66.8°E and has a diameter of ~12 km. It is a rim-breached crater; therefore, the mare deposit on the crater floor can be from the adjacent surroundings. In this study, craters with an enclosed rim were only included. A total of 71 mare-filled craters of diameter <15 km were observed. Therefore, along with the Ivanov and Melosh (2003) study and our observations, we suggest the crater size does not entirely control the ability of the magma to reach the surface.

Although existing studies suggest 1) the structure of impact craters (impact fracture, breccia lens, impact melts) will attenuate the dike movement and will favour intrusions instead of eruptions (Wilson and Head, 2017, 2018), 2) highlands crust favours intrusions (Jozwiak et al., 2015; Wilson and Head, 2017, 2018), and 3) due to unloading of less surface material, infilling in small size craters is not favoured (Michaut and Pinel, 2018). In this study, exceptional cases of infilling of lava in highlands craters and smaller diameter craters ($\leqslant$15 km) were observed. Therefore, this study expects, along with the major role played by internal excess pressure generated fractures (Johnson and Pollard, 1973; Wilson and Head III, 1981; Head and Wilson, 2017; Wilson and Head, 2017), impact-induced surface unloading (Michaut and Pinel, 2018) and basin fractures (Nahm et al., 2013), impact crater fractures formed at the time of the impact process (Schultz, 1976; Polanskey and Ahrens, 1990; Ivanov and Melosh, 2003) could have played a role in ascending, intrusion, and eruption of these magmas in the mare-filled craters.

Based on all the observations, we made a schematic model representing mare-infilling in craters in the highland, at the impact basin rims/periphery of the mare region and within the mare regions on the Moon, which are shown in Figure 3.22. Examples of mare-filled craters in highland regions are Tsiolkovskiy, Compton, and Kohlschutter, and at the impact basin rim are Plato, Posidonius, and Condorcet. Impact fractures probably intersect with the pre-existing shallow magma reservoir (e.g., sills) in these locations, resulting in volcanism (Figure 3.22: C-1, 2). A similar infilling process in craters within the lunar mare/mare-filled impact basins is possible (Figure 3.22: C-3-5), but this study expects infilling in craters on the mare regions/mare-filled impact basins predominantly to occur through over-pressurised dikes due to thin crustal thickness (Jozwiak et al., 2015; Head and Wilson, 2017; Wilson and Head, 2017). Excess pressure at the top of magma exerts elastic stress, which can fracture the overlying rocks and initiate and propagate the dikes (Head and Wilson, 2017; Wilson and Head, 2017). These propagating dikes can directly reach the surface and erupt (Jozwiak et al., 2015; Head and Wilson, 2017; Wilson and Head, 2017). Pre-existing deep-seated fractures formed during basin formation (e.g., Nahm et al. (2013); Andrews-Hanna et al. (2018)) will also contribute to infilling; impact cratering can reactivate the pre-existing deep-seated fractures and result in mare-filling (Figure 3.22: C-2-5). This model also represents different levels of infilling in craters (Figure 3.20): C-3, 4 & 5 craters to the surroundings. Mare-filled crater C-3 (e.g., Figures 3.20a-d) has rela-

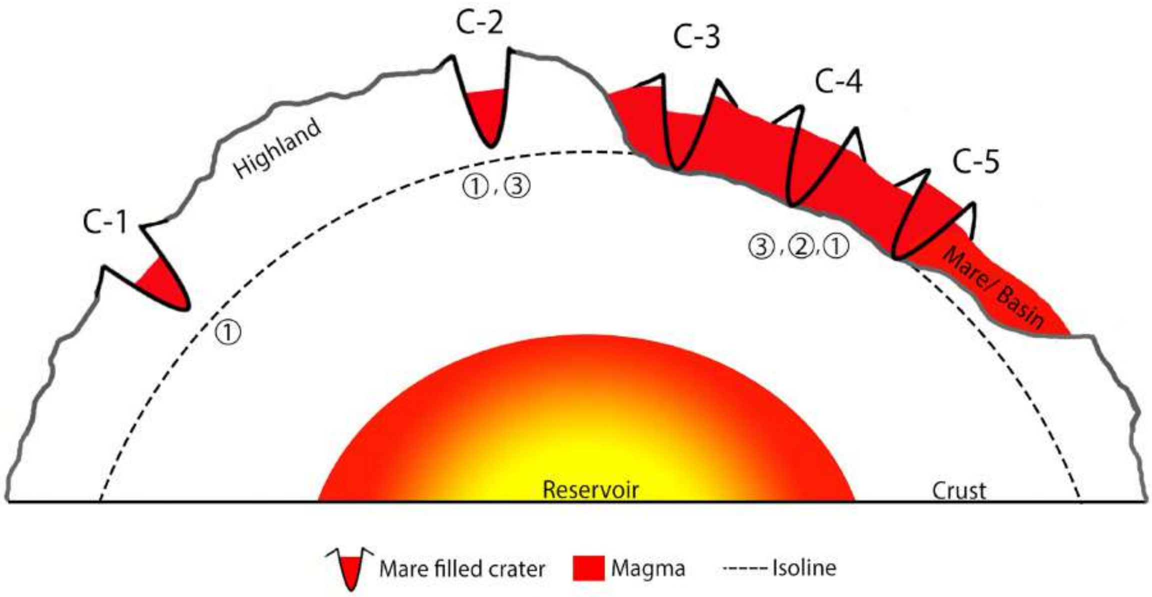

Figure 3.22: A schematic model (not to scale) of Mare-infilling in craters in different geological settings of the Moon: C-1 represents mare-filled craters in the highlands; C-2: craters at the periphery of the basins; and C3 to 5: craters within the mare/basins. C-3 to 5 also represent different levels of lava infilling. Mare-infilling in these craters could be through three different processes: 1) impact fractures puncture the preexisting shallow magma reservoir, 2) overpressurised dikes, and 3) pre-existing deep-seated fractures.

-tively less infilling than the surroundings, C-4 (e.g., Figures 3.20e & f) has similar infilling, and C-5 (e.g., Figure 3.20g & h) has higher infilling than the surrounding.

3.5 Conclusions

The study of impact craters floors modified by mare infilling with unbreached rims reveals the following:

1. The differences in mare-filled craters' morphology are due to differences in the amount of lava infilling and intrusion. Class 1a mare-filled craters have the thickest mare infilling, followed by classes 1b and 2. Class 3 and some mare-filled craters from class 4 morphologies are affected by both intrusion and mare infilling.

2. Mare-modified FFCs refer to craters that have undergone modification by mare activity subsequent to their formation as floor-fractured craters. These craters suggest that the same crater witnessed multiple

episodes of magmatism. It raises the question of whether completely filled mare craters may represent previous FFCs.

3. We made two observations:

   (a) Mare-filled craters on the highlands. The previous studies suggest the highland crust favours intrusions rather than volcanism (Wilson and Head, 2017, 2018).

   (b) Lava infilling in 71 small craters (D $\leqslant$15 km). The study by Michaut and Pinel (2018) favoured infilling in larger craters (D $\geqslant$15 km).

   Based on these observations, we suggest that the impact fractures with internal excess pressure and impact-induced surface unloading played a significant role in ascending, intrusion, and eruption in mare-filled craters.

4. In this study, nearly 50% of the mare-filled craters are located within the rims of impact basins; hence, we suggest basin fractures have played a significant role in lava infilling in the mare-filled craters located at the rims of the basin.

5. Mare-infilling in simple craters could be sourced from the shallowest stalled recent magma reservoirs as fractures generated during simple craters formation should be relatively shorter in depths than those generated by the complex craters/ impact basins. Such mare-filled small craters can be potential sites for understanding shallow stalled magma reservoirs.

The analysis of mare-filled craters within 17% (Nelson et al., 2014) of the lunar surface can be applied to the highland regions, whose craters' floor depths are relatively shallow. Highlands' craters with shallow crater floor depth may host mare infilling within them, but they are successively mantled by ejecta materials. Overall, this study suggests the fractures generated during the impact cratering provide pathways for the magma to intrude and extrude within the crater floor, along with dike and deep-seated fractures.

Chapter 4

Posidonius Crater Region:

Insights from Cratering, Magmatism & Tectonism Interaction

4.1 Introduction

The Posidonius crater is located in the northeastern region of the ~3.98 Ga-old Mare Serenitatis basin (Head III, 1979; Neukum, 1984). Prior investigations of the Posidonius crater region have identified several deformational features associated with both magmatism and tectonism. These deformational features include a fractured floor resulting from magma intrusion (Schultz, 1976; Jozwiak et al., 2012), a mare-filled floor due to magma extrusion (Kimi et al., 2023) and a sinuous rille caused by lava flow (Hurwitz et al., 2013). Additionally, the crater region displays various tectonic deformational features associated with blind thrust faults—wrinkle ridges (Thompson et al., 2017) and lobate scarps (Watters et al., 2015) formed under compressional stress, along with small-scale graben (French et al., 2015) formed due to extensional stress. Generally, small-scale grabens are typically formed under extensional stress, resulting from flexural bending while forming wrinkle ridges and lobate scarps (Plescia and Golombek, 1986; Watters et al., 2010). In the case of Posidonius, they are suggested to form due to uplift from magmatic intrusion linked to Floor-Fractured Craters (FFCs) formation (French et al., 2015). These small-scale grabens within the Posidonius crater region contain tectonic pits formed by collapse and drainage into subsurface fault zones (French et al., 2015). They cross-cut partially degraded small-diameter craters, suggesting a maximum age between late Eratosthenian and early Copernican (French et al., 2015).

Based on previous research, it is evident that the Posidonius crater region exhibits a diverse range of deformation features arising from impact

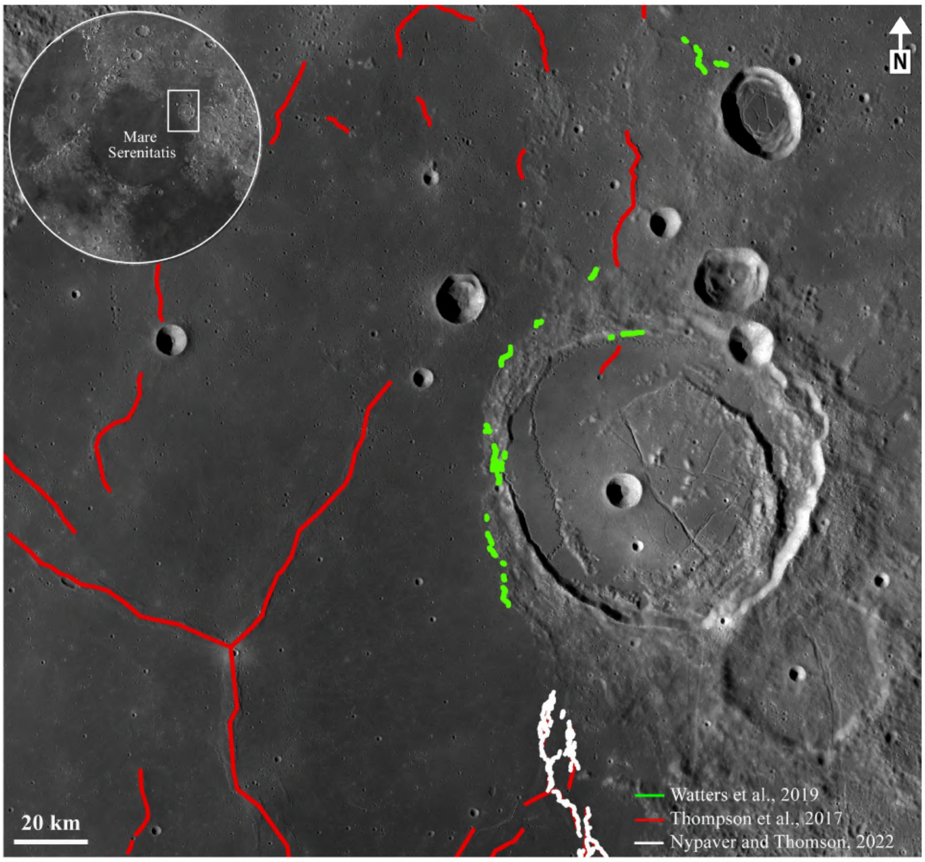

Figure 4.1: An overview of the study area with reported lobate scarps by Watters et al. (2019) (neon green), wrinkle ridges by Thompson et al. (2017) (red) and Nypaver and Thomson (2022) (white) overlaid on the LROC-WAC mosaic.

cratering, magmatism, and tectonism. This setting presents an excellent opportunity to study the interaction between these processes. Despite extensive previous studies, there remains a notable gap in our understanding of how these processes interact in this study area (Figure 4.1). The objective of this study is to investigate the interactions between these processes and examine the resulting deformational features and subsurface faults. To accomplish this objective, we have outlined specific goals:

1. Mapping the distribution of tectonic features in the study area to identify potential locations where tectonic activity likely occurred in the recent and past.

2. Investigation of the formation of small-scale graben: resulting from flexural bending during movement along a blind thrust fault or the magma intrusion uplift.

3. Examine the transition of wrinkle ridges and lobate scarps to seek a

better understanding of the subsurface blind thrust fault in the study area.

4. Determine the ages of deformed features to unravel geological events in the study area.

5. Investigate the formation of the Rimae Posidonius by lava flow or complex processes (intrusion, subsidence, and blind thrust fault).

4.2 Methodology

4.2.1 Datasets

This study used various high-resolution imaging datasets for data acquisition and analysis purposes. These datasets included Lunar Reconnaissance Orbiter Camera (LROC)-Wide Angle Camera (WAC) image of spatial resolution ~100 m/pixel (Robinson et al., 2010), LROC-Narrow Angle Camera (NAC) images of spatial resolution ~0.5–2 m/pixel (Robinson et al., 2010), Chandrayaan (CH2) Terrain Mapping Camera (TMC2) with spatial resolution ~5 m/pixel (Chowdhury et al., 2020), and Selenological and Engineering Explorer (SELENE)-Terrain Camera (TC) with spatial resolution ~10 m/pixel (Haruyama et al., 2008). These datasets were utilised for the identification and mapping of deformed structures as well as for crater counting. The IDs for the NAC images utilised in this study are listed in Table AII-1. Furthermore, elevation and slope measurements were conducted using a merged dataset of the Lunar Orbiter Laser Altimeter (LOLA) and Selenological and Engineering Explorer (SELENE)-Terrain Camera (TC) digital elevation model (DEM) with a spatial resolution of ~59 m/pixel and a vertical resolution ~3–4 m (SLDEM2015) (Barker et al., 2016).

4.2.2 Mapping and Measurements

We started by exploring the deformed structures using the LROC Quickmap web interface (https://quickmap.lroc.asu.edu/) base map of WAC+NAC+NAC_ROI_MOSAIC. NACs with a large incidence angle ranging from 55° to 80° east and west were primarily used for exploration as they are the most effective. Then, using georeferenced NAC images obtained from PILOT (https://pilot.wr.usgs.gov/) in ArcGIS 10.5 software, tectonic features that were not previously documented within the study area were systematically mapped, including wrinkle ridges, lobate scarps, small-scale graben, tectonic pits, crosscut craters by wrinkle ridges, lobate scarps, and small-scale graben, followed by measurements of the lengths and azimuths of the linear structures. Additionally, we utilised shapefiles of previously mapped deformed structures (lobate scarps, wrinkle ridges, and deformed craters by wrinkle ridges) in the study area for our reference (Watters et al., 2015; Thompson et al., 2017; Nypaver and Thomson, 2022). In this study, orthographic projection was employed. We mapped the linear to sinuous compressional structures associated with the mare as wrinkle ridges (Plescia and Golombek, 1986), those linear to arcuate compressional structures associated with the highlands as lobate scarps (Watters, 1993; Watters et al., 2015), and linear and narrow openings as small-scale graben (Watters et al., 2012). Then, the diameters of the craters deformed by wrinkle ridges, lobate scarps, and small-scale graben were measured using CraterTools (Kneissl et al., 2011).

4.2.3 Crater Size-Frequency Distribution (CSFD)

Crater size-frequency distribution (CSFD) measurements were employed to estimate model ages of deformed structures using the traditional crater counting (TCC) method, the plugin feature in CraterTools (Kneissl et al., 2011). The deformed structures include the hanging wall of wrinkle ridges and lobate scarps and the footwall of a few lobate scarps, and the lava-filled and fractured floor of the Posidonius crater floor. The delineation of elongated polygons/ count area over the hanging wall and footwall was determined by factors including slope, the availability of NAC images with suitable illumination conditions for crater counting, the availability of NAC images with the same ID of an entire scarp and segments of scraps where they begin to splay were not considered. While demarcating counting areas of hanging and foot walls, similar slope gradients were selected. In this study, slopes $\geqslant 10^{\circ}$ were avoided due to the potential for young model age resulting from mass wasting effects (Basilevskii, 1976; Meyer et al., 2018). However, in some instances, we had to work with slopes $\geqslant 10^{\circ}$, reaching a maximum of 25°, as slopes $\leqslant 10^{\circ}$ were unavailable in our location. The approximate maximum slope within each count area is listed in Table AII-2. After demarcating the count area of deformed structures, the diameter of all postdating craters was measured using the three-point crater digitising method. While mapping, the secondary (chain of craters) craters were omitted. Then, the .scc files were exported for analysis in CraterStats II (Michael and Neukum, 2010). The imported .scc files in CraterStats II (Michael and Neukum, 2010) were used to derive the model ages using the lunar production and chronology functions of Neukum et al. (2001). The CSFDs were plotted in both cumulative and relative (R-plot) forms Van Der Bogert et al. (2018). Poisson age determination (PDF) and cumulative fits (CumF) were both employed in estimating the ages Michael et al. (2016); Van Der Bogert et al. (2018). Additionally, we did the standard deviation of adjacent area (SDAA) randomness analysis to identify the clusters of secondary craters Michael et al. (2012) and applied cumulative resurfacing correction to one of the ages to enhance the derived model ages. We assumed that the counted craters formed after the wrinkle ridges and lobate scarps and that any pre-existing craters were entirely erased during deformation. However, since the rate of deformation remains uncertain, it is difficult to confirm whether all older craters were fully reset. This uncertainty could affect the reliability of the derived model ages.

4.3 Results

4.3.1 Wrinkle Ridges

In and around the Posidonius crater, 384 segments of wrinkle ridges were mapped, whose total length summed up to ~808 km (Figure 4.2a). They are mainly oriented in the north direction (Figure 4.3a). Nearly 83% (~672 km) of the mapped wrinkle ridges in the study area are new, and only ~17% (~136 km) overlap with the previous studies (Thompson et al., 2017; Nypaver and Thomson, 2022).

The wrinkle ridges inside and outside the crater were mapped separately. Within the crater, ~6% (~48 km) of wrinkle ridges were observed on the crater floor (Figure 4.4a), mainly on the western part of the resurfaced floor. Some of those wrinkle ridges deformed 6 craters, whose diameters range from ~90 m to ~1.6 km (Figure 4.4b). Outside the crater, ~94% (~760 km) of wrinkle ridges were observed, and they are distributed to the north, west, and south of the crater (Figure AII-1). Among these, ~50% (out of 94%) are located in the southern region of the Posidonius crater, making it the most populated region of wrinkle ridges (Figure 4.4c). The wrinkle ridges outside the Posidonius crater deformed 406 small diameter

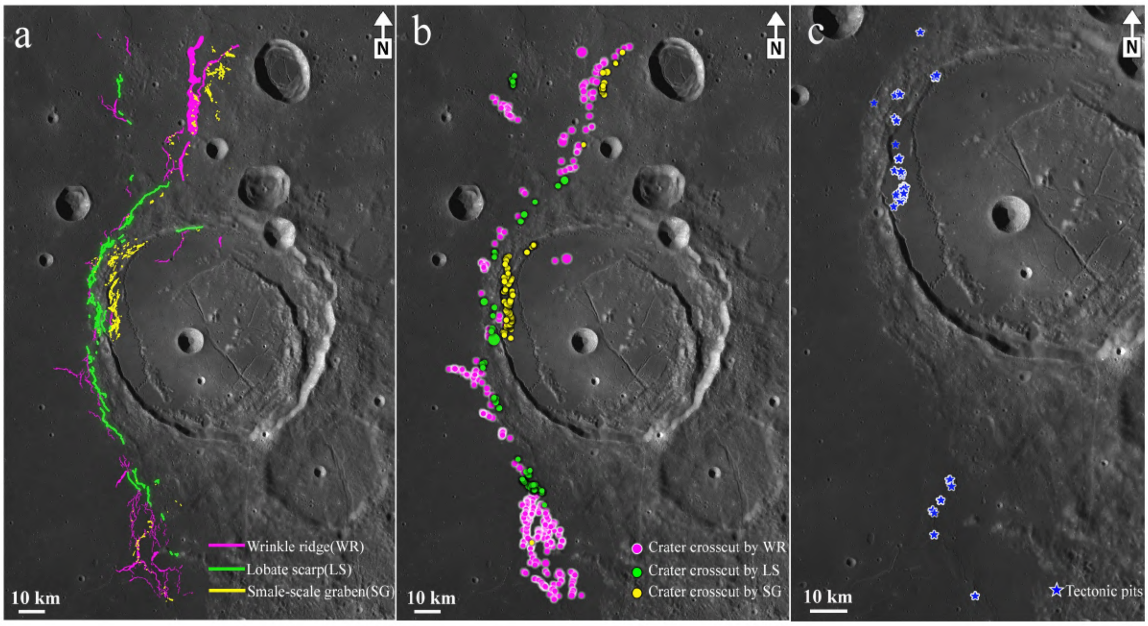

Figure 4.2: Mapped deformed structures overlaid on the LROC-WAC mosaic. a) Distribution of mapped wrinkle ridges (pink), lobate scarps (neon green), and small-scale graben (yellow). b) Distribution of deformed craters by wrinkle ridges (pink), lobate scarps (neon green), and small-scale graben (yellow). c) Distribution of tectonic pits (blue).

craters, whose diameters range from ∼20 m to ∼1.9 km (Figure 4.4d). Overall, this study observed 412 craters deformed by wrinkle ridges within and outside the Posidonius crater (Figure 4.2b), and their frequency distribution plot is shown in Figure 4.3b.

4.3.2 Lobate Scarps

A total of 206 segments of lobate scarps were mapped, whose total length is ∼286 km in and around the Posidonius crater (Figure 4.2a). They are mainly oriented towards the north (Figure 4.3c). Nearly 77% (∼219 km) of the mapped lobate scarps in the study area are new, and only ∼23% (∼67 km) overlap with the previous studies (Watters et al., 2015, 2019). About 8% (∼23 km) of mapped lobate scarps are located at the inner walls of the Posidonius crater (Figures 4.5a and 4.5b). Other remaining ∼92% (∼263 km) of lobate scarps are mapped along the transition of the Mare Serenitatis basin floor to the Posidonius crater rim in the north, west, and south (Figures 4.5c, 4.5d and Figure AII-2). Apart from the craters deformed by wrinkle ridges outside the Posidonius crater, this study observed 55 craters are deformed by lobate scarps whose diameters range from ∼30 m to ∼2.6 km (Figures 4.2b, 4.5d and Figure AII-2c&d). The frequency distribution plot for craters deformed by lobate scarps is shown in 4.3d.

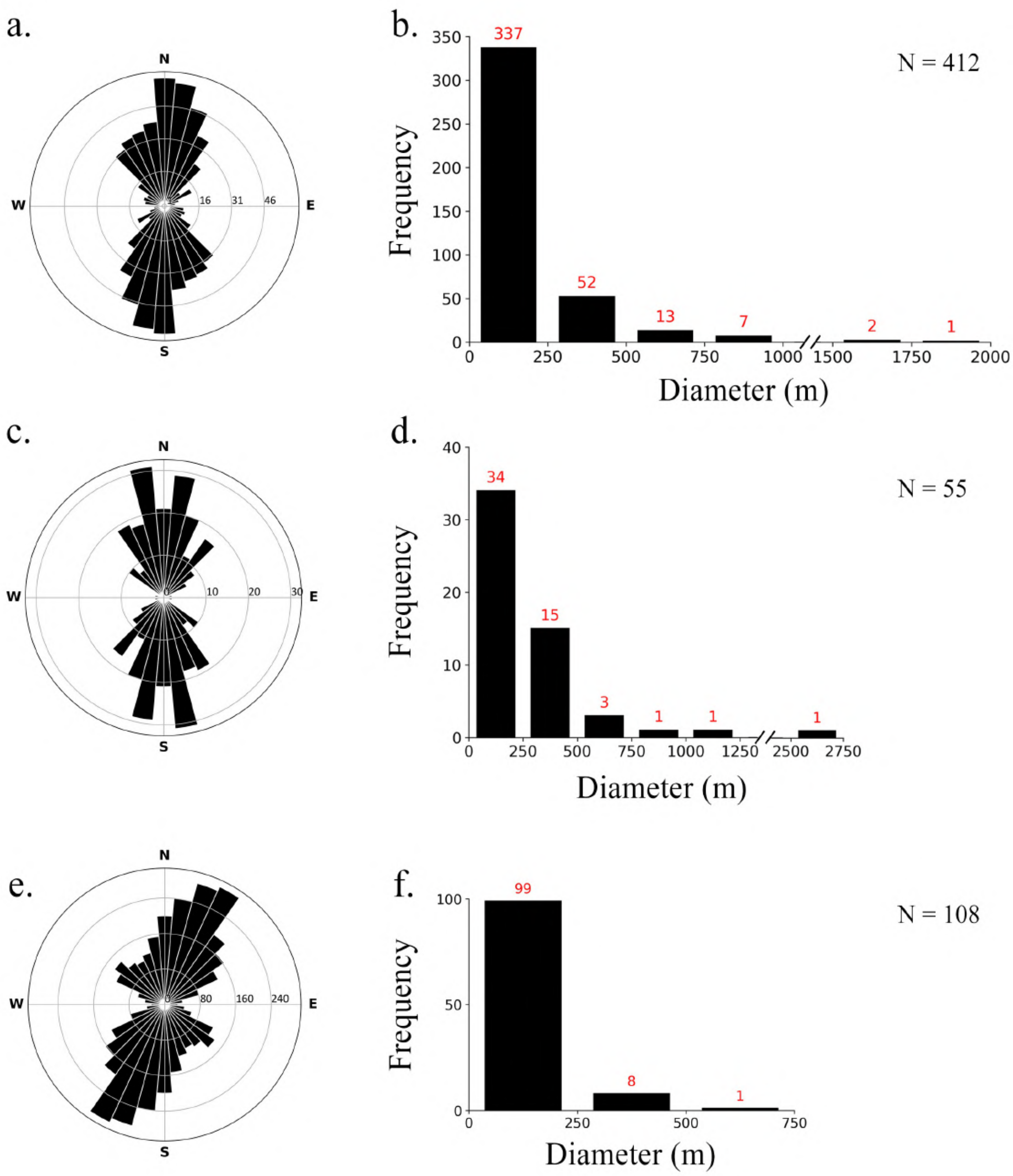

Figure 4.3: Rose diagrams showing the orientations of a) Wrinkle ridges, c) Lobate scarps, and e) Small-scale graben. Size frequency distribution of craters deformed by b) Wrinkle ridges, d) Lobate scarps, and f) Small-scale graben.

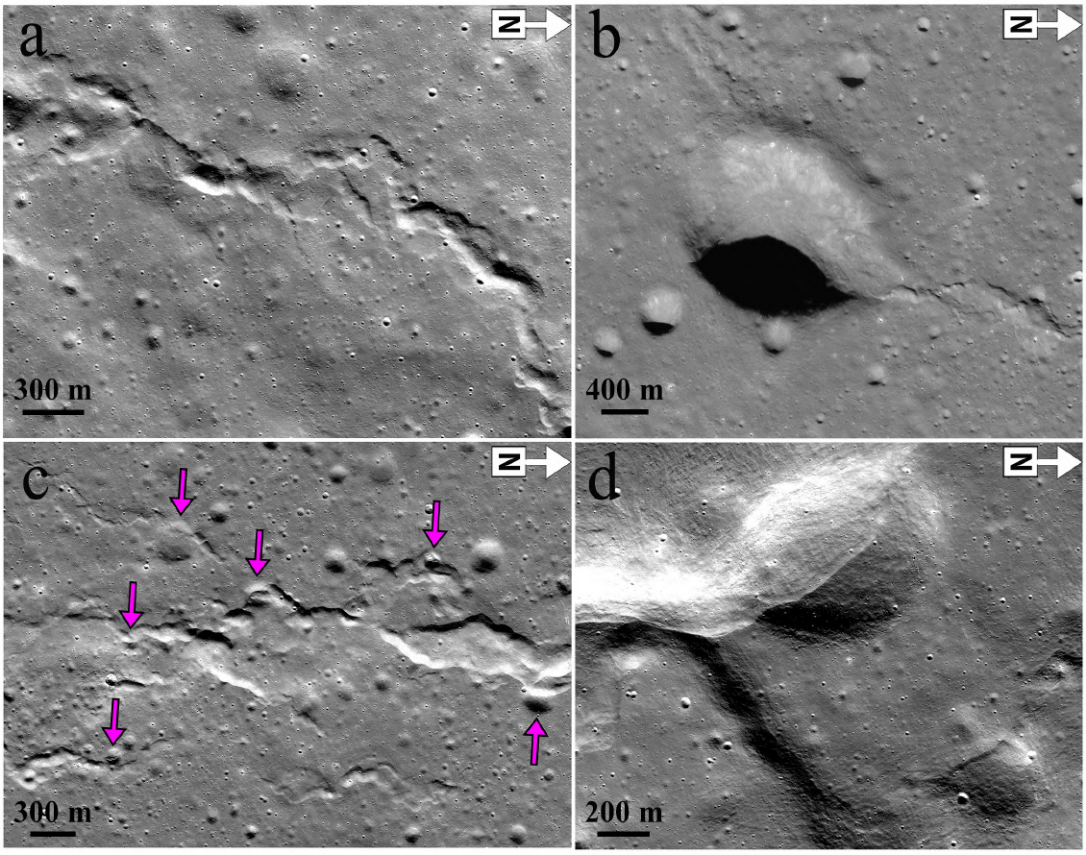

Figure 4.4: LROC-NAC images of wrinkle ridges and deformed craters by wrinkle ridges. a) Mapped wrinkle ridge (M1154030547RE) and b) deformed crater (M1108017413LE, M1108017413RE) on the floor of Posidonius crater. c) Mapped wrinkle ridge (M1199932087RE) to the south of the Posidonius crater and deformed craters marked in pink arrows. d) Deformed crater (M1199924943LE) mapped north to the Posidonius crater.

4.3.3 Small-Scale Graben

The Posidonius crater and its surroundings also host small-scale graben, apart from the wrinkle ridges and lobate scarps. We have identified and mapped 2523 segments of small-scale graben whose total length spans ~346 km (Figure 4.2a) in the study area. They are mainly oriented in the northeastern direction (Figure 4.3e). Almost 86% (~296 km) of the mapped small-scale graben in the study area are new, and only ~14% (~50 km) coincide with the previous study (French et al., 2015).

Like wrinkle ridges and lobate scarps, small-scale graben were mapped inside and outside the crater separately. Nearly 33% (~115 km) of them were mapped (Figure 4.6a) inside the Posidonius crater, which crosscuts 75 craters of diameters ranging from ~20 m to ~400 m (Figure 4.6b). Most of the mapped small-scale graben inside the Posidonius crater are located

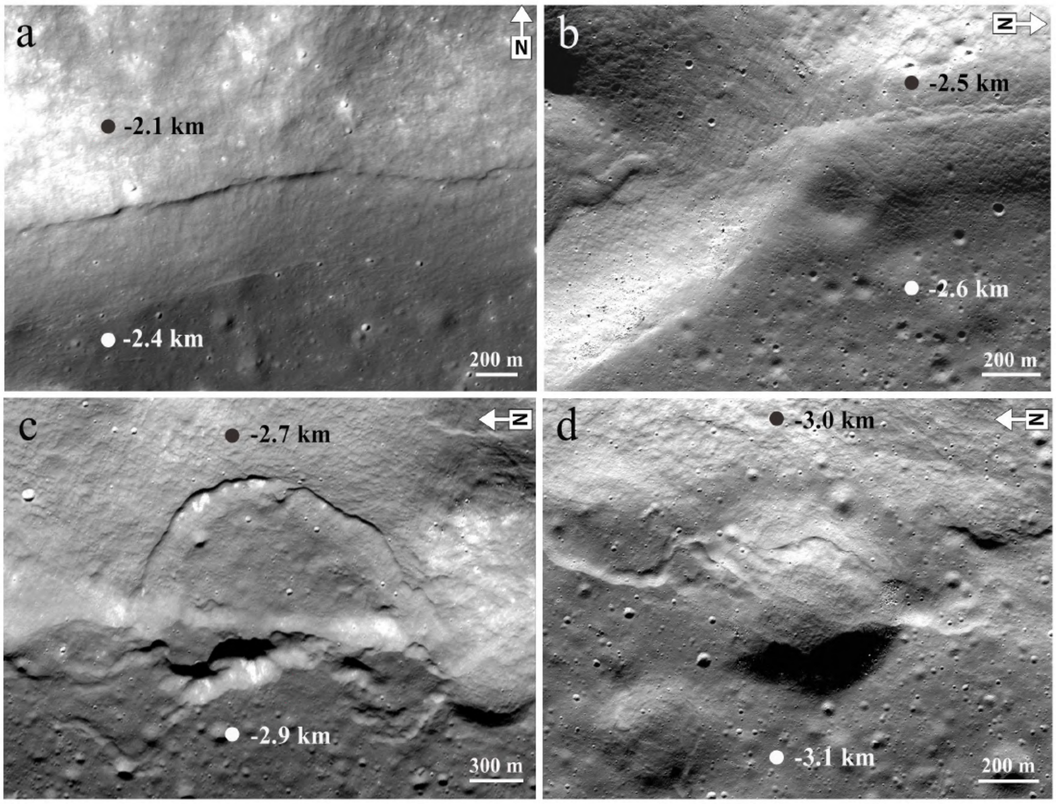

Figure 4.5: LROC-NAC images of lobate scarps and deformed crater by lobate scarp. a) Mapped lobate scarp at the north (M1108017413LE) and b) western (M1157563796RE) walls of the Posidonius crater. c) A mapped lobate scarp between the northeastern Mare Serenitatis basin floor and the Posidonius crater's western rim (M1096379115LE). d) Deformed crater by lobate scarp between the Mare Serenitatis basin floor and the northwestern rim of Posidonius crater (M1188164347RE).

at the elevated part of the northwestern floor (Figure 4.7). Around 1% (~3 km) of small-scale graben are formed at the crater wall (Figure 4.6a (black arrow) and Figure AII-3). Outside the crater, ~66% of small-scale graben were mapped. About 22% (~75 km) out of 66% were mapped at the northwestern rim of the Posidonius crater. The remaining ~38% (~133 km) were mapped to the north (Figure 4.6d and Figure AII-1e) and ~6% (~20 km) to the south outside of the Posidonius crater (Figure 4.6c and Figure AII-1c). These observations revealed that most of the mapped small-scale graben outside the Posidonius crater are located next to or on the crest of wrinkle ridges, suggesting a younger formation age than the wrinkle ridge. Due to their small size, small-scale grabens do not persist on the surface for extended periods. Many suggested their formation younger than 50 Ma (Watters et al., 2012; French et al., 2015). Small-scale graben outside the Posidonius craters crosscut 33 craters of diameters ranging from ~0.03 km

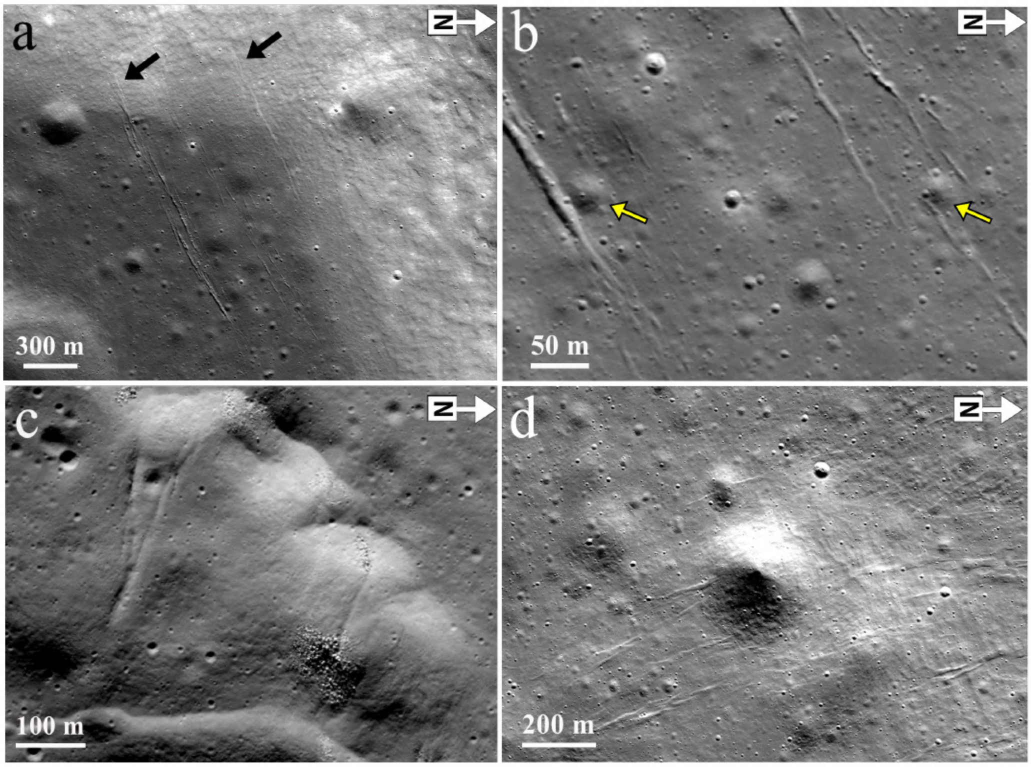

Figure 4.6: LROC-NAC images of small-scale graben and deformed craters by small-scale graben. a) Small-scale graben (M1108088900LE) on the northwestern floor and wall (black arrow) of the Posidonius crater; and b) deformed craters by these graben (yellow arrow) (M1108088900LE). c) Small-scale graben formed on the wrinkle ridge south of the Posidonius crater (M180980846LE). d) Deformed craters by graben located north of the Posidonius crater (M1199924943LE).

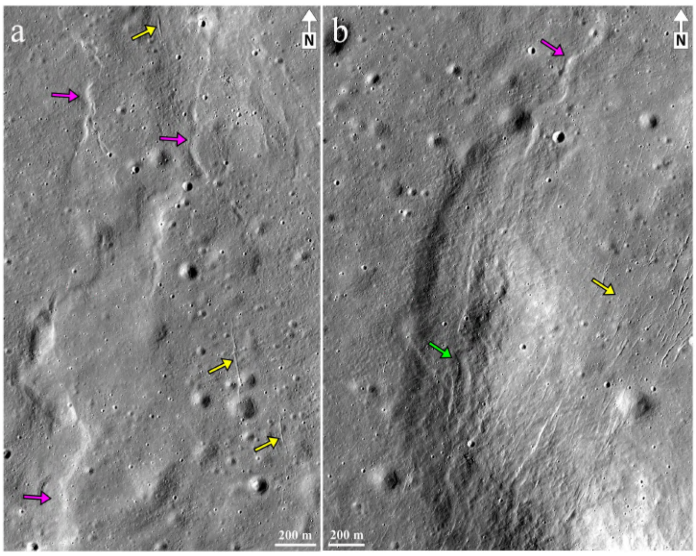

Figure 4.7: LROC-NAC images of western Posidonius floor a) wrinkle ridges (pink arrows) and the small-scale graben (yellow arrows) (M1154037629RE), and b) wrinkle ridge and lobate scarp (green arrow) transition and the associated small-scale graben (M1154037629RE).

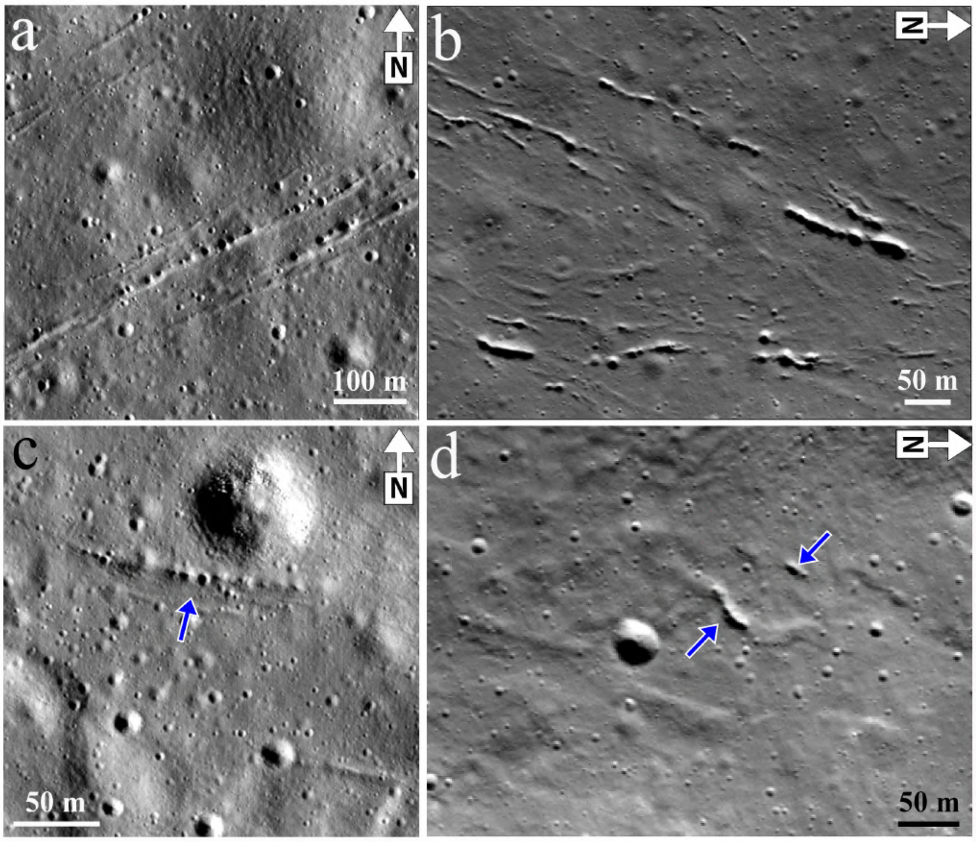

Figure 4.8: LROC-NAC images of tectonic pits formed within the small-scale graben. a) (M1188164347RE) and b) (M1182289525LE) are tectonic pits mapped on the floor of the Posidonius crater. Tectonic pits mapped c) at the southern surrounding of Posidonius (M165659105RE) and d) at the rim of the Posidonius crater (M1154037629RE).

to 0.6 km (Figure 4.6d). In total, small-scale graben crosscut 108 craters (Figure 4.2b) in the study area, and their frequency distribution plot is shown in Figure 4.3f.

4.3.4 Tectonic Pits

French et al. (2015) reported the tectonic pits present within the graben in the study area, but they were not mapped. Here, we mapped tectonic pits using LROC-NAC images that are available in the study area. A total of 269 tectonic pits were mapped that formed within the small-scale graben (Figure 4.2c). About 71% (192) were mapped on the western floor of the Posidonius (Figures 4.8a and 4.8b). Outside the crater, ∼10% (27) are mapped on the north-western rim of the Posidonius crater (Figure 4.8d). The remaining ∼19% (50) are observed south of the Posidonius crater, out of which few are observed within the small-scale graben that are associated with the wrinkle ridges (Figure 4.8c).

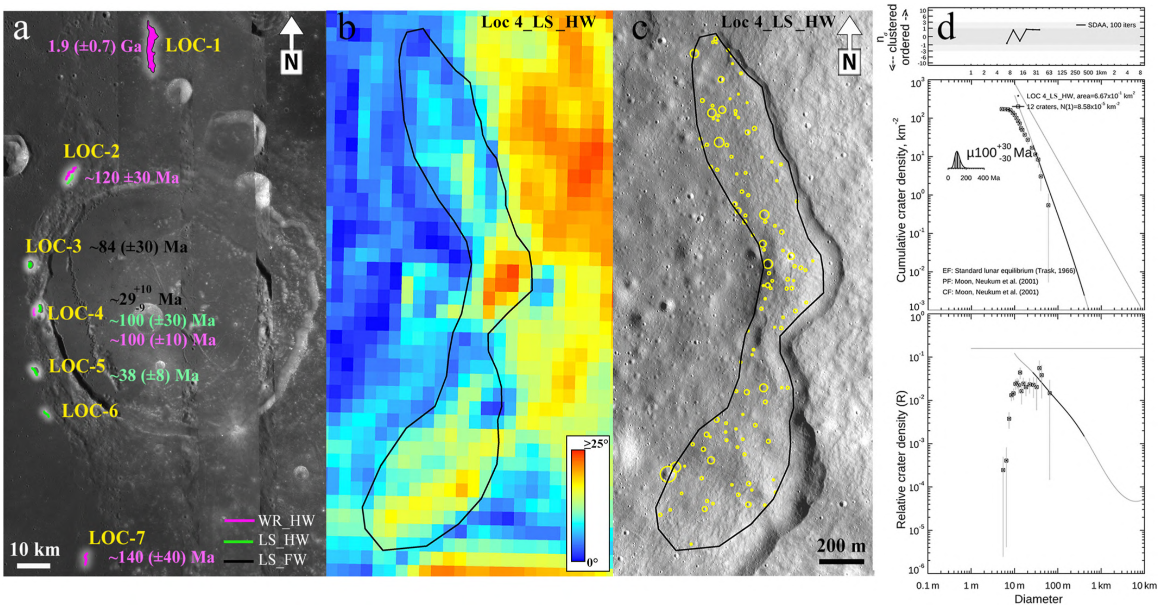

Figure 4.9: (a) An overview of the ages and locations for four segments of wrinkle ridges hanging wall (WR_HW) (pink), five segments of lobate scarps hanging wall (LS_HW) (neon green), and three segments of lobate scarps footwall (LS_FW) (black). The ages are overlaid on the LROC-WAC mosaic and TMC2. Note. Areas where the CSFD reached equilibrium are left blank. (b) Slope map of Location 4's lobate scarp, (c) Count area of Location 4's lobate scarp hanging wall, and (d) cumulative and relative crater frequency plots showing the model age determined using Poisson timing analysis. (Please refer to Table AII-3 for Chandrayaan-2's TMCs images IDs. Figure AII-4 for details of other location plots)

4.3.5 Model Ages

For estimating the model ages of the deformation, we considered four segments of wrinkle ridges hanging wall, five segments of lobate scarps hanging wall, three segments of lobate scarps footwall, and the Posidonius crater floor (Figure 4.9 and Figures AII-4, AII-5 and Table AII-2). The obtained age using the crater counting technique of wrinkle ridges hanging wall ranges from $\sim$100 $\pm$10 Ma to $\sim$1.9 $\pm$0.7 Ga, and lobate scarps hanging wall and footwall range from $\sim 29^{+10}_{-9}$ Ma to 100 $\pm$30 Ma. The range of estimated model ages suggests multiple episodes of tectonic activities spanning from late Eratosthenian to Copernican periods in the study area. The ages of wrinkle ridges and lobate scarps closer to Posidonius are younger ($\sim 29^{+10}_{-9}$ Ma to $\sim$120 $\pm$30 Ma) (Figure 4.9: loc-2 to loc-6) than those farther away ($\sim$140 $\pm$40 Ma and $\sim$1.9 $\pm$0.7 Ga) (Figure 4.9: loc-1 and loc-7), indicating that there has been more recent activity near Posidonius than in distant areas.

All these deformations occurred over a lava-resurfaced floor whose age tends to be $\sim 2.8^{+0.4}_{-0.5}$ Ga (Figures AII-5a and AII-5b). The non-resurfaced, fractured floor is estimated to be $\sim 3.6^{+0.05}_{-0.07}$ Ga (Figures AII-5a and AII-5c). To further support the derived ages, we have also measured the diameters of 575 deformed craters by wrinkle ridges, lobate scarps, and small-scale graben, whose diameters range from ~20 m to ~2.6 km. These small-size craters (diameter ~30 m to ~500 m) are considered Eratosthenian and Copernican in age (Trask, 1971; Moore et al., 1980; Watters et al., 2010). Therefore, based on derived ages and deformed small craters, this study suggests late Eratosthenian to Copernican-age tectonic activity in the study area.

4.4 Discussion

4.4.1 Small-scale graben formation and Blind thrust fault

The deformed structures mapped in this study are mainly distributed in the western region of the Posidonius crater (Figure 4.2). Among the mapped structures, compressional structures such as wrinkle ridges and lobate scarps are mostly distributed around the Posidonius crater, whereas extensional structures such as small-scale graben and tectonic pits are mostly distributed inside the crater (Figure 4.2a). According to previous studies, these extensional structures—graben are formed as a result of flexural bending during lobate scarp and wrinkle ridge formation (Plescia and Golombek, 1986; Watters et al., 2012; Clark et al., 2022; Frueh et al., 2022). They are oriented perpendicular and subparallel to the strike of the lobate scarp and wrinkle ridge (Watters et al., 2010, 2012). These small-scale graben can contain tectonic pits caused by collapse and drainage into subsurface fault zones (Head and Wilson, 2017). Small-scale graben can also form by flexural bending during shallow magmatic intrusion (Watters et al., 2012). Cooling and degassing of magmatic intrusion to the surface can cause pit craters along and within the graben (Wilson and Head, 2018).

French et al. (2015) did not observe any compressional structures near small-scale graben within the Posidonius crater, thus suggesting that graben were formed as a result of flexural bending due to magma intrusion uplift. In this study, we observed a few compressional structures—wrinkle ridges near the small-scale graben (Figure 4.7), indicating small-scale graben are formed in response to compressional stress. However, a few of these graben on the Posidonius crater floor are directly not observed near compressional

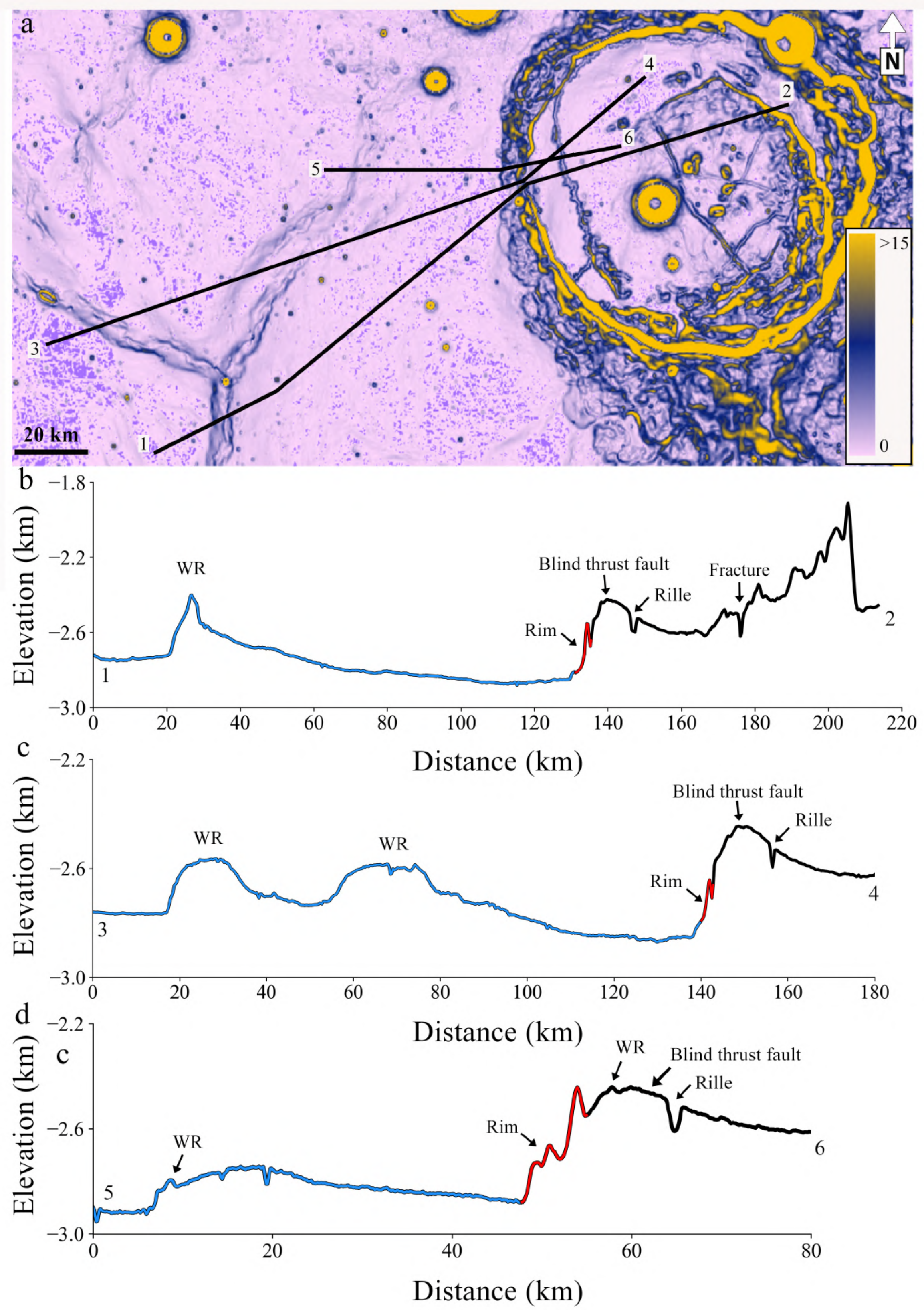

Figure 4.10: a) SLDEM2015 slope map of the study area. b, c, and d) Profile across the wrinkle ridge formed on the Mare Serenitatis basin floor close to the study area and the Posidonius crater's western floor.

structures, but they are located at the elevated portion of the western floor of the Posidonius crater (Figures 4.2a, 4.12c and AII-6). Previous work (French et al., 2015), and our observation of wrinkle ridges near the small-scale graben in the Posidonius crater floor do not offer enough proof to determine how the small-scale graben developed. Therefore, in order to obtain a more precise idea, we further investigated the adjoining wrinkle ridge outside the Posidonius crater, located to the west (N—S orientation), formed at the floor of the Mare Serenitatis basin close to the Posidonius crater (Figure 4.10).

We report an intriguing similarity between the western floor rise inside the Posidonius, where small-scale graben are present, and the topographic rise and fall, as well as the height and width, of the wrinkle ridges located within the basin (Figures 4.10 a-c), which suggests small-scale graben are indeed formed in response to compressional stress associated with wrinkle ridges. Furthermore, to the southwest of the Posidonius crater, Nypaver and Thomson (2022) mapped a cluster of wrinkle ridges and suggested the wrinkle ridges to be recently active. So, based on 1) the existing studies (Thompson et al., 2017; Nypaver and Thomson, 2022), 2) our observations of wrinkle ridges on the Posidonius crater floor (Figures 4.4a and 4.7), and 3) similar topographic rise of wrinkle ridges from the Mare Serenitatis basin floor and the western Posidonius crater floor (Figure 4.10), we expect the thrust fault associated with the active wrinkle ridges reported in Nypaver and Thomson (2022) study in the eastern region of the Mare Serenitatis basin to extend further north, passing through the western Posidonius crater floor in our study area. However, wrinkle ridges are visible only in a few locations within the crater floor (Figures 4.4a and 4.7). In other locations, wrinkle ridges are not visible, but other recent surface expressions (small-scale graben, tectonic pits, and deformed craters) formed in response to it are observed. Adding to our study, in the Andrews-Hanna et al. (2014) study, a linear gravity anomaly associated with lava-filled rifts pass through the western floor of the Posidonius crater, and wrinkle ridges are expected to form in response to compressional stress that closes the lava-filled rifts. Therefore, based on observation and existing studies (Andrews-Hanna et al., 2014; Nypaver and Thomson, 2022), this study suggests that the study area— the western region of the Posidonius crater is deformed by a blind thrust fault.

We propose small-scale graben mapped on the western elevated floor of the Posidonius crater formed due to a blind thrust fault instead of the magma intrusion uplift. Also, associated pits form by collapse and drainage into subsurface fault zones instead of cooling and degassing of magmatic intrusion. These small-scale graben crosscut small-size craters (Figures 4.6 b&d), indicating these graben are young and formed due to the reactivation of blind thrust faults.

4.4.2 Orthogonal transitions of adjacent Wrinkle ridges and Lobate scarps

In the study area, wrinkle ridges are distributed on the Posidonius crater floor and Mare Serenitatis basin floor (Figure 4.2a). Lobate scarps are distributed along the wall and rim of the Posidonius crater (Figure 4.2a). Both the wrinkle ridges and lobate scarps are differentiated based on their morphology and formations in previous studies (Melosh, 1978; Solomon and Head, 1980; Plescia and Golombek, 1986; Schultz, 2000; Banks et al., 2012; Watters et al., 2015; Clark et al., 2017; Williams et al., 2019; Valantinas and Schultz, 2020; Nypaver and Thomson, 2022). This study also observed the morphological difference between the wrinkle ridges and lobate scarps; wrinkle ridges usually appear more sinuous than the arcuate lobate scarps (Figure 4.4 vs 4.5).

According to the prior work, wrinkle ridges and lobate scarps transition into one another (longitudinal transitions) (Clark et al., 2017). Their study suggested a pre-existing blind thrust fault that forms a wrinkle ridge, reactivates, and extends into a highland to form lobate scarps. Around the Posidonius crater, our investigation has revealed several longitudinal transitions of wrinkle ridge to lobate scarp or vice versa at multiple locations (Figures 4.11a and 4.7b). They are mainly clustered between the northeastern Mare Serenitatis basin floor and the Posidonius crater's western rim rather than within the Posidonius crater. This study expects the same formation scenario for longitudinal transition in the area, as suggested by Clark et al. (2017).

In addition to the above-discussed longitudinal transition, we are reporting a new transition of wrinkle ridges and lobate scarps (Figures 4.11a-c). Based on their close proximity and subparallel orientations, we interpret the adjacent wrinkle ridges and lobate scarps to be surface expressions of subsurface splay faults (Watters et al., 2010; Williams et al., 2013; Watters, 2022) of the existing blind fault that formed a larger wrinkle ridge in the area (Figures 4.11d-g). Orthogonal transition terminology was employed in this study to describe closed-by and subparallel-oriented wrinkle ridges and lobate scarps. We have also observed the transition of wrinkles to wrinkles and lobates to lobates, similar to the orthogonal transition of wrinkle ridges and lobate scarps (Figure AII-7). Therefore, this study expects wrinkle-to-wrinkle and lobate-to-lobate orthogonal transitions to also be splay faults. In this study, we have given a visually interpreted splay model (Figures 4.11d-g) of only two splay scenarios for the orthogonal transition of wrinkle ridges and lobate scarps to avoid the complexity. However, this study observed more than two splay scenarios (e.g., Figure AII-7) indicating multiple blind thrusts formed from the main thrust fault, and we expect they can form at the same or different periods from one another. These splay faults (wrinkle ridges and lobate scarps) can form in the same direction as the main thrust fault (synthetic) or in the opposite direction (antithetic) (Figures 4.11d-g).

Based on derived young tectonic activity ages from wrinkle ridges and lobate scarps (Figure AII-4) and deformed small-diameter craters by wrinkle ridges and lobate scarps (Figures 4.3b&d), this study suggests these splay faults—wrinkle ridges and lobate scarps are relatively younger than the main thrust fault. They are likely reactivated or formed newly during the late stage of the reactivation of the existing main thrust fault. This study observed a similarity between the orientations of wrinkle ridges and lobate scarps (N—NW) in the study area (Figures 4.3a&c) and the orientations of the predicted faults due to a combination of recession stresses, diurnal tidal stresses at apogee, and global contraction (Watters et al. (2015), Figure 2c). Overall, we interpret that the formation of splay faults is due to reactivation caused by those three combined stresses.

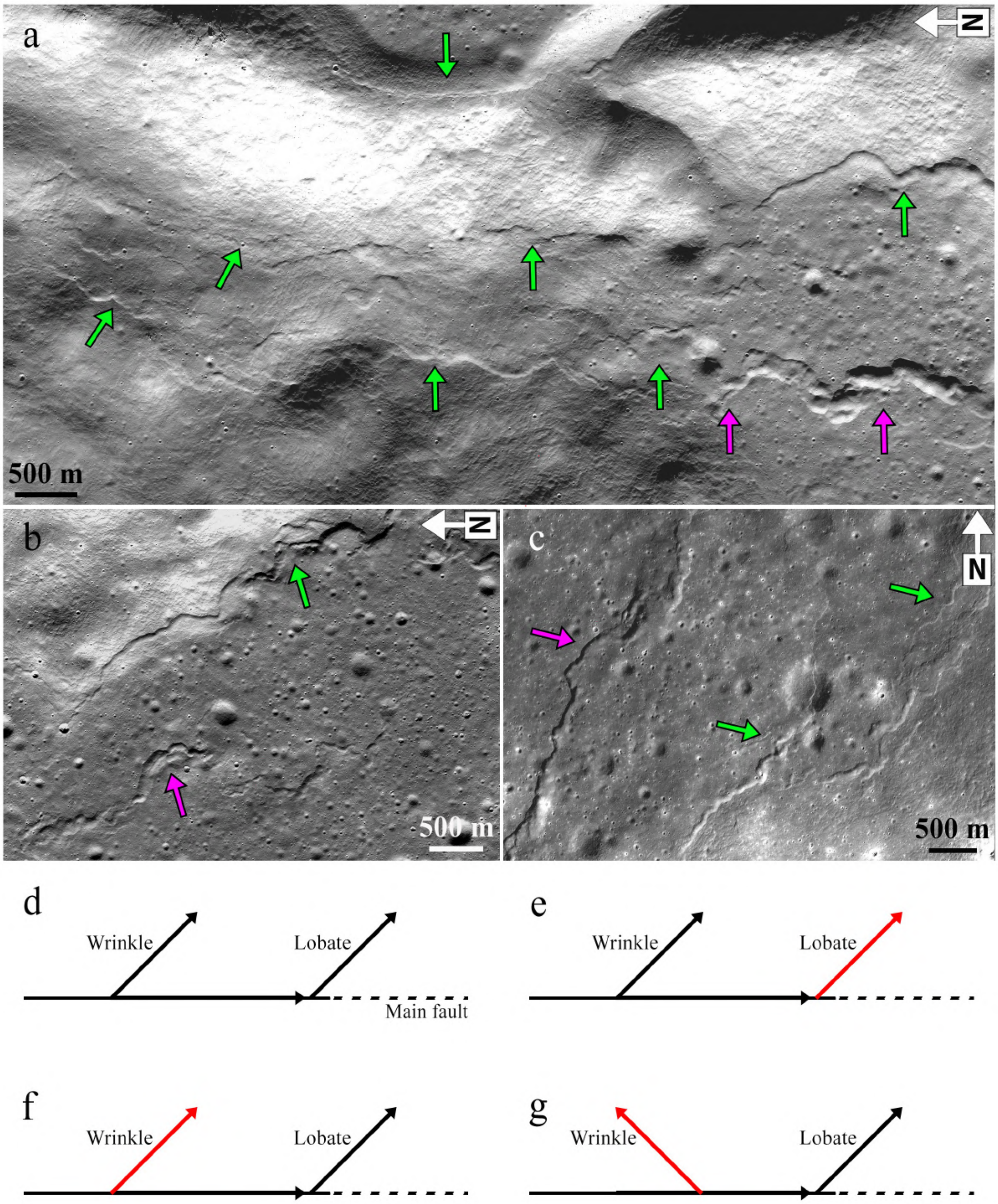

Figure 4.11: LROC-NAC images of wrinkle ridges (pink arrow) and lobate scarps (neon green arrow) transition a) Longitudinal and orthogonal transition of wrinkle ridges and lobate scarps (M1157563796RE). b) M180988010RE and c) M190416512LE, showing an orthogonal transition of adjacent wrinkle ridges and lobate scarps. A visual interpretation of the subsurface splay of wrinkle ridges and lobate scarps orthogonal transition (modified after Feng et al., 2015): d) they can form simultaneously, e) lobate formed after wrinkle, f) wrinkle formed after lobate, and g) antithetic wrinkle formed after lobate.

4.4.3 Formation of the Rimae Posidonius

Rimae Posidonius is a sinuous rille that runs north-south over the western floor and shares its border with the northern Posidonius walls (Figure 4.12a, yellow polygon). Its origin is suggested to be due to lava flow and erosion (Hurwitz et al., 2013). The rimae on the Moon are generally interpreted to be lava channels (Hulme, 1973; Williams et al., 2000; Hurwitz et al., 2012, 2013). The following section discusses a few interesting observations related to the Rimae Posidonius:

1. The northern floor of the Posidonius has the lowest elevation (Figures 4.13a and AII-6). It can be due to the magma intrusion uplifting the surrounding floor, making the northern floor appear relatively lower, or due to subsidence of the northern crater floor towards the center of the crater (Schultz, 1976; Wilson and Head, 2018). The morphology of the Rimae Posidonius seems to be affected by the intrusion and subsidence processes.

2. The Rimae Posidonius formed across the inclined floor ($\sim 1^{\circ}$) (Figures 4.12a—c and 4.13a) with varying widths and depths. Its sinuosity appears to be more than the other rilles (Hurwitz et al., 2013). It also contains mounds—the small, elevated, rounded shape feature within the floor (Figure AII-8). Rimae Posidonius formation on an inclined surface and mounds on the floor raises a question about the rille formation through lava flow erosion in the Posidonius crater.

3. Rimae Posidonius superposed the resurfaced crater floor with lava (Kimi et al., 2023), suggesting it to be younger than the lava infilling (Figure 4.12a).

4. A few sections of Rimae Posidonius share a common boundary with the northern crater wall (Figure 4.12a, black arrows). In the western region, it plausibly followed or joined the existing moat (Figures 4.12a&d, blue arrow). The moat separates the wall from the crater floor (Schultz, 1976; Jozwiak et al., 2012), and its formation is hypothesized to be related to dike intrusion and sill formation (Jozwiak et al., 2012). It also shares borders with three hillocks, which might be relics of an earlier floor material (Figure 4.13b, blue arrows).

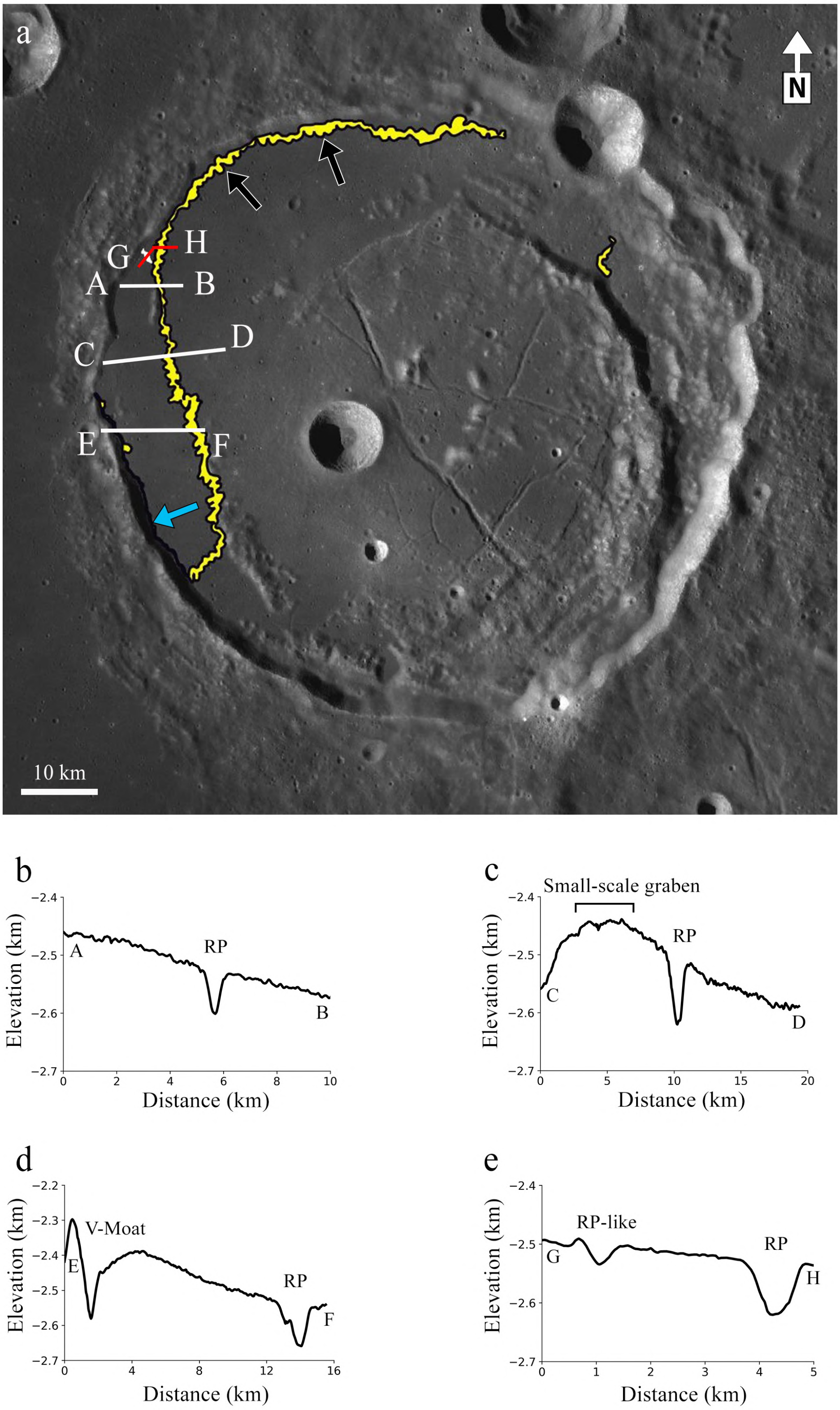

Figure 4.12: a) Rimae Posidonius (yellow) and Rimae Posidonius-like rille (white) overlaid on the LROC-WAC mosaic. b) and c) are profiles of Rimae Posidonius (RP) on a western sloping floor from west to east. d) Profile of V-Moat and Rimae Posidonius. e) Profile of Rimae Posidonius-like rille and Rimae Posidonius.

5. A long, narrow linear gravity anomaly passes through the western region of the Posidonius crater (Andrews-Hanna et al., 2014), which coincides with the Rimae Posidonius location. These linear gravity anomalies are interpreted to be the frozen remnants of lava-filled rifts (Andrews-Hanna et al., 2014).

Based on our observations and the existing studies (Schultz, 1976; Jozwiak et al., 2012; Andrews-Hanna et al., 2014; Kimi et al., 2023), this study expects a combination of complex modification processes—a moat—forming intrusion (Jozwiak et al., 2012), subsidence of the crater floor (Schultz, 1976; Wilson and Head, 2018) towards the center, and lava-filled rifts tectonics associated with blind thrust fault (Andrews-Hanna et al., 2014) played a role in the formation of the Rimae Posidonius. In addition, we observed a Rimae Posidonius-like feature, smaller and shallower than Rimae Posidonius, on the northwestern floor (Figures 4.12a&e and 4.14). It can be an underdeveloped rille that formed after Rimae Posidonius when the intensity of modification processes decreased. There is no sign of lava flowing within the small Rimae Posidonius-like feature, which supports our hypothesis that this rille may be the result of complex modification processes, but still, we are not ruling out the possibility of lava forming the rille.

4.4.4 Tectonic evolution of the Posidonius crater region

Based on this study, we constructed a schematic model illustrating the tectonic evolution of the Posidonius crater region (Figure 4.15) as described below:

Nectarian period: The Posidonius crater formed in the northeastern region of the Mare Serenitatis basin, indicating its formation younger than the Mare Serenitatis basin (~3.98 Ga, Neukum (1984)). We expect that after the formation, the Posidonius crater experienced extensive and intense volcanism that partially buried the central peak (Kimi et al., 2023) (Figure 4.15a).

Imbrian period: The Posidonius crater has a fractured floor due to shallow magmatic intrusion (Jozwiak et al., 2012). This study's determined age of the fracture floor is ~3.6 Ga (Figure AII-5c), close to the earlier reported age (~3.7 Ga, Salem et al. (2022). We expect the shallow magmatic intrusion followed volcanism, which led to a huge slumping at the eastern wall of the Posidonius crater (Figure 4.15b & 4.13b).

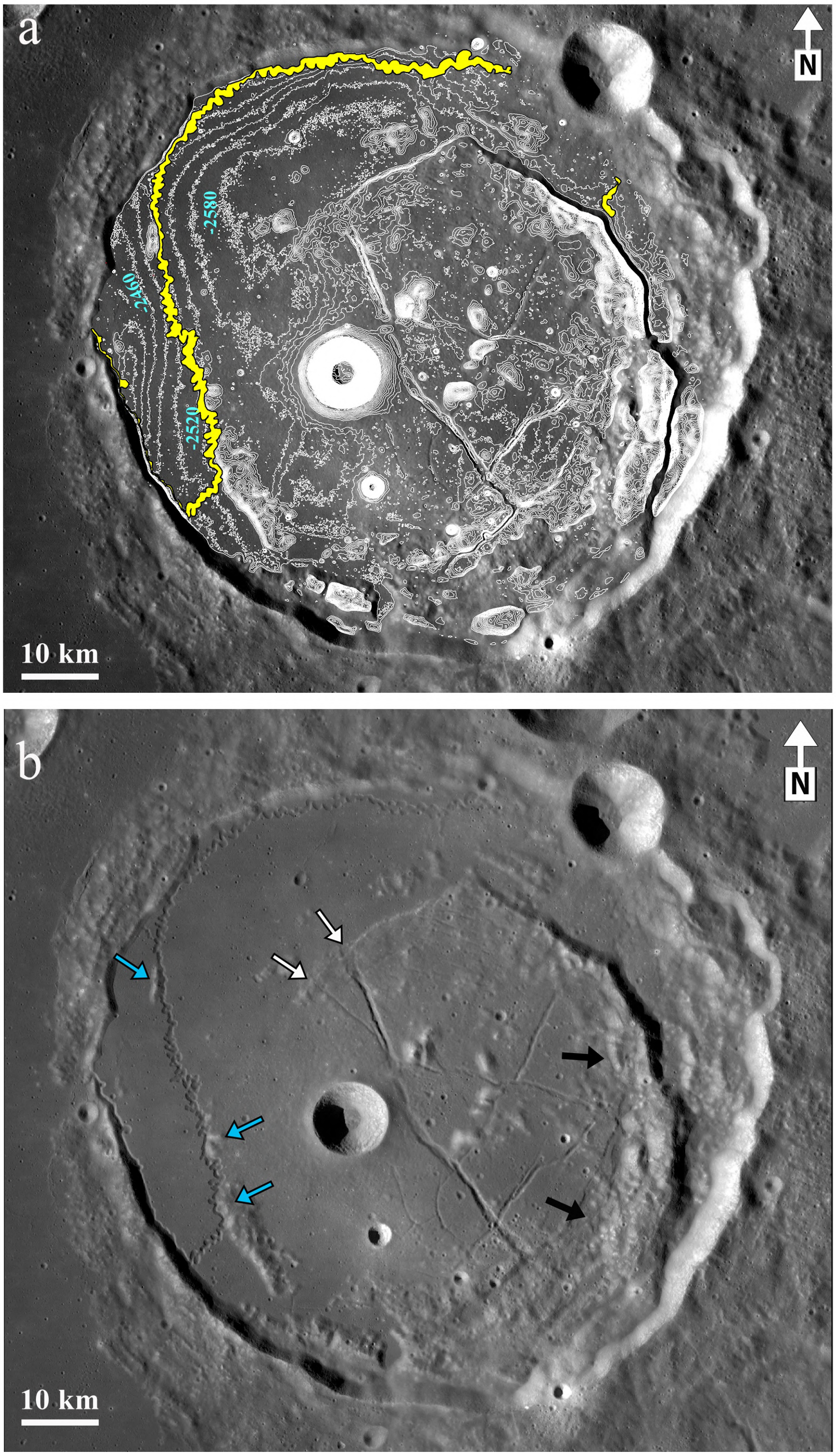

Figure 4.13: a) Rimae Posidonius (yellow), along with the contour map of 30 m intervals, is shown in the LROC-WAC mosaic. Rimae Posidonius is observed following two parallel consecutive contour intervals. b) Slumped wall (black arrows), truncated fractures (white arrows), and hillocks that might be relics of an earlier floor material (blue arrows).

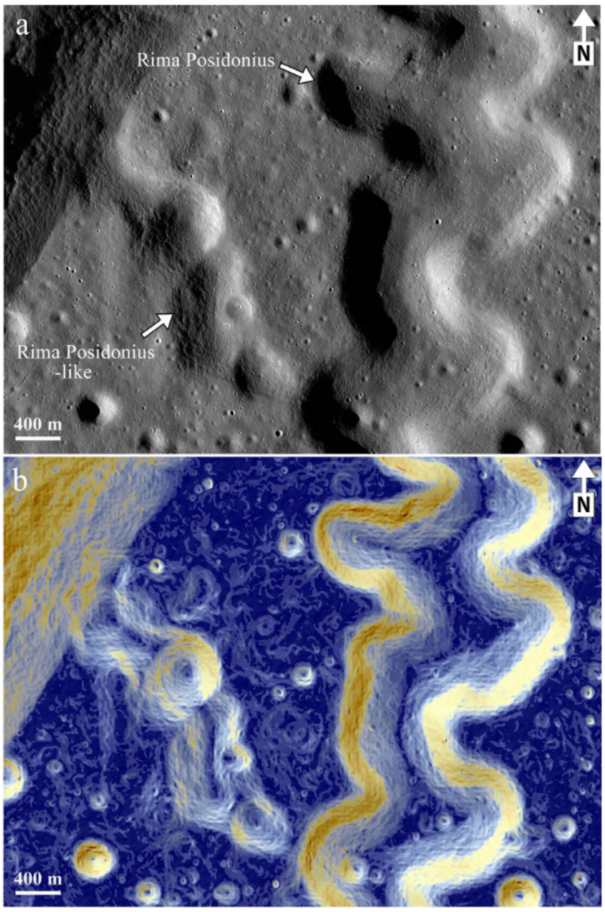

Figure 4.14: Rimae Posidonius and Rimae Posidonius-like rille, smaller and shallower than Rimae Posidonius, shown in a) LROC-NAC image (M1188164347LE) and b) a slope map—light colours indicate steeper slopes and dark colours shallower slopes.

Imbrian to Copernican period: During this period, based on the truncated/discontinuous fractures and the determined age of the lava-covered floor (∼3.1 Ga, Figure AII-5b), we interpret a second phase of volcanism to occur after the shallow magmatic intrusion, which erased/truncated the fractures (Figure 4.13b). The fault plausibly formed during the Mare Serenitatis basin formation (Hartmann and Kuiper, 1962; Andrews-Hanna et al., 2018) or due to load-induced subsidence (Melosh, 1978; Solomon and Head, 1980), potentially served as a pathway for the multiple stages of volcanism and intrusive magmatism (Kimi et al., 2023).

Within this period, along with volcanism, we expect multiple complex processes—subsidence (Schultz, 1976; Wilson and Head, 2018), the transition from vertical (magmatic uplift, subsidence) to horizontal tectonism (wrinkle ridges) (Solomon and Head, 1979), and the formation of Rimae Posidonius (Figure 4.15c).

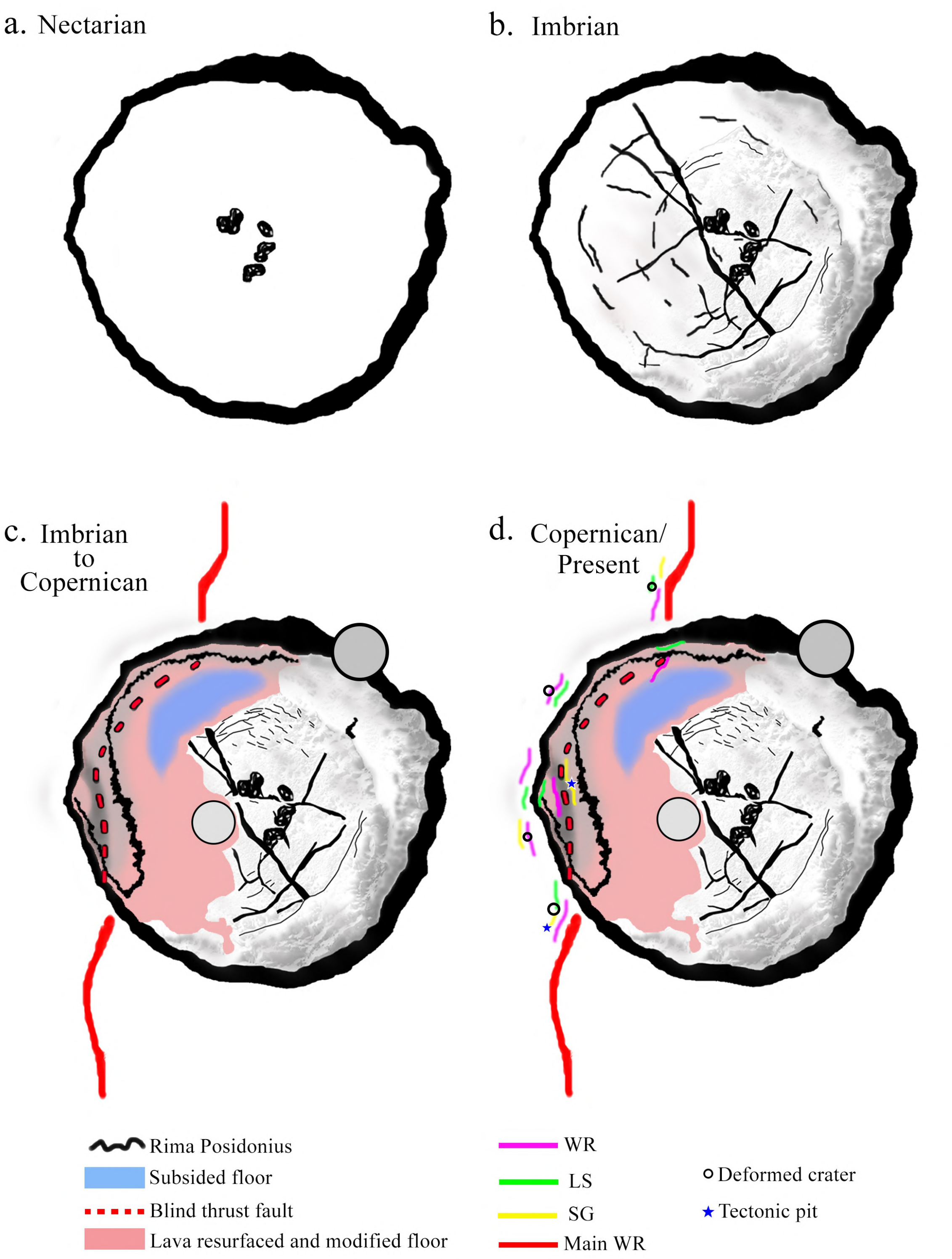

Figure 4.15: A schematic diagram illustrating the expected tectonic evolution of the Posidonius crater region from the Nectarian to Copernican periods. a) Lava filled the Posidonius crater floor and partially buried the central peak. b) Magma intrusion resulted in fracturing the crater floor and slumping of the eastern wall. c) Lava resurfaced the crater floor, partially erasing the fractures, followed by subsidence, formation of wrinkle ridges and Rimae Posidonius. d) At present, deformational structures—wrinkle ridges, lobate scarps, small-scale graben, tectonic pits, and deformed craters—possibly continue deformation. (The Figure is not to scale.)

Copernican period: Based on the recent deformational structures—wrinkle ridges, lobate scarps, small-scale graben, tectonic pits, and deformed craters —as well as the ages of the wrinkle ridges and lobate scarps (Figure AII-4), we expected the existing blind thrust fault passing through the western region of the Posidonius crater reactivated in the Copernican period and formed the recent deformation structures, or deformation continued and could still be tectonically active (Figure 4.15d).

4.5 Conclusions

The study of the Posidonius crater and its surrounding tectonic structures reveals the following:

1. The study area is deformed by deep-seated fractures beneath the western floor of the Posidonius crater. These fractures likely originated from basin fractures (Hartmann and Kuiper, 1962; Andrews-Hanna et al., 2018) or may have formed during load-induced subsidence (Melosh, 1978; Solomon and Head, 1980).

2. These fractures potentially served as a pathway for the multiple stages of volcanism and intrusive magmatism, dating back up to ~2.8 Ga and leading to slumping on the crater's eastern wall.

3. Tectonic features such as wrinkle ridges, lobate scarps, and deformed small-size craters, which are indicators of recent activity on the Moon analyzed in the study area, suggest ages ranging from $\sim 29^{+10}_{-9}$ Ma to $\sim 1.9 \pm 0.7$ Ga. This suggests the deep-seated fracture was plausibly reactivated, forming these tectonic features during the Eratosthenian period and continuing into the Copernican period.

4. This reactivation is possibly caused by stresses from a combination of lunar recession forces, diurnal tidal stresses at apogee, and global contraction.

5. The reactivation of the fracture led to the formation of splay faults, as evidenced by nearby and subparallel-oriented wrinkle ridges and lobate scarps, referred to as orthogonal transitions. These transitions also suggest multiple reactivation events in the study area.

6. Additionally, this study suggests that the small-scale graben observed on the elevated western floor of the Posidonius crater were formed by

flexural bending resulting from the reactivation of this fault rather than the previously proposed magma intrusion uplift.

7. A combination of complex modification processes—a moat-forming intrusion (Jozwiak et al., 2012), subsidence of the crater floor (Schultz, 1976; Wilson and Head, 2018), and lava-filled rifts tectonics associated with blind thrust fault (Andrews-Hanna et al., 2014)—could have formed the Rimae Posidonius. A small rille on the northwest floor resembling the Rimae Posidonius may be an undeveloped rille with no sign of lava flowing, supporting our hypothesis that this rille may result from complex modification processes.

Chapter 5

Gruithuisen Region Lava Tube:

Insights from Magmatism & Tectonism Interaction

5.1 Introduction

Lunar lava tubes have gained considerable attention due to their potential as habitable spaces for future missions. These naturally occurring tunnels formed by lava flow (Please refer to Section 1.2) provide a shield against extreme temperature variations, radiation, and micrometeorite impacts, making them attractive candidates for potential human bases (Coombs and Hawke, 1992; Haruyama et al., 2012; Blamont, 2014).

Obtaining direct information about lava tubes is challenging due to their subsurface nature. However, earlier studies have adopted a photo-geological approach to investigate the potential presence of these underground structures. They utilize photo-geological analyses of collapsed pits and pit chains as a means to infer the existence of subsurface lava tubes (Haruyama et al., 2009; Robinson et al., 2012; Wagner and Robinson, 2014; Sauro et al., 2020). With advancements in technology, researchers have now delved into the exploration of subsurface lunar lava tubes by harnessing data acquired from missions such as the Gravity Recovery and Interior Laboratory (GRAIL) (Chappaz et al., 2017; Zhu et al., 2024) and the SELENE Lunar Radar Sounder (LRS) (Kaku et al., 2017). The identification of potential lava tubes with GRAIL relies on the observation of mass deficits, while the LRS is centred on detecting characteristics in radar echos (Chappaz et al., 2017; Kaku et al., 2017; Zhu et al., 2024).

Additionally, studies have employed numerical models to assess the structural stability of lava tubes, with key factors under consideration, including

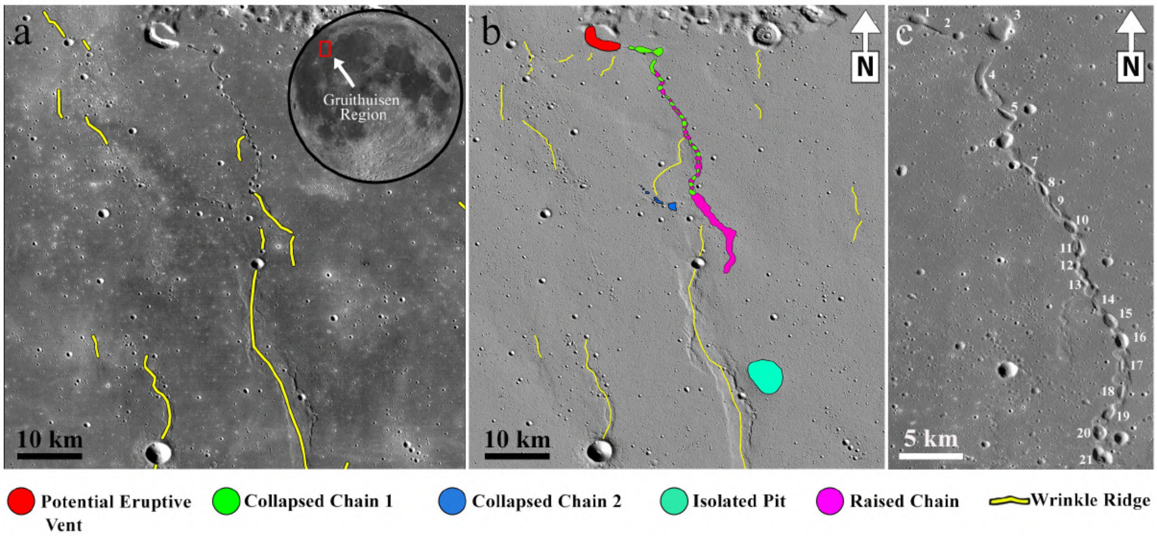

Figure 5.1: a) The study area located at the Gruithuisen region (∼35°N, 44°W) is shown in LROC-NAC images overlaid by wrinkle ridges mapped by Thompson et al. (2017). b) Geomorphological map containing collapsed pits, raised features, potential eruptive vent and wrinkle ridges. c) Closer view of collapsed pits and raised features in LROC-NAC images.

the lava tube's dimensions, the thickness of the overlying material, and material properties, the tensile strength of the materials (Theinat et al., 2020). Moreover, Martellato et al. (2013) conducted a modelling of the formation of pits that occur when a meteorite impacts the roof of a lava tube, leading to its collapse. Adding on to the Martellato et al. (2013) meteorite impacts scenarios, Sauro et al. (2020) photo-geological study suggested the possibility of pit chain formation due to compressional tectonic activity based on wrinkle ridge partially following the collapsed chain. This compressional tectonism can arise from various processes: load-induced subsidence (Solomon and Head, 1980), global cooling contraction (Watters et al., 2010), and a combination of global contraction, orbital recession, and tidal forces (Watters et al., 2015). Wrinkle ridges are linear deformational structures formed due to compressional stress (Solomon and Head, 1980; Watters et al., 2010; Valantinas and Schultz, 2020; Nypaver and Thomson, 2022).

In this context, our objective is to comprehend how a lava tube responds to compressional stress, drawing from insights provided in the Sauro et al. (2020) study, which suggested the possibility of collapsed pit chain formation linked to a lava tube as a result of compressional stress in the Gruithuisen region. We expect that the Gruithuisen region is an ideal location for investigating lava tube deformation (Figure 5.1a). We have integrated numerical simulations alongside morphometric analysis to understand the lava tube deformation, with a focus on addressing existing knowledge gaps related to how the interaction between compressional tectonic activity and volcanic feature–lava tube plays a role in shaping the surface of the Moon.

5.2 Methodology

5.2.1 Datasets, Mapping, and Measurements

In this study, georeferenced Lunar Reconnaissance Orbiter Camera (LROC)–Narrow-Angle Camera (NAC) images with resolutions ~1 to 1.5 m/pixel (Table AIII-1) were utilised for detailed mapping. The NAC DTM with vertical and horizontal precision finer than ~2 to 5 m/pixel (Henriksen et al., 2017) and SLDEM2015 with a spatial resolution of ~59 m/pixel and a vertical resolution of ~3–4 m (Barker et al., 2016) were used for topography analysis. Using these datasets in ArcGIS, the wrinkle ridges, collapsed pits, and associated raised features were mapped. Additionally, this study incorporated shapefiles of previously identified wrinkle ridges for cross-referencing and validation (Thompson et al., 2017). This study used an orthographic projection in the mapping process. Subsequently, the length of the wrinkle ridges and the major and minor axes of the collapsed pits, the depth of the collapsed pits, the height of raised features, and the orientations of the wrinkle ridges were measured. Collapsed pit depths were estimated by computing the difference between contour values (5 m interval) of collapsed edges and floors. Similarly, the heights of raised features were determined from the difference in contour values (5 m interval) between the highest contour of the raised feature and the surrounding floor.

5.2.2 Estimation of Strain, Stress, and Force

In this study, the normal strain was estimated using the largest wrinkle ridge present in the study area (Figure 5.2). This study employed the same method previously utilised by Watters and Robinson (1997) and Watters (2022). The strain is the result of how the geological structure responds to external forces. The formula for calculating normal strain, ϵ, involves:

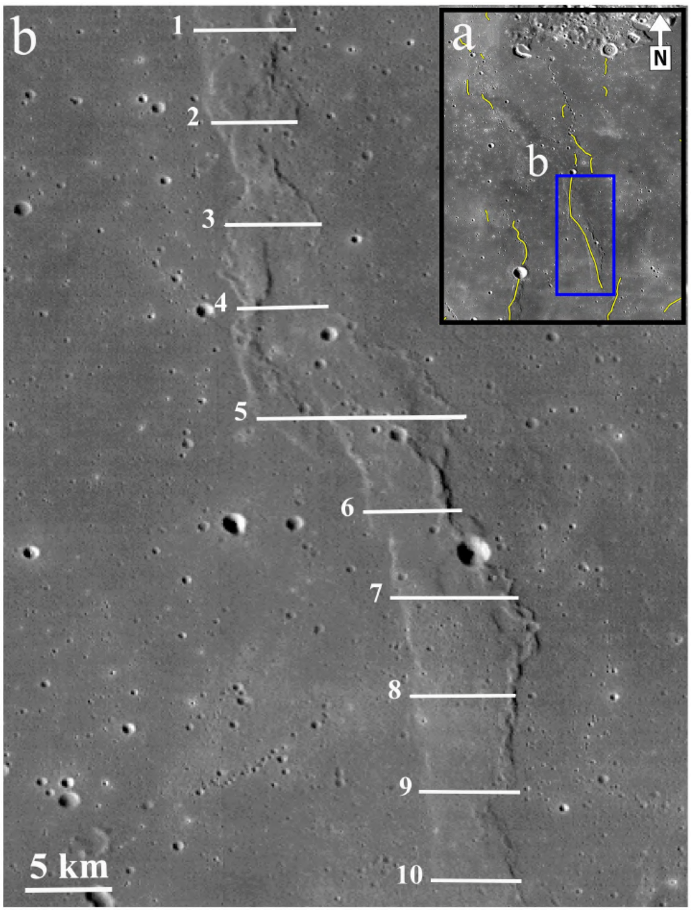

Figure 5.2: Measured ten cross-sections across the large wrinkle ridge in the study area.

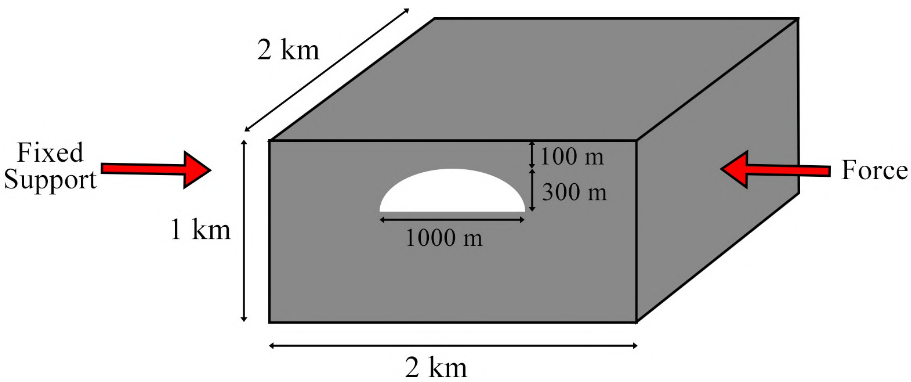

Figure 5.3: The dimensions of 2 km x 2 km x 1 km were employed in the 3D model, and a semi-elliptical hollow section of a 1 km width, approx. one-third height and a 100 m thick roof were used. Note that dimensions are not for scale. The red arrow indicates the direction of the applied fixed support/boundary condition and the force applied in the opposite direction.

$$\epsilon = \frac{\Delta L}{L_o} \tag{5.1}$$

where ΔL is the change in length, and L_o is the original length.

A systematic approach was taken for obtaining ΔL and L_o: Ten horizontal straight-line distances across the large wrinkle ridge were measured for comprehensive sampling. Then, the cross-length sections were calculated across these ten sections of the wrinkle ridge using the Pythagorean theorem (Figure 5.2). Then, the difference between the cross-length and the horizontal straight-line distance was estimated, representing the length change (ΔL). The horizontal straight-line distance represented the original length (L_o). By using these two measured parameters, normal strain (ϵ) was calculated. Then, normal stress (σ) was calculated:

$$\sigma = E \times \epsilon \tag{5.2}$$

where E is Elastic Modulus.

The force (F) was then calculated by:

$$F = \sigma \times A \tag{5.3}$$

where A is the area of the geometry of the model.

5.2.3 3D Modelling in Ansys

ANSYS 2019 software was used for qualitative 3D modelling to study lava tube deformation via Finite Element Analysis (FEA). We defined material properties based on established sources, with the model sensitive to Young's modulus and Poisson's ratio (Theinat et al., 2020) (Table AIII-2). The model had dimensions of 2 km in length, 2 km in width, and 1 km in height with a semi-elliptical hollow section. The semi-elliptical hollow dimensions and roof thickness followed Theinat et al. (2020), suggesting a 1km width, approx. one-third of its width in height, and a 100 m roof stability thickness (Figure 5.3). This geometry was meshed with 50 m divisions, ensuring that both the geometries and the mesh were optimized for faster computer simulations without compromising result precision. Our model simplifies complex scenarios for better understanding. It is important to note that the 3D simulation results in this study primarily emphasize the structural changes when subjected to force rather than providing precise quantification. The quantification is challenging since accurately simulating the actual conditions is not feasible. Therefore, this model focuses on visualizing and understanding the shapes (geometries) of the tubes that emerge under the compressional force. The specific boundary conditions were set based on the observations of the orientations of the wrinkle ridges and estimated stress from the largest wrinkle ridge in the study area. It guided us in inferring the direction and estimating the amount of external force that should be applied in linear static structural analysis. An external force was applied in the negative x-direction (East to West), counterbalanced by fixed supports at the opposing end (West) (Figure 5.3). In modelling, we initially assumed the lava tube had remained unaffected by any external forces since its formation. Then, the external force was introduced to the empty lava tube in the negative x-direction.

The governing equation was solved by Ansys software once boundary conditions were established in linear static analysis:

$$F = [K] \times u \tag{5.4}$$

where F is the applied force, [K] is the stiffness matrix, and u is the displacement.

Subsequently, after completing the static structural analysis, an eigenbuckling analysis was performed to determine the load at which the structure is expected to undergo buckling. This calculation was carried out in the Ansys software using the following equation:

$$[K + \lambda_n[S]]\Psi_n = 0 \tag{5.5}$$

where [K] is the stiffness matrix, and [S] is the stress stiffness matrix.

The outcome of this analysis is the load multiplier (λ_n) and the mode shape (Ψ_n). We validated simulation results/ mode shape (Ψ_n) by comparing with mapped collapsed chain and raised features in the Gruithuisen region.

5.3 Results

5.3.1 Collapsed pits and Raised features

A total of 29 collapsed pits and 13 raised features were mapped in the study area (Figure 5.1b). Among these, 21 collapsed pits were part of the collapsed chain 1 and associated with 13 raised features (Figures 5.1b&c). The collapsed chain 2 has seven collapses, but no associated raised features (Figure 5.1b). Furthermore, we discovered one isolated collapsed pit (Figure 5.1c), bringing the total count to 29 mapped collapsed pits in the study area. However, this study primarily focuses on features associated with collapsed chain 1.

The ellipticity of the 29 collapsed pits has aspect ratios ranging from 0.1 to 0.9. Major axes ranged from ~140 m to ~8 km, averaging ~1.5 km, while minor axes spanned ~100 m to ~4 km, averaging ~1 km. Depths obtained using NAC DTM and SLDEM2015 varied widely, from ~5 m to ~225 m, averaging ~80 m (Table AIII-3). Raised features reached ~35 m to ~85 m height, averaging ~50 m (Table AIII-4). The measured data provides insights into the diversity of the collapsed pits in the study region.

5.3.2 Wrinkle Ridges: Orientations, Strain, Stress, and Force

We mapped 16 wrinkle ridge segments, whose cumulative length is ~178 km long, significantly overlapping with Thompson et al. (2017) (Figures 5.1a&b). Our primary goal in mapping these wrinkle ridges was to determine the prevailing stress direction for accurate force modelling. We found that they predominantly trended northward (Figure 5.1b, and Figure AIII-1 and Table AIII-5), indicating the maximum principal stress in the region likely aligns in the east-west direction. In addition to stress orientation, the calculated normal strain from largest wrinkle ridge range from ~$7*10^{-4}$ to $4*10^{-3}$, averaging $2*10^{-3}$, normal stress range from ~$2*10^{-2}$ to $1*10^{-1}$ GPa, averaging ~$7*10^{-2}$ GPa (Table AIII-6), and force, considering the area of $2*1$ km^2 from the geometry of the model, and average stress of ~$7*10^{-2}$ GPa, is ~$1.4*10^{14}$ N.

5.3.3 3D Models

In total, twenty mode shapes/3D deformed models were studied under varying load multipliers during buckling analysis, and variations in both

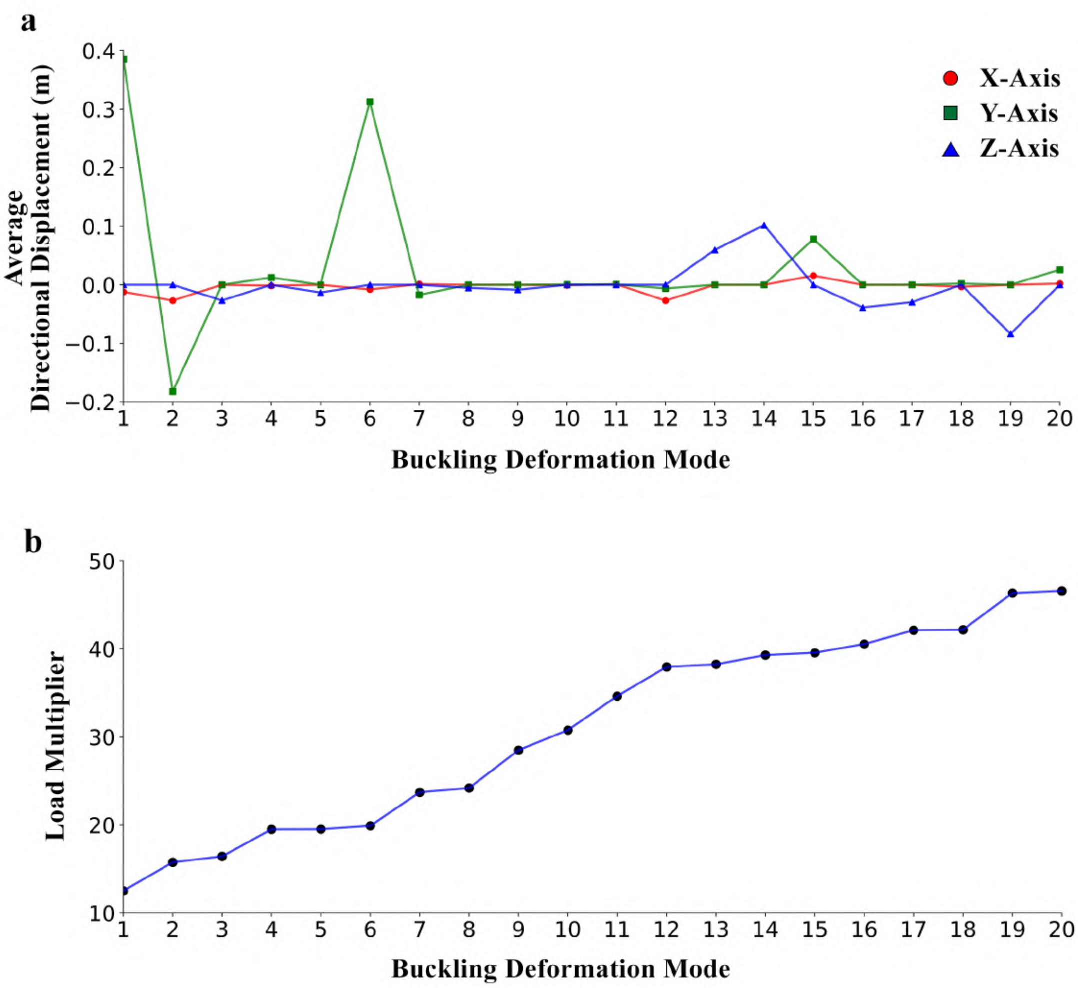

Figure 5.4: a) Displays the average directional displacement versus mode shape for twenty simulated models, illustrating variations in displacement magnitude and direction. Negative displacement signifies movement along the negative X, Y, and Z axes. b) Load multiplier versus mode shape, indicating the amount of load that needs to be multiplied by the estimated force ($1.4*10^{14}$ N) to achieve the depicted mode shape.

displacement magnitude and direction along the XYZ axes were observed with the maximum displacement occurring along the Y axis, followed by the Z and X axes (Figures 5.4 and Table AIII-7).

The observed deformations in the models appear at stresses significantly higher than the estimated 70 MPa value, possibly due to simplification in the model. The simplified model does not account for variations in lava tube roof thickness, cross-sections (Chwała et al., 2024), and tube shapes (Calvari and Pinkerton, 1998), which would influence deformation (Figures AIII-2 and AIII-3).

Among the 20 models studied, several exhibited similarities: Model 2 resembles Model 1 (Gifs S15 & S14); Model 4 resembles Models 3, 8, and 10 (Gifs S17, S16, S21 & S23); Model 7 resembles Models 5, 9, and 11 (Gifs S20, S18, S22 & S24); and Model 18 is similar to Model 19 (Gifs S31 & S32). Among the similar models, the most likely match model was chosen for comparison with the observation (For Gifs please refer to: https://doi.org/10.5281/zenodo.11075944). The models closely resembling the observation are 2, 4, 6, 7, 13, 16, and 18.

5.4 Discussion

The morphology of the collapsed chain 1 and associated raised features closely align with the seven simulated 3D models out of the twenty (Figure AIII-4). The collapsed chain 1 exhibited eight distinct morphological characteristics: 1) Collapsed pit resembling a curvilinear channel-like shape with walls with nearly uniform slopes. Model 2, which closely resembles this, displays consecutive sagging and hogging in the roof of the lava tube, with sagging aligning the observed collapsed pit (Figures 5.5a-c). This study employed sagging and hogging terms to describe the model lava tube roof bending concave upward and downward. 2) Alternating collapsed pits and raised features were identified, characterized by elliptical collapsed shapes and approximately uniform collapsed wall slopes. A total of seven were identified, and the closely resembling model 4 exhibits an alternating pattern of sagging and hogging of the lava tube roof (Figures 5.5d-f and Figure AIII-5). 3) Collapsed pit having a nearly elliptical shape, with one side displaying a steeper slope while the other displaying a gentler slope. The closely resembling model 6 exhibits a partial sagging and hogging of the lava tube roof (Figures 5.5g-i). 4) Partially collapsed pits and raised features were identified with nearly uniform collapsed wall slopes. A total of five are identified, and three have the additional feature of alternating raise patterns (Figures 5.6a&b and Figure AIII-6). The close resembling model 7 shows partial sagging and hogging of the lava tube roof with a distinctive elliptical shape and repetition (Figure 5.6c). 5) Collapsed pits surrounded by raised features and exhibit more or less uniform collapsed wall slopes. A pair of such features have been recognized with an additional feature displaying alternating raised patterns (Figures 5.6d&e and Figure AIII-7). 6) Collapsed pits with a raised feature at the center and have nearly uniform wall slopes. A pair of these features has been recognized

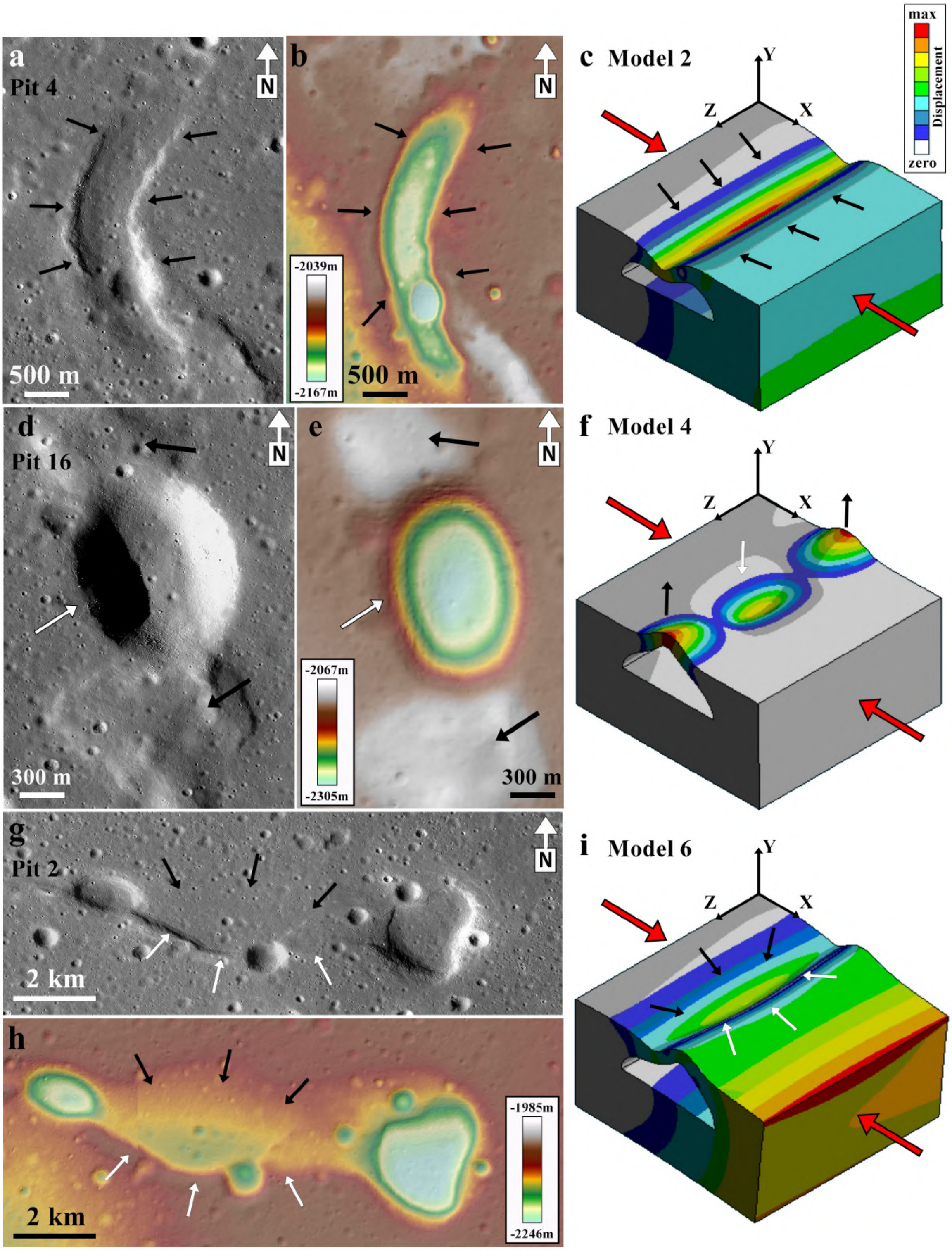

Figure 5.5: Comparison of morphological features in LROC-NAC images and NAC DTM with the model. a&b) Pit 4-curved-shaped is possibly due to the natural formation of the curved lava tube, while c) Model 2 appears straight due to simplifications made to avoid complexity. d&e) Pit 16, alternating pattern of collapsed and raised feature, and aligned f) Model 4. g&h) Pit 2 with a steep slope on one side than the other, and i) Model 6. Red arrows denote force direction.

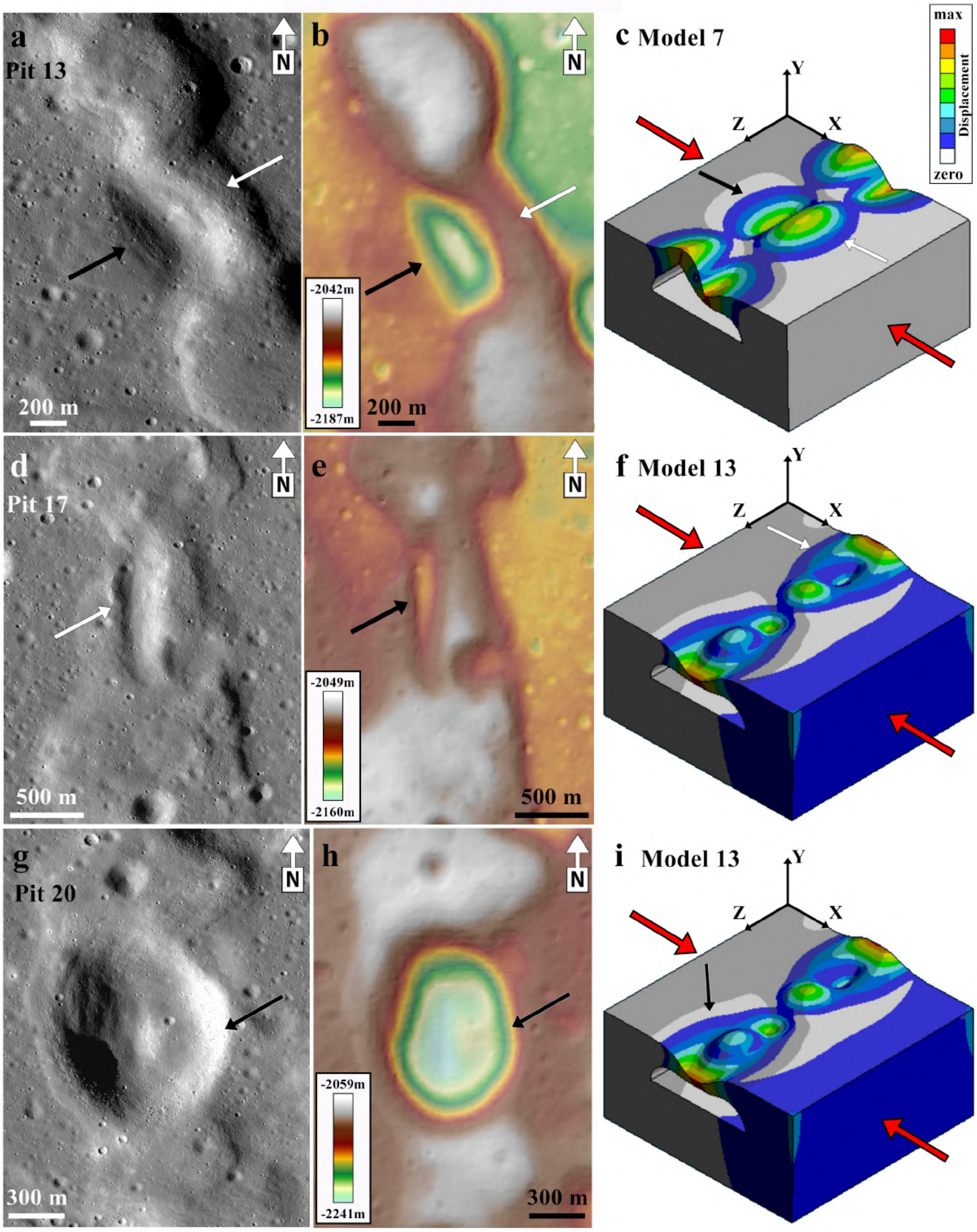

Figure 5.6: Comparison of morphological features in LROC-NAC images and NAC DTM with model. a&b) Pit 13-partial collapsed and raised feature and aligned c) Model 7. d&e) Pit 17 is surrounded by a raised feature, and f) Model 13. g&h) Pit 20 with a raised feature at the center and i) Model 13. Red arrows denote force direction.

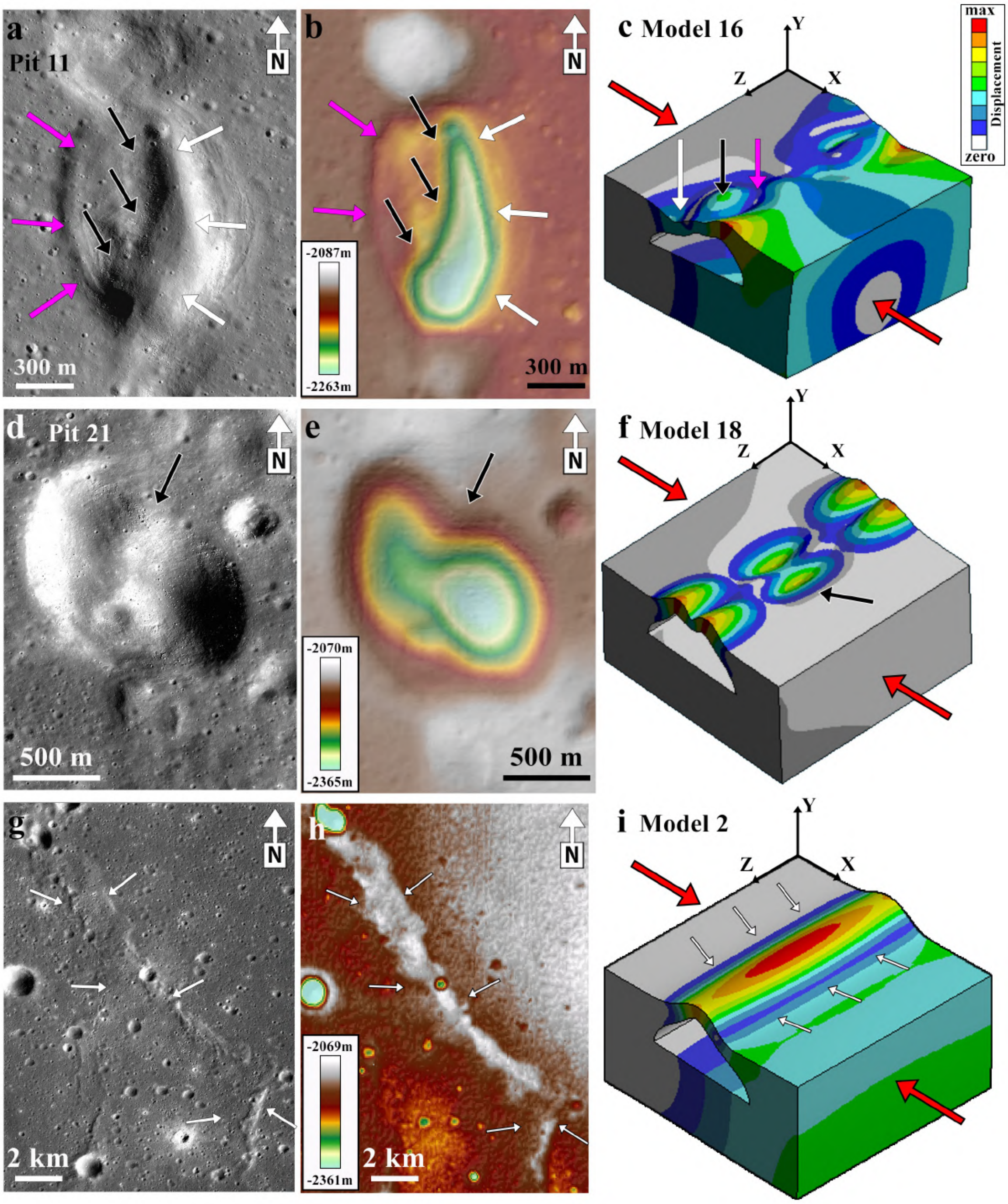

Figure 5.7: Comparison of morphological features in LROC-NAC images and NAC DTM with model. a&b) Pit 11-one side is significantly collapsed than the other, and c) Model 16. d&e) Pit 21 seems fused of a pair of pits, and f) Model 18. g&h) Elongated raised feature at the end of collapsed chain 1 and i) Model 2. Red arrows denote force direction.

with an additional feature displaying alternating raised patterns (Figures 5.6g&h and Figure AIII-8). The closely resembling model 13, with the above-discussed five and sixth characteristic, is observed hogging within the sagging of the lava tube and vice-versa (Figures 5.6f&i). 7) Collapsed pit with non-uniform collapsing where one side of the pit experiences a significant collapse than the other, creating an asymmetrical appearance. A total of two such features were recognized. Furthermore, an additional feature displays alternating raised patterns (Figures 5.7a&b and Figure AIII-9). The closely resembling model 16 shows sagging of one side more pronouncedly than the other and hogging in the middle (Figure 5.7c). 8) Two collapsed pits seem to be fused and have nearly uniform wall slopes, and the resembling model 18 shows a pair of hogging and another pair of sagging alternatingly (Figures 5.7d-f). In addition, an elongated raised feature was observed at the end of the collapsed chain 1, and the model 2 hogging pattern closely resembled (Figures 5.7g-i). Based on modelling, this study propose an elongated structure that could be an intact lava tube.

Pits typically display an elliptical or conical shape, with or without flat floors, and their walls often show clear stratification (Wyrick et al., 2004; Wagner and Robinson, 2014). However, in morphological observations, we did not observe stratification. It could be due to being obscured by regolith covering the stratification, or the lava tube roof did not experience complete failure or collapse, explaining the lack of a stratified wall. Therefore, it appeared to concave up, aligning with our model findings.

The closely aligned seven simulated 3D models, models 2, 4, 6, and 7, have significant displacement along the Y-axis, followed by X and Z directions. These models also differ noticeably from one another in the displacement magnitude and direction (positive or negative). For Model 13, displacement primarily occurs in the Z-axis, followed by X and then the Y-axis direction. Model 16 displays displacement primarily along the Z-axis, followed by Y and X-axis. Model 18 has dominant displacement along the X-axis direction, followed by Y and Z directions (Figure 5.4a). These variations in displacement magnitude and direction result from varying compressional stress that arises from increased load multiplier during the buckling analysis. These varying stresses contribute significantly to the diverse shapes observed among these models (Figure 5.4b and Table AIII-7).

5.5 Conclusions

This study investigated the interactions between compressional tectonic activity and lava tube in the Gruithuisen region, to understand its role in shaping the surface of the Moon through numerical simulations and morphometric analysis. Among twenty simulated models, seven aligned with morphometric analysis results, highlighting unique morphological characteristics arising from disparities in displacement magnitude and direction along three distinct axes (X, Y, Z) due to varying compressional stress in the model and study area. Moreover, the models reveal that a) the collapses observed were partial rather than complete and b) an elongated structure associated with the collapsed chain 1 could be an intact lava tube resembling wrinkle ridges.

Additionally, the estimated compressional stress levels, averaging ~70 MPa, fall within the predicted threshold (~100 MPa) for the formation of blind thrust faults (Solomon and Head, 1979; Watters et al., 2010). However, concluding whether the same or higher stress level contributed to the deformation of the lava tube remains challenging, as our model simplifies many complexities.

Based on this study, we expect the lava tube in the Gruithuisen region to have formed in the past lunar history when global expansion and volcanism prevailed (Solomon and Longhi, 1977). As lunar conditions transitioned to a phase of global cooling, leading to the global contraction of the Moon (Solomon and Longhi, 1977; Head and Wilson, 2017), the Gruithuisen region lava tube was subjected to compressional stress–the combination of recession stresses, diurnal tidal stresses at apogee, and global contraction like wrinkle ridges (Watters et al., 2015), giving rise to unique structural deformation in the area due to sequential geological events of lava tube formation followed by compressional stress resulting in lava tube deformation. Overall, the lava tube in the Gruithuisen region, Moon, is intriguing, characterized by a distinctive chain of collapsed pits and raised features, provides an opportunity to understand the potential morphological deformation of lunar lava tubes under compressional stress.

Chapter 6

Summary and Future Outlook

6.1 Summary

This chapter presents a brief summary of the work undertaken in this thesis. The study focuses on comprehending how impact cratering, magmatism, and tectonism interact to shape the lunar surface, with insights into the subsurface. First, the study scrutinised the interaction between impact cratering and magmatism through a detailed examination of mare-filled craters. Subsequently, it proceeded to investigate the interaction among impact cratering, magmatism, and tectonism through a study of the Posidonius region. Finally, it concluded by exploring the interaction of magmatism and tectonism through an analysis of lava tube compression in the Gruithuisen region. This investigation of interactions reveals an intriguing narrative of the Moon's dynamic history, spanning from its past to its present state, providing a glimpse into the transformative processes that have sculpted it into the lunar landscape we observe today. Overall, this study led to the following significant insights:

6.1.1 Mare-Filled Craters on the Moon

The study of impact craters floors modified by mare infilling with unbreached rims reveals several key insights. The morphological differences in mare-filled craters are attributed to variations in the amount of lava infilling and intrusion. Class 1a mare-filled craters exhibit the thickest mare infilling, followed by classes 1b and 2, while class 3 and some class 4 mare-filled craters show modifications due to both intrusion and mare infilling. These mare-filled craters are predominantly located at the periphery of the lunar mare and mare-filled impact basins, some within the mare/mare-filled impact basins and a few in the highlands. Previous studies suggest that the highland crust favors intrusions rather than volcanism (Wilson and Head, 2017, 2018). However, this study observed mare-filled craters in the highlands. Additionally, the study by (Michaut and Pinel, 2018) favoured infilling in larger craters (D $\geqslant$15 km), this study observed lava infilling in 71 small craters (D $\leqslant$15 km). Based on these observations, this study propose that impact fractures, combined with internal excess pressure and impact-induced surface unloading, have played a significant role in the processes of magma ascent, intrusion, and eruption in mare-filled craters.

Mare-infilling in simple craters could be sourced from the shallowest stalled recent magma reservoirs, as fractures generated during the formation of simple craters should be relatively shorter in depth than those generated by complex craters or impact basins. Such mare-filled small craters can be potential sites for understanding shallow stalled magma reservoirs.

Mare-modified FFCs refer to craters that have undergone modification by mare activity subsequent to their formation as floor-fractured craters. These craters suggest that the same crater witnessed multiple episodes of magmatism. It raises the question of whether completely filled mare craters may represent previous FFCs.

The study of mare-filled craters within 17% (Nelson et al., 2014) of the lunar surface can be applied to the highland regions, whose craters' floor depths are relatively shallow. Highlands' craters with shallow crater floor depth may host mare infilling within them, but they are successively mantled by ejecta materials.

6.1.2 Recent tectonic activity in and around the Posidonius crater, Moon

The study of the mare-filled Posidonius crater and its surrounding tectonic structures suggests that deep-seated fractures beneath the western floor of the crater, possibly originating from basin fractures or load-induced subsidence of mare-filled, served as pathways for multiple stages of volcanism and intrusive magmatism, dating back up to ~3.1 billion years ago. This magmatism activity led to slumping on the crater's eastern wall. The tectonic features, mainly distributed in the western region, are indicative of recent activity on the Moon, whose age ranges from ~1.5 billion years to

~26 million. These tectonic features are likely formed by the reactivation of these deep-seated fractures during the Eratosthenian period and continuing into the Copernican period. The cause of reactivation is possibly due to stresses from lunar recession forces, diurnal tidal stresses at apogee, and global contraction. The resulting tectonic features include wrinkle ridges, lobate scarps, splay faults, and small-scale graben. The small-scale graben formed on the elevated western floor of the Posidonius crater were formed by flexural bending resulting from the reactivation of this fault rather than the previously proposed magma intrusion uplift. Additionally, a combination of complex modification processes, including moat-forming intrusion, crater floor subsidence, and lava-filled rift tectonics associated with a blind thrust fault, could have formed the Rimae Posidonius. A small rille on the northwest floor, resembling the Rimae Posidonius but lacking signs of lava flow, supports the hypothesis of its formation through complex modification processes.

6.1.3 Deformation of the Gruithuisen region lava tube under compressional stress on the Moon

A combined numerical simulation and morphometric analysis of the Gruithuisen region's lava tube revealed that compressional tectonic stress not only formed features like wrinkle ridges and lobate scarps but also caused unique structural deformations such as collapsed pits and raised features. The deformation of the lava tube under varying compressional tectonic stress led to these distinctive structural changes. These findings provide insights into potential morphological transformations that lunar lava tubes could undergo under similar compressional tectonic stress. Furthermore, the study underscores the importance of exercising caution when distinguishing between an intact lava tube and a wrinkle ridge.

6.2 Future Outlook

1. In the future, the plan is to delve deeper into the study of the interactions between impact cratering and tectonism. This will include a detailed morphological analysis and numerical simulations to understand how these processes could influence each other on the Moon.

2. Mare-infilling in simple craters could be sourced from the shallowest

stalled recent magma reservoirs, as fractures generated during simple crater formation should be relatively shorter in depth than those generated by complex craters and impact basins. Further exploration of such small, mare-filled craters in the near future could offer valuable insights into shallow, stalled magma reservoirs. In future studies, we also plan to incorporate gravity datasets to provide additional constraints and enhance the interpretation of mare-filled crater evolution.

3. Mare-modified FFCs refer to craters that have undergone modification by mare activity subsequent to their formation as floor-fractured craters. These craters suggest that the same crater witnessed multiple episodes of magmatism. It raises the question of whether completely filled mare craters may represent previous FFCs. Further studies can explore this transition from FFCs to mare-filled craters to deepen the understanding of the evolution of magmatism processes.

4. The study of shallow mare-filled craters within 17% of the lunar surface can be applied to the highland regions whose craters' floor depths are relatively shallow. Highlands' craters with shallow crater floor depth may host mare infilling within them, but currently, they are mantled by ejecta materials.

5. The formation of a Rimae Posidonius likely resulted from a combination of complex modification processes—a moat-forming intrusion (Jozwiak et al., 2012), subsidence of the crater floor (Schultz, 1976; Wilson and Head, 2018), and lava-filled rifts tectonics associated with blind thrust fault (Andrews-Hanna et al., 2014). A small rille on the northwest floor resembling the Rimae Posidonius may be an undeveloped rille with no sign of lava flowing, supporting our hypothesis that this rille may also result from complex modification processes. Furthermore, this study could utilize numerical simulations to better understand the complex deformation mechanisms involved.

6. The potential of lava tubes in the context of habitability is another important aspect that can be taken up in future studies, as these subsurface volcanic features may offer naturally shielded environments with stable thermal conditions and protection from radiation, making them promising candidates for future exploration and habitation.

7. The study of the Gruithuisen region lava tube under compressional

stress on the Moon underscores the importance of exercising caution when distinguishing between an intact lava tube and a wrinkle ridge. This study can be taken up in the near future to achieve a clearer distinction between these geological features.

8. Additionally, the above-highlighted outlook can be extended to other lunar regions to gain broader insights into evolution and geodynamics.

Appendix-I

Table AI-1: Measurements of 324 mare-filled craters and ages of 66 mare units measured in this study, along with 65 from previous studies, are listed. The asterisk (*) represents the common mare unit area of mare-filled craters, and texts highlighted in red are mare covered areas mapped in this study. The plus sign (+) represents the ages of a single mare unit, and the texts highlighted in green are mare ages given by previous studies.

Platform	Link
Zenodo	https://zenodo.org/records/11570370
Icarus Doi	https://doi.org/10.1016/j.icarus.2022.115298

Table AI-2: Chandrayaan-2 (TMC-2) image IDs

Name	**Chandrayaan-2**
Liebig H	ch2_tmc_ndn_20200209T0626426134_d_oth_cnb
Crater (unnamed)	ch2_tmc_ndn_20191219T2239092459_d_oth_d18
Briggs A	ch2_tmc_ndn_20191218T1714166346_d_oth_d18
Hohmann	ch2_tmc_ndn_20200116T1227206758_d_oth_d18

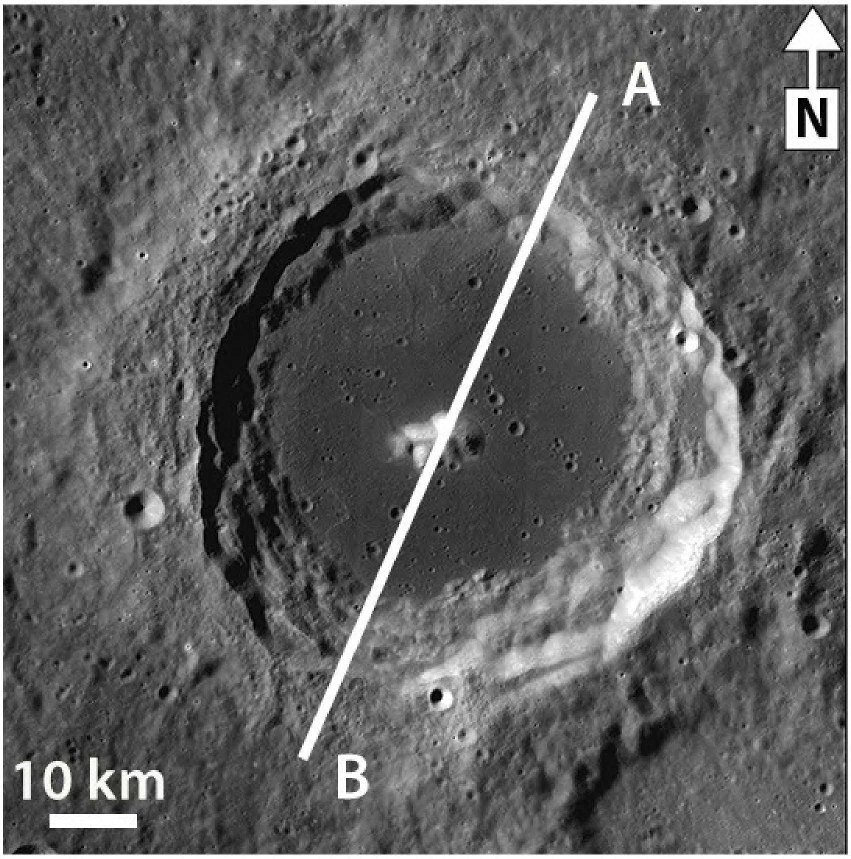

Figure AI-1: The Jenner (42°S, 96°E), a mare-filled crater with greater central peak height than the expected peak height by Pike (1977) (solid red) and Krüger et al. (2018) (solid green).

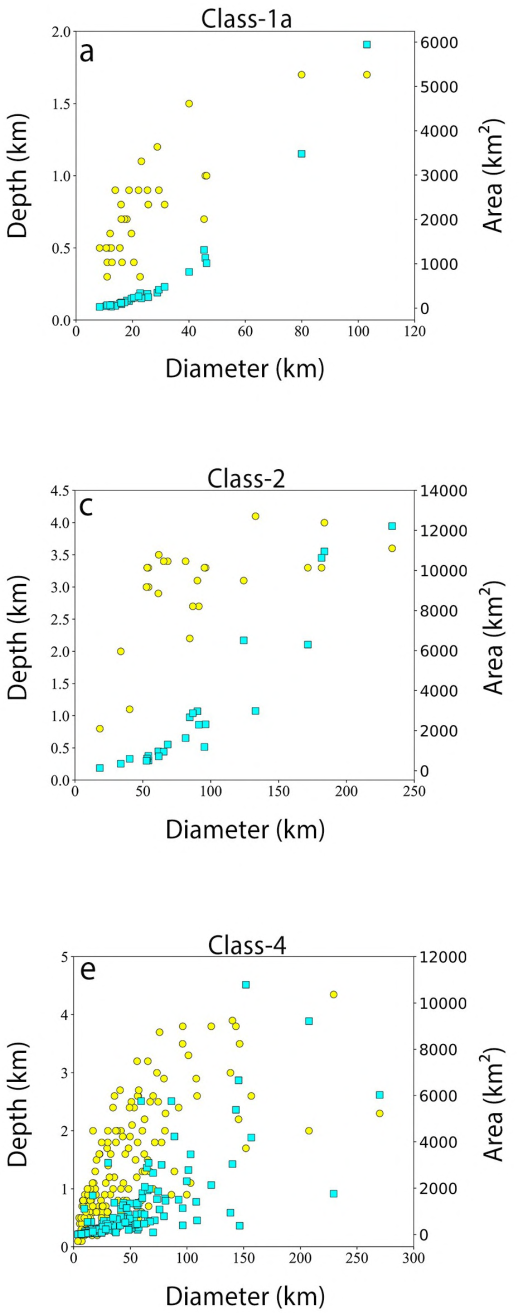

Figure AI-2: Diameter vs. Depth plots (yellow) and Diameter vs mare covered floor area plots (cyan) of mare filled craters classes.

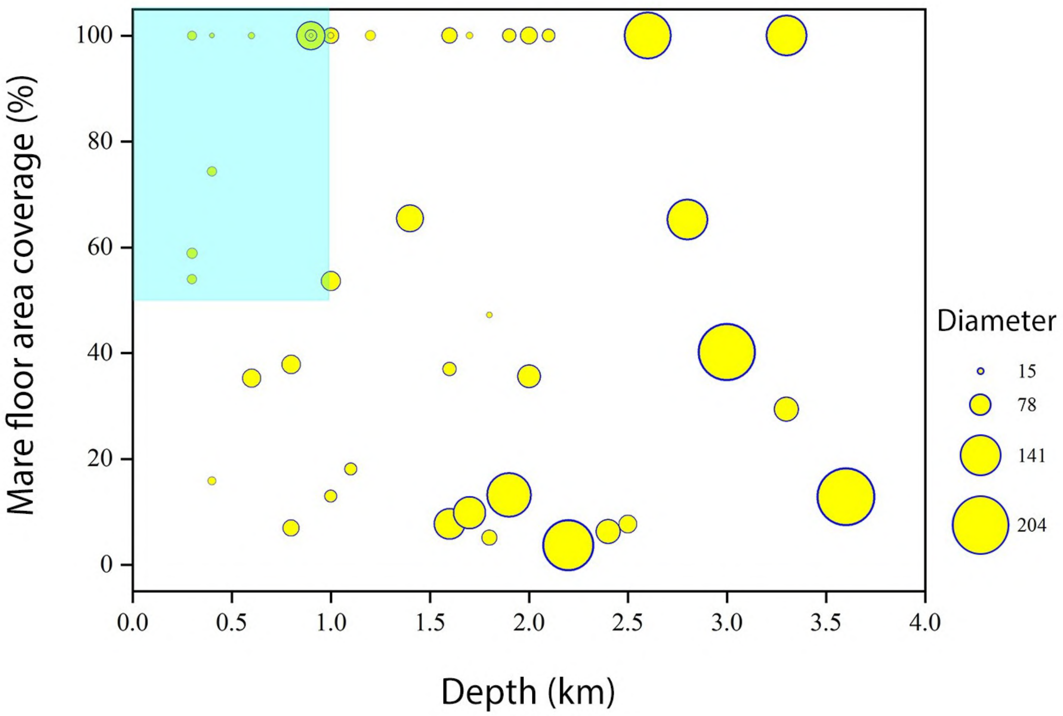

Figure AI-3: Plot of class 3 mare floor area coverage vs depths with varying diameters.

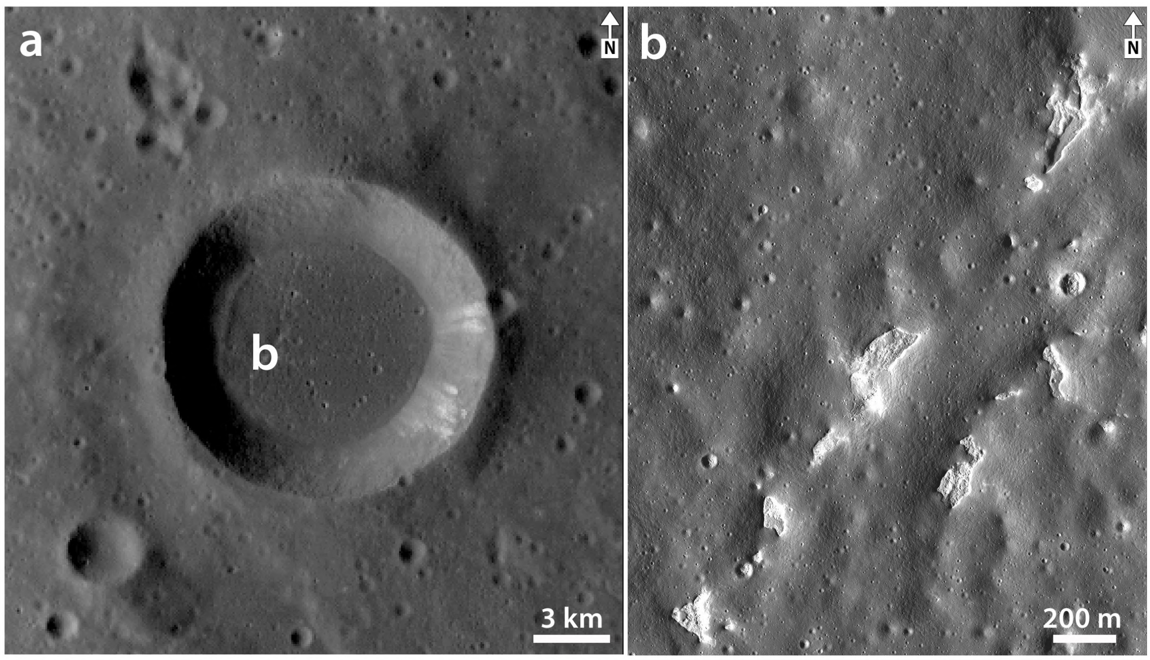

Figure AI-4: a) The Sosigenes (8.7°N, 17.6°E) mare-filled crater and b) Irregular Mare Patches (IMPs) on the floor of the Sosigenes crater.

Appendix-II

Table AII-1: IDs for 154 NAC images used in the study.

M192753946RE	M1195241591RE	M1123406204RE	M157391825LE
M190402144RE	M1157578065RE	M1203474059RE	M155030843LE
M190402144LE	M1236444890RE	M181016578RE	M1241128735RE
M190394996RE	M1126964359RE	M1184640066LE	M1225799359RE
M190394996LE	M1157585184RE	M183339730LE	M1223450315LE
M185677216RE	M1105759451RE	M1203474059LE	M1221101213RE
M185677216LE	M192789631RE	M180980846LE	M1221101213LE
M183332663RE	M1098679960RE	M1096343478LE	M1215247118LE
M180980846RE	M1111649933RE	M181016578LE	M1215233040RE
M159746292RE	M1218773130RE	M1218751980LE	M1215233040LE
M1188143290RE	M1197576089RE	M1138738250LE	M1154037629RE
M1182289525RE	M1230525721RE	M1136384626LE	M192775391RE
M1182289525LE	M1199925062RE	M1190532879LE	M1123413334RE
M1177585954RE	M1199932087RE	M165659105RE	M1129296857RE
M1177564593RE	M1230518698RE	M1236430822LE	M190416512LE
M1177564593LE	M1162255085RE	M1188164347LE	M1159912932RE
M1164624691LE	M1162255085LE	M1151681365LE	M137352732LE
M1164603322RE	M1159891695RE	M1098672765LE	M1105752249RE
M1228176668LE	M1159891695LE	M1236430822RE	M1096343478RE

Table AII-1: **C**ontinuation.....

M1098658474RE	M1129275563RE	M1157563796RE	M1096293460RE
M1199924943LE	M1234067891RE	M1218751980RE	M1096300483RE
M1096379115LE	M1101023438RE	M1225841554LE	M1123434646LE
M1210534943RE	M1192852158RE	M1096293460LE	M111415577RE
M1210534943LE	M1188164347RE	M1218751980LE	M1129318284LE
M1208171955RE	M1188157332RE	M1289319410LE	M1098679960LE
M1199932087LE	M1188157332LE	M1267003263LE	M1114000794LE
M1199939069LE	M1203481114LE	M181016578RE	M1169323327LE
M1157563796LE	M1199932087RE	M180980846LE	M1151681365RE
M180988010RE	M165659105LE	M1154030547RE	M1129282616RE
M1154030547RE	M192796817LE	M1157585184LE	M1175240781LE
M1142248406LE	M1212898039RE	M1111649933LE	M1218773130LE
M1114000794RE	M1190532879RE	M1105752249LE	M1212912138LE
M1175240781RE	M192796817RE	M1105759451LE	M1129275563LE
M1199946106RE	M1195241591LE	M1126950178LE	M1123392061RE
M1245840811LE	M1236444890LE	M1105716510LE	M1118688964LE
M1111621632RE	M1197561960RE	M1096379115RE	M1113972392RE
M1129282616LE	M1197561960LE	M1159905853RE	M1111614408RE
M1234067891LE	M1218759000LE	M1199924943RE	M1108088900LE
M1108017413RE	M1108017413LE		

Table AII-2: Details of the ages of wrinkle ridges and lobate scarps–hanging walls and footwalls, the fractured floor, and the resurfaced lava floor. WR: Wrinkle ridge, LB: Lobate scarp, HW: Hanging wall, and FW: Foot wall.

LOCATION	LONGITUDE	LATITUDE	FIGURE NO.	SLOPE	FEATURE
	deg	deg		deg	
1	29.62	34.90	A2-4a	10	WR
2	28.46	33.32	A2-4b	10	LS
	28.40	33.34	A2-4c	15	WR
3	27.89	32.32	A2-4d(iii)	15	LS
			A2-4d(iv)		
4	28.03	31.81	A2-4e	20	LS
			A2-4d		
	27.96	31.80	A2-4f	10	WR
5	27.98	31.03	A2-4g(iii)	15	LS
			A2-4g(iv)		
6	28.12	30.56	A2-4h	25	LS
7	28.64	28.75	A2-4i	10	WR
-	28.69	32.42	A2-5b	-	Resurfaced lava floor
-	30.40	32.00	A2-5c	-	Fractured floor

Table AII-2: Continuation.....

LOCATION	NAC_ID	INC ANGLE
		deg
1	M1218751980LE	73
2	M190416512LE	52
3	M1199939069LE	69
4	M1157563796RE	77
5	M180988010RE	71
6	M1203481114LE	75
7	M1289319410LE	59
-	WAC	-
-	WAC	-

Table AII-2: Continuation.....

LOC	NAME	COUNT AREA	COUNT CRATERS	FIT DIA.
		km^2		m
1	LOC 1_WR	38.5	554	300 - 3000
2	LOC 2_LS	0.6	194	-
	LOC 2_WR	1.5	290	32 - 600
3	LOC 3_LS_HW	0.9	113	-
	LOC 3_LS_FW	0.3	123	23 - 300
4	LOC 4_LS_FW	0.3	123	15 - 300
	LOC 4_LS_HW	0.7	121	27 - 400
	LOC 4_WR	0.5	147	15 - 350
5	LOC 5_LS_HW	0.8	202	17 - 500
	LOC 5_LS_FW	0.4	171	-
6	LOC 6_LS	0.3	119	-
7	LOC 7_WR	1.0	647	35 - 500
-	Resurfaced lava floor	2114	176	740m - 25km
-	Fractured floor	1650	109	900m - 20km

Table AII-2: Continuation.....

LOCATION	CumF	N(1)	PDF	N(1)
		km^(-2)		km^(-2)
1	2.2 (+0.9, -0.10) Ga	1.88 x 10^(-3)	1.9 (±0.7) Ga	1.61 x 10^(-3)
2	-	-	-	-
	110 (±20) Ma	8.84 x 10^(-5)	120 (±30) Ma	1.01 x 10^(-4)
3	-	-	-	-
	85 (±30) Ma	7.12 x 10^(-5)	84 (±30) Ma	7.01 x 10^(-5)
4	28 (±10) Ma	2.31 x 10^(-5)	29 (+10, -9) Ma	2.43 x 10^(-5)
	79 (±20) Ma	6.66 x 10^(-5)	100 (±30) Ma	8.58 x 10^(-5)
	100 (±10) Ma	8.67 x 10^(-5)	100 (±10) Ma	8.40 x 10^(-5)
5	38 (±8) Ma	3.15 x 10^(-5)	38 (±8) Ma	3.20 x 10^(-5)
	-	-	-	-
6	-	-	-	-
7	120 (±40) Ma	1.02 x 10^(-4)	140 (±40) Ma	1.14 x 10^(-4)
-	2.5 (+0.5, -0.6) Ga	2.14 x 10^(-3)	2.8 (+0.4, -0.5) Ga	2.39 x 10^(-3)
-	3.6 (+0.05, -0.07) Ga	7.62 x 10^(-3)	3.6 (+0.05, -0.07) Ga	7.0 x 10^(-3)

Table AII-3: Figure 7 Chandrayaan-2 (TMC-2) image IDs

ch2_tmc_ndn_20220612T1251305871_d_oth_d32
ch2_tmc_ndn_20220612T1449306040_d_oth_d32
ch2_tmc_ndn_20220612T1647304021_d_oth_d32

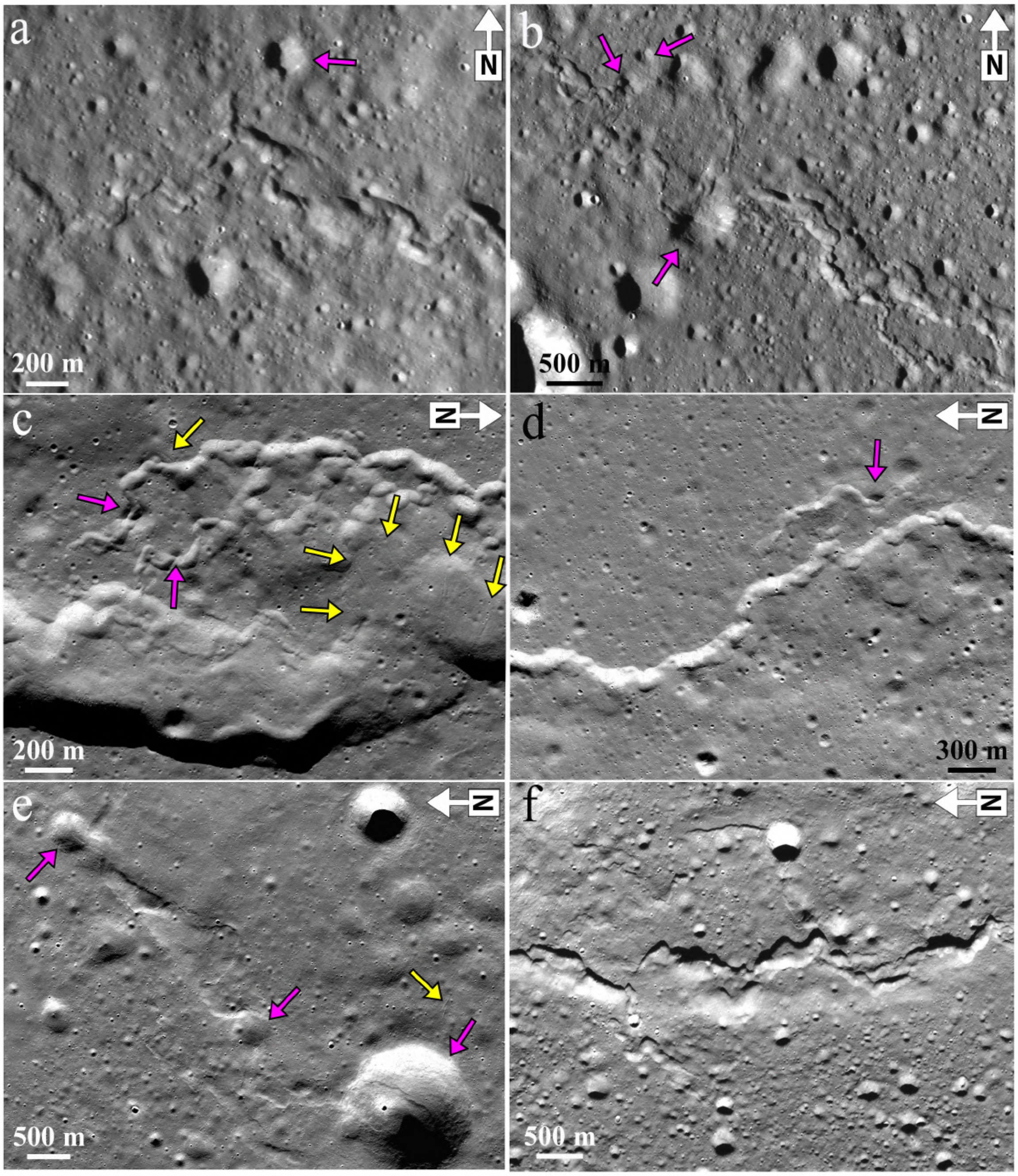

Figure AII-1: LROC-NAC images of wrinkle ridges, deformed craters by wrinkle ridges (pink arrows) and small-scale graben associated with it (yellow arrows). a) M1096379115LE and b) M1096379115LE are from the western surrounding of the Posidonius crater. c) M180980846LE and d) M1230525721RE are from the southern surrounding of the Posidonius crater. e) It is from the northern surrounding of the Posidonius (M1096300483RE). f) It is from the western surrounding of the Posidonius crater (M1096379115LE).

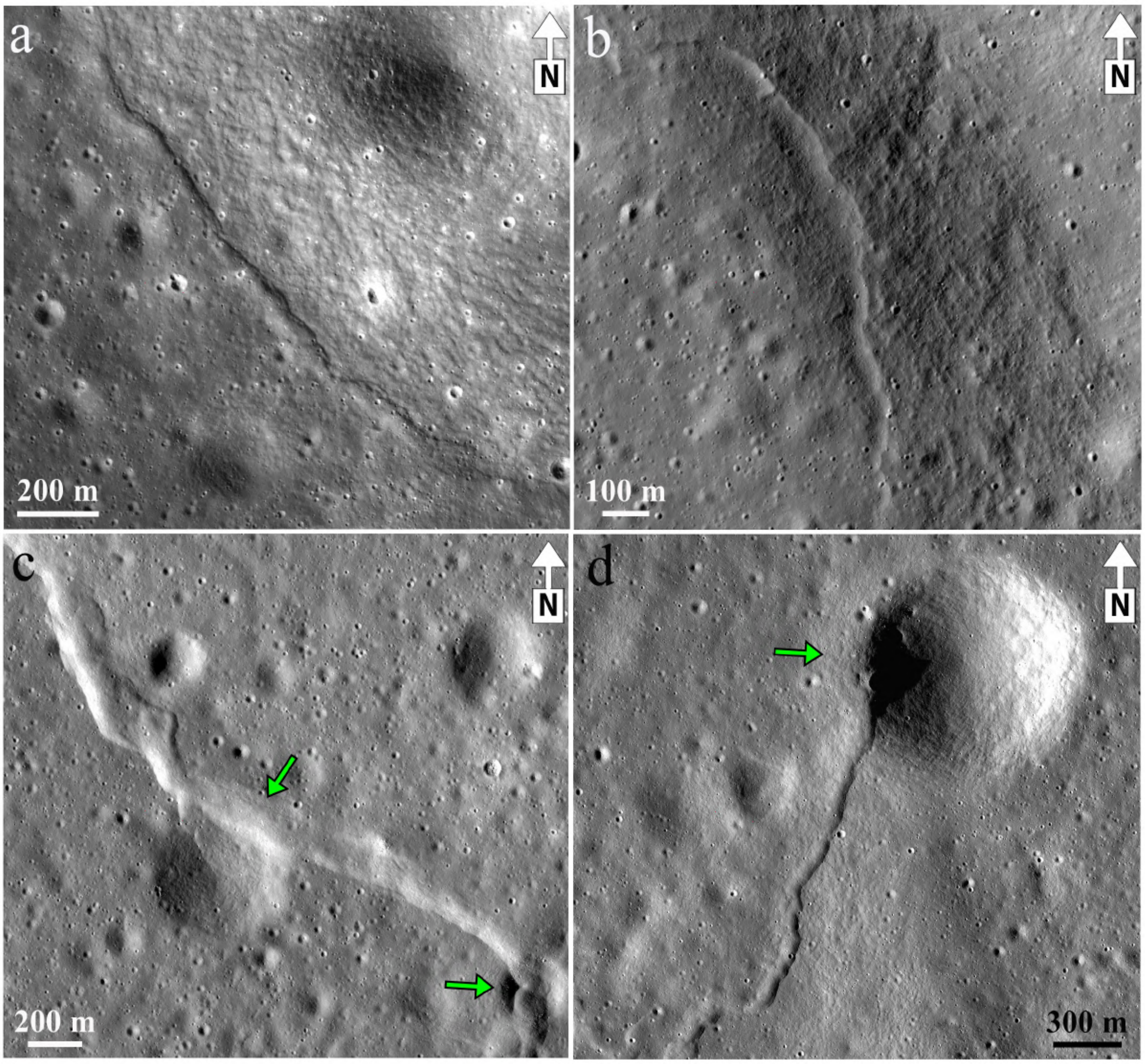

Figure AII-2: LROC-NAC images of lobate scarps and deformed craters by lobate scarps. Mapped lobate scarp a) at the north (M1159912932RE) and b) western wall of the Posidonius crater (M1123413334RE). Deformed craters by lobate scarps c) to the south of the Posidonius crater (M180980846LE) and d) to the north of the Posidonius crater (M1096300483RE, M1096300483LE).

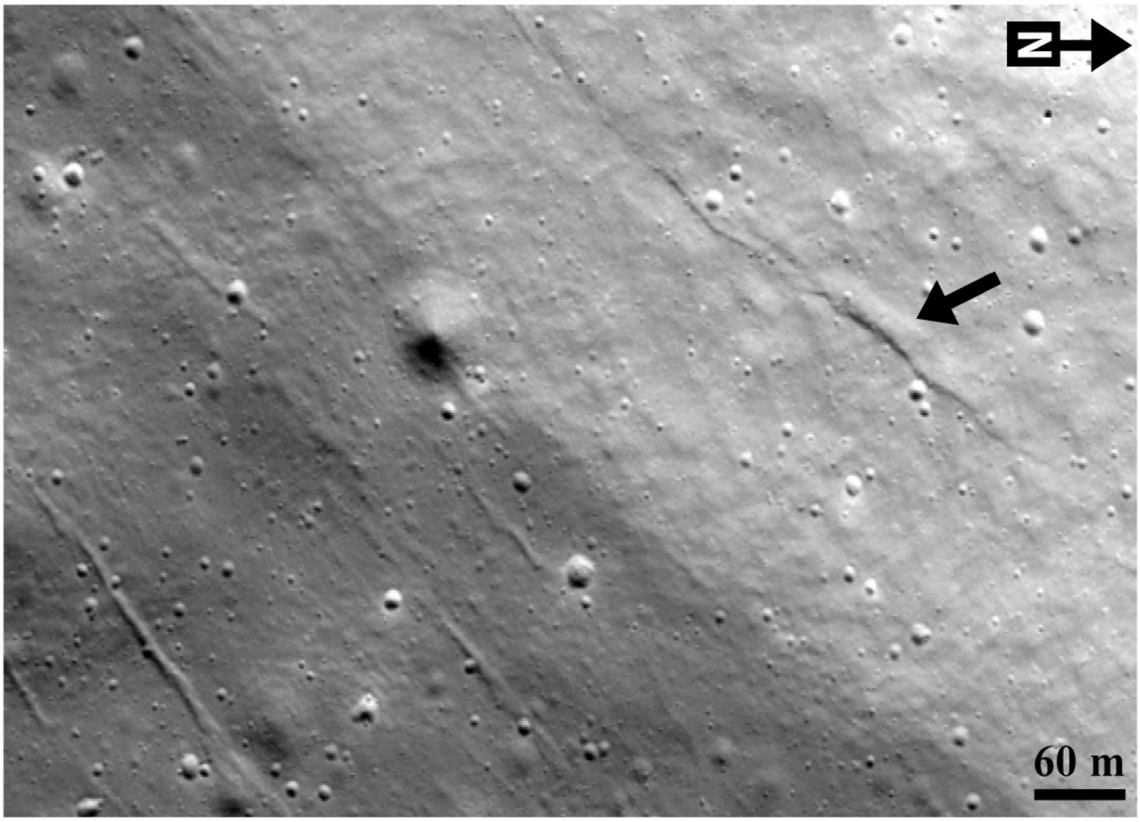

Figure AII-3: Small-scale graben formed at the western wall of the Posidonius crater (M1154037629RE).

Figure AII-4: Slope maps derived from SLDEM2015 for wrinkle ridges (WR) and lobate scarps (LB) are presented, along with NAC images with marked count area in solid and dash lines and counted craters. The figure also includes cumulative size frequency distributions (CSFDs) and a randomness analysis plot. Standard crater counting was utilized to estimate the tectonic activity ages. The details of the ages of the hanging wall of wrinkle ridges and lobate scarp and a footwall of lobate scarp are presented as follows: a) Location-1 wrinkle ridge, b) Location-2 wrinkle ridge, c) Location-2 lobate scrap, d) Location-3 lobate scrap hanging wall (solid line) and footwall (dash line), e) Location-4 lobate scrap hanging wall (solid line) and footwall (dash line), f) Location-4 wrinkle ridge, g) Location-5 lobate scrap hanging wall (solid line) and footwall (dash line), h) Location-6 lobate scrap, and i) Location-8 wrinkle ridge.

Figure AII-4: **C**ontinuation.....

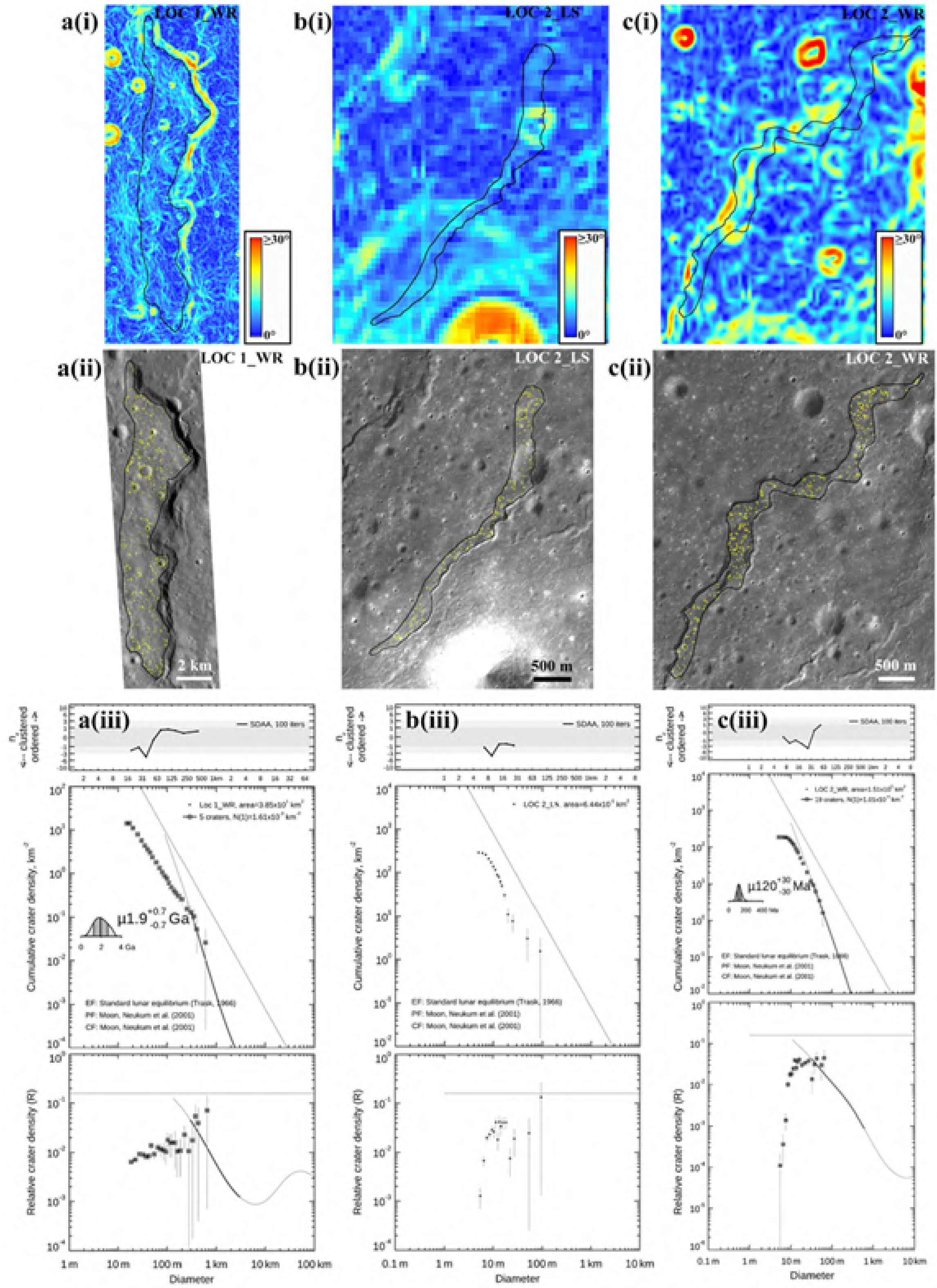

Figure AII-4: **C**ontinuation.....

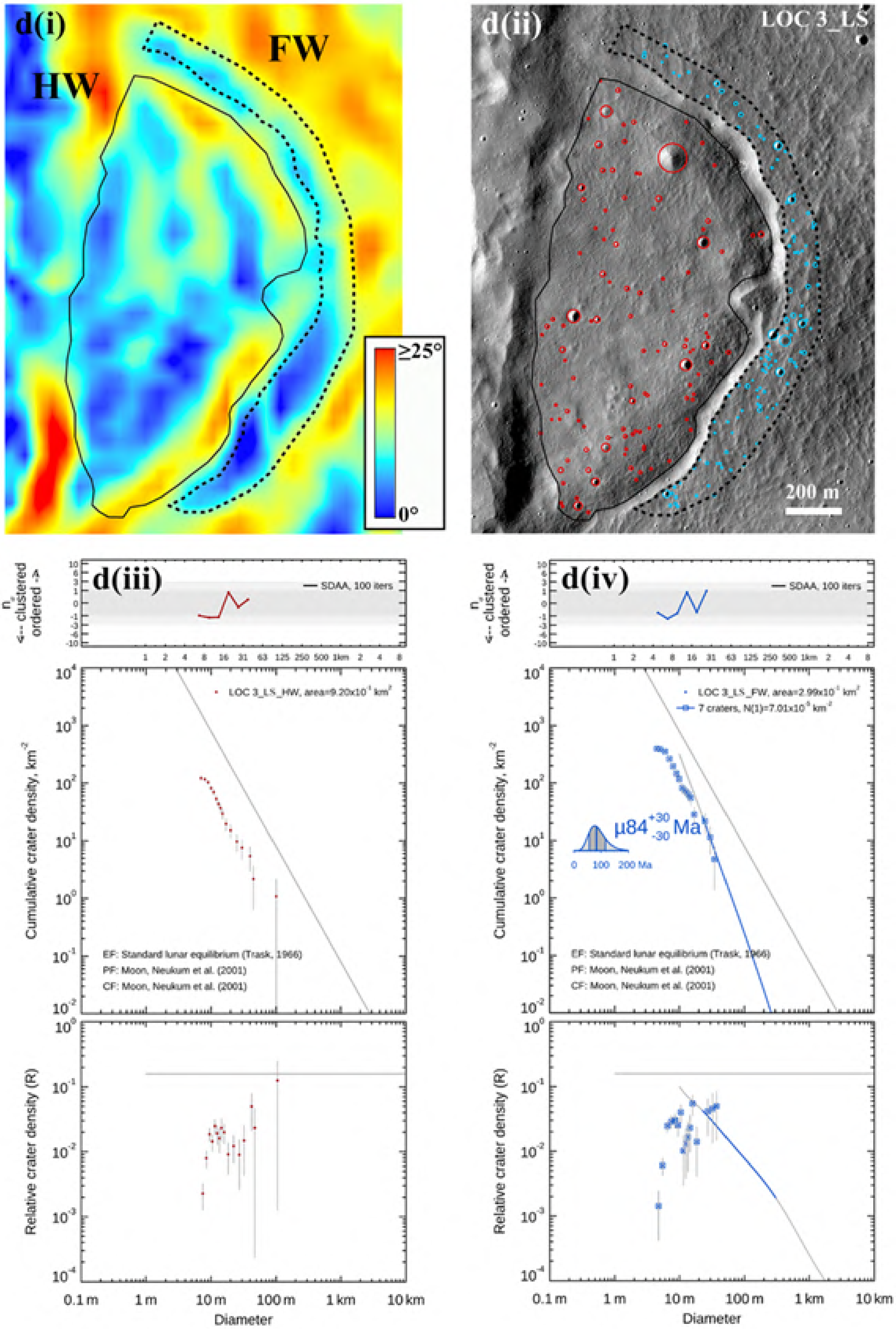

Figure AII-4: **C**ontinuation.....

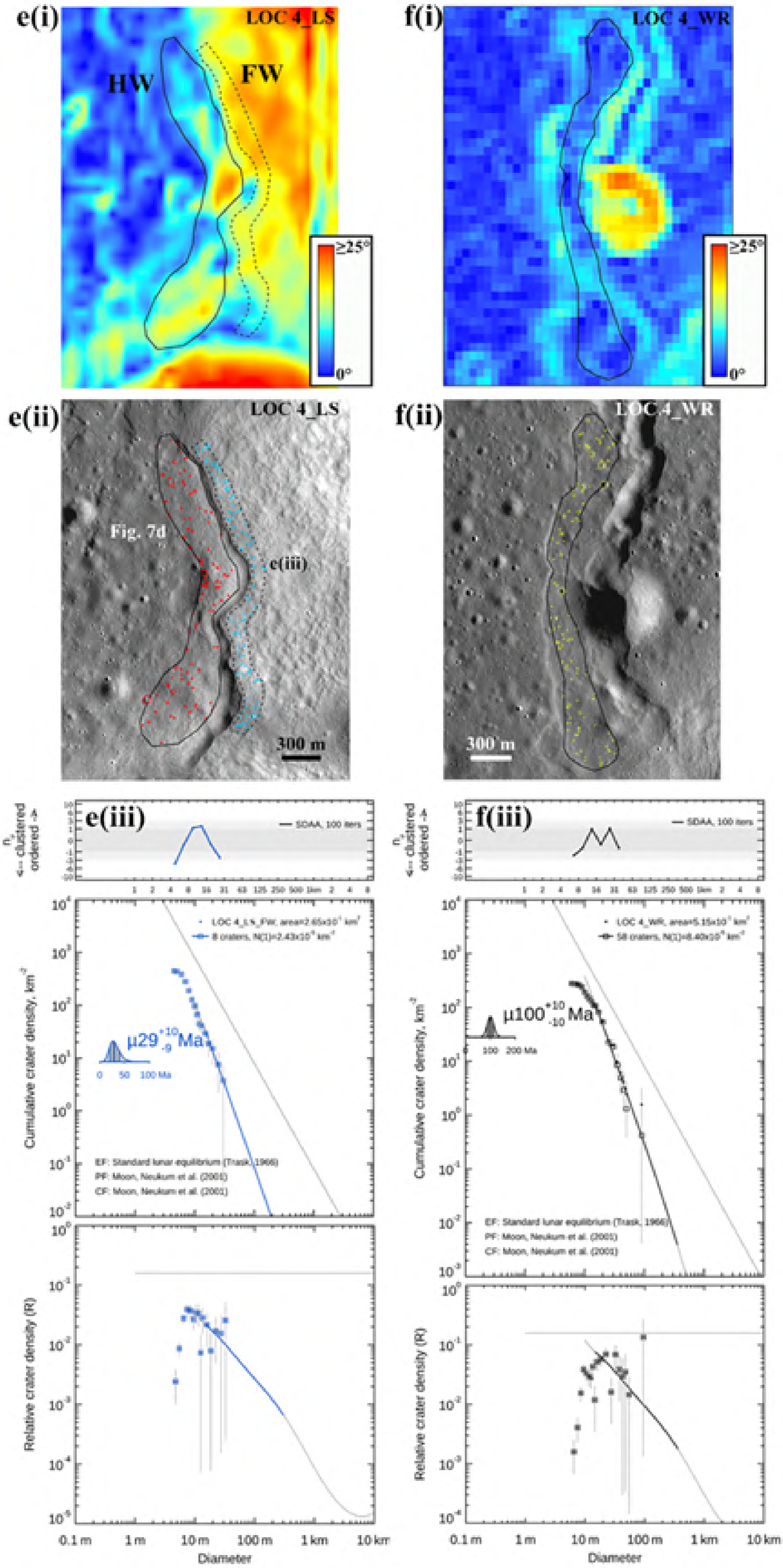

Figure AII-4: Continuation.....

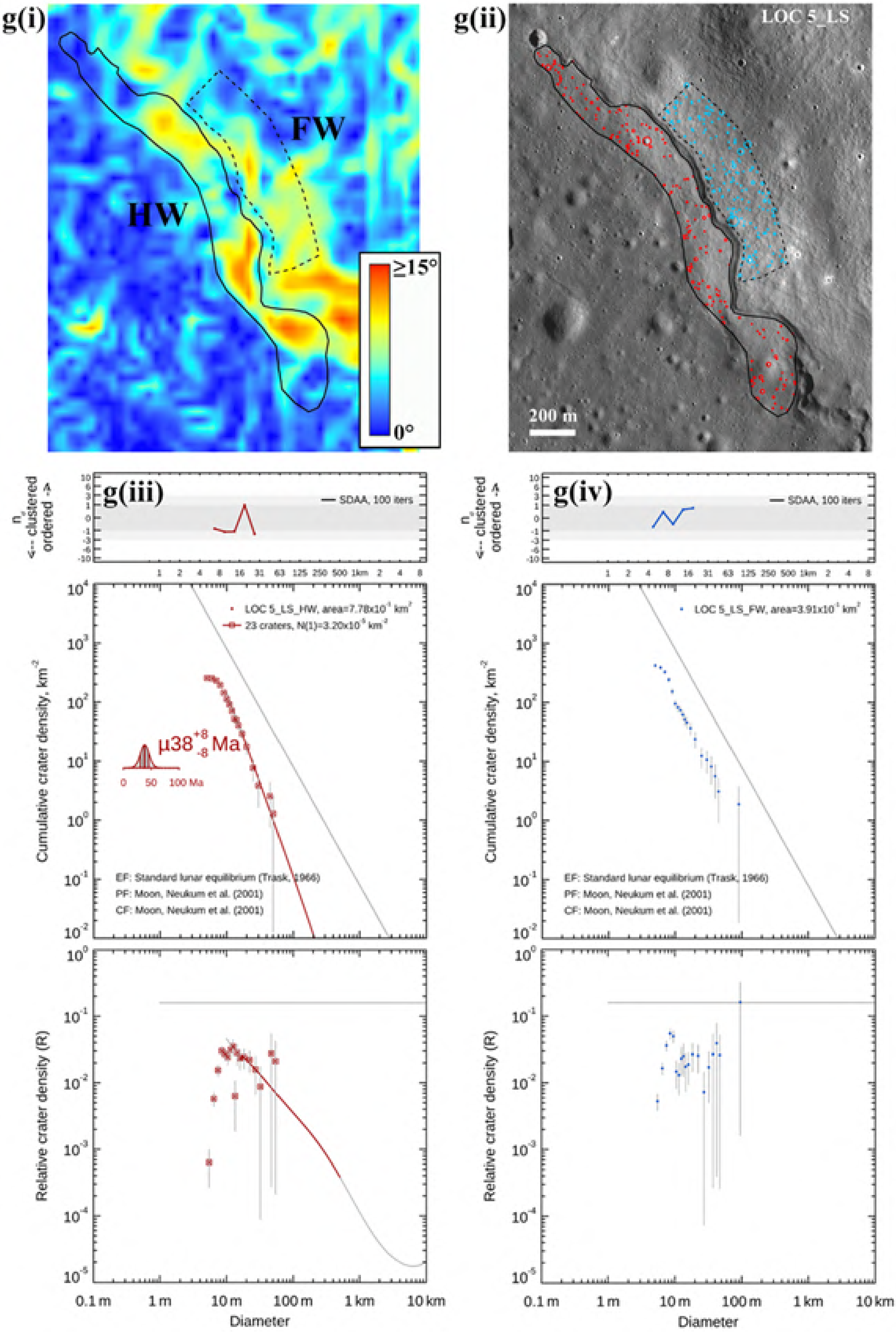

Figure AII-4: **C**ontinuation.....

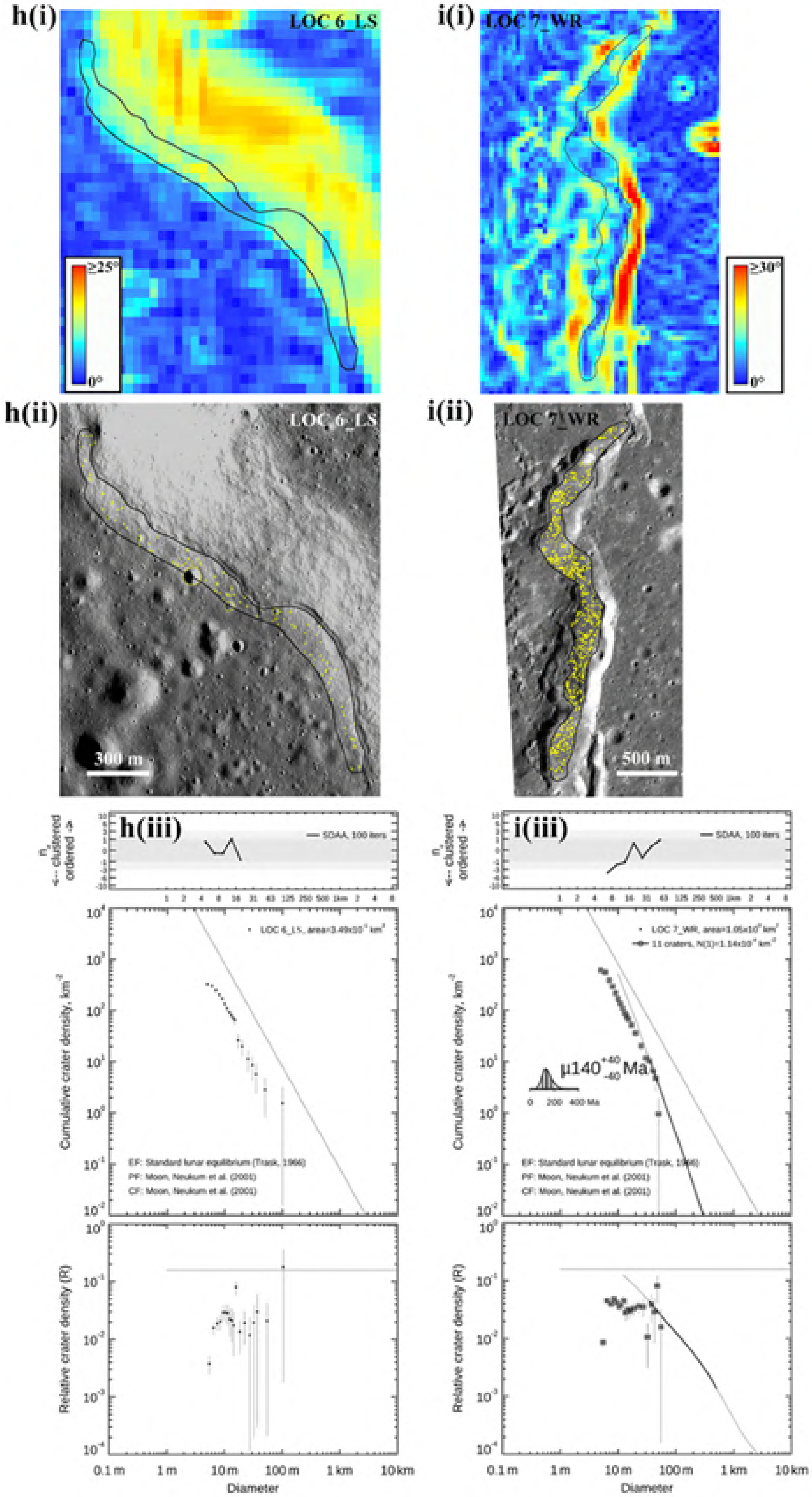

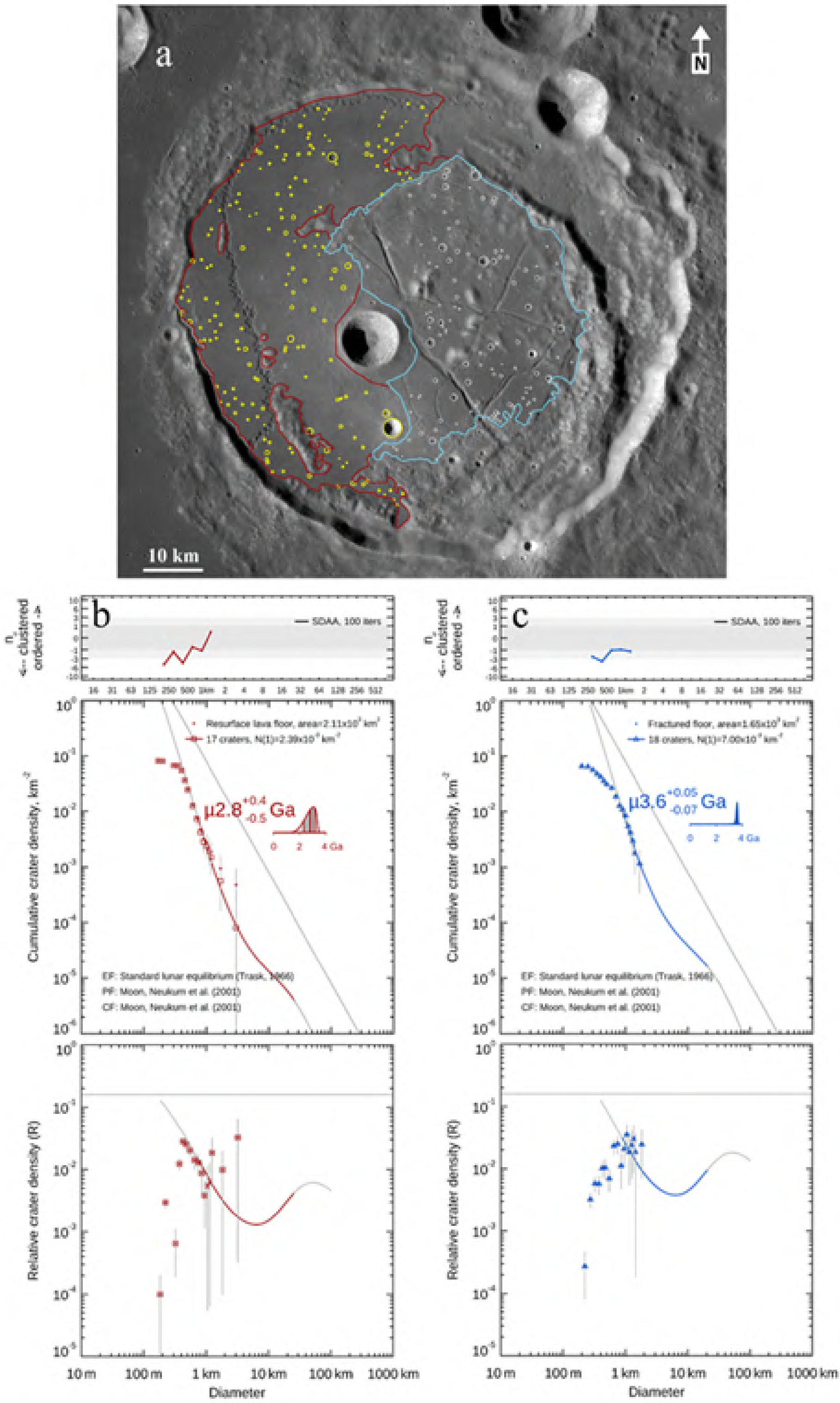

Figure AII-5: a) Craters counted on the resurfaced lava floor (red outline) and fractured floor (blue outline). Cumulative size frequency distributions (CSFDs), randomness analysis plot, and age of b) resurfaced lava floor and c) fractured floor.

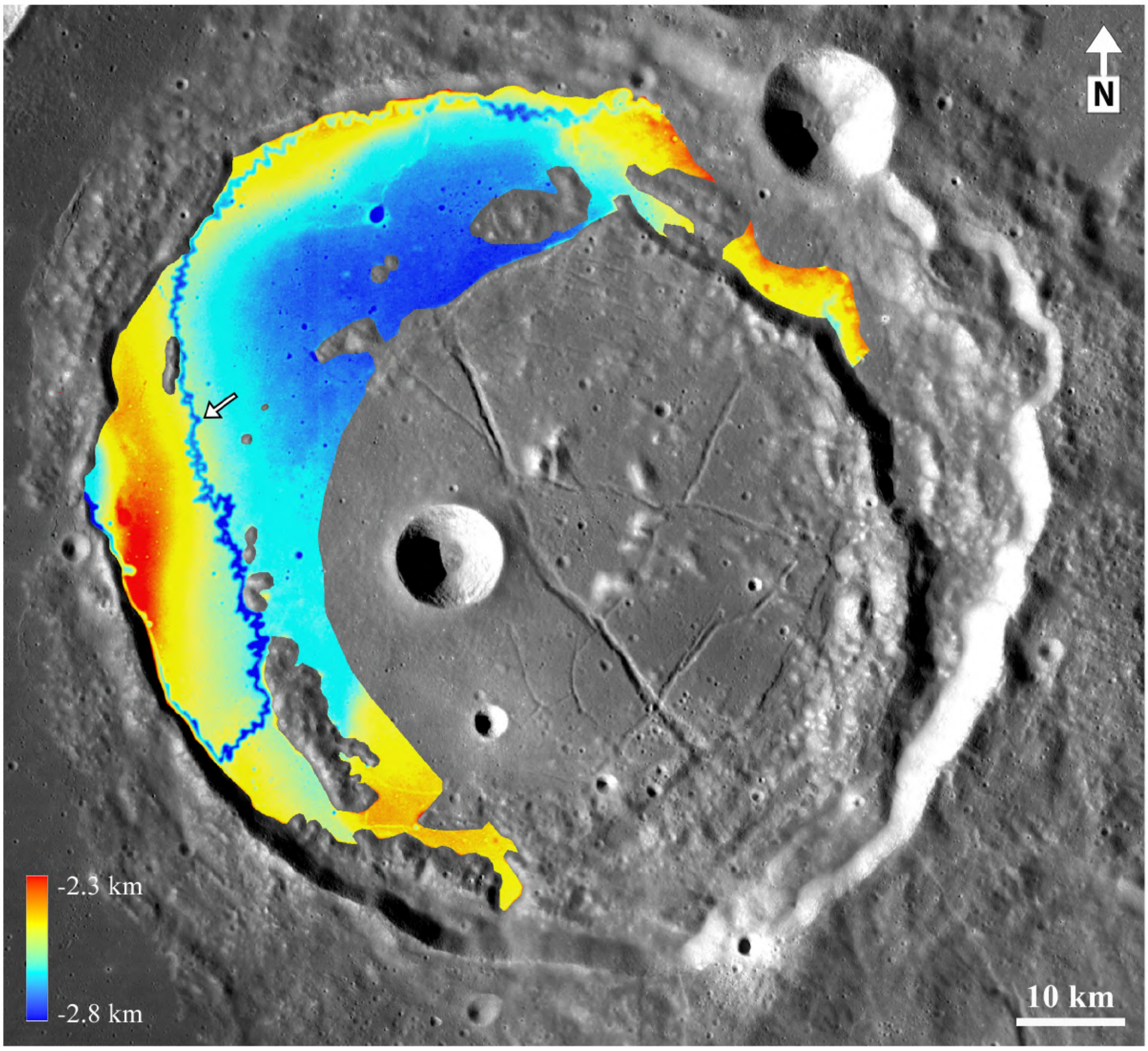

Figure AII-6: SLDEM2015 of the Posidonious floor overlaid on the LROC-WAC mosaic image. The western floor, which has a relatively higher elevation, could be a blind thrust fault, and Rimae Posidonius on the sloped surface is shown with a white arrow. The northern floor has the lowest elevation, which could be due to subsidence.

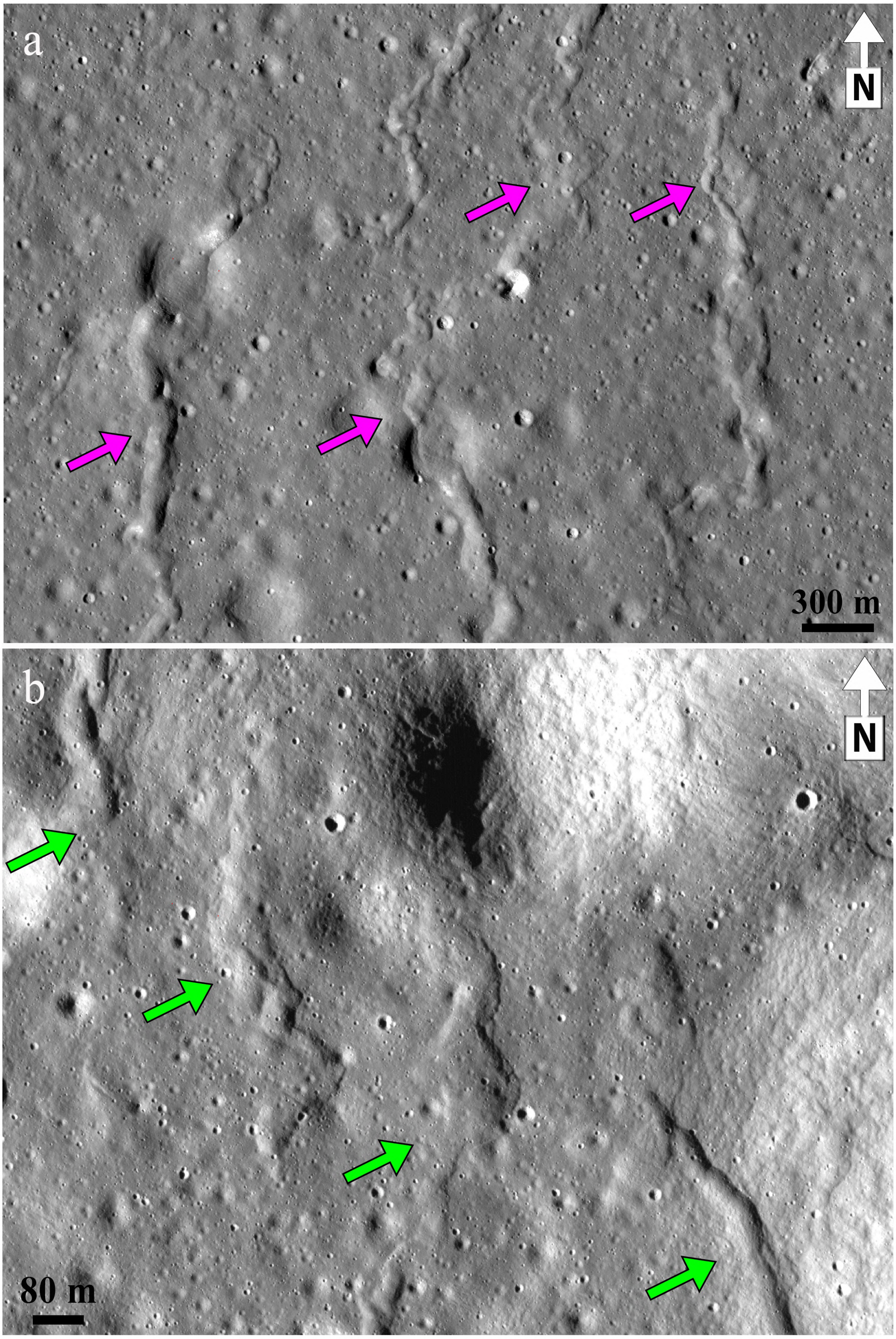

Figure AII-7: LROC-NAC images of a) wrinkle-to-wrinkle (M181016578RE, pink arrows) and b) lobate-to-lobate orthogonal transition (M1157563796RE, green arrows).

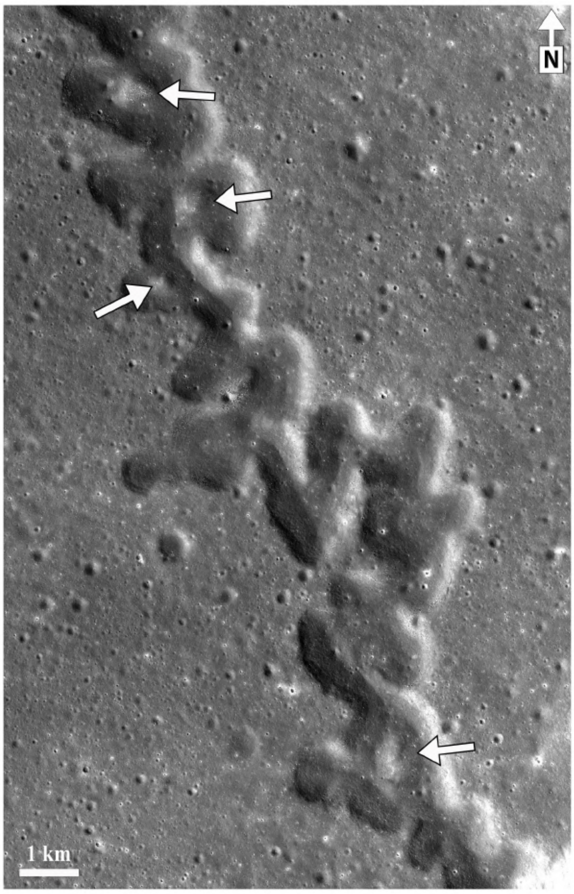

Figure AII-8: A section of Rimae Posidonius with mounds is shown in the LROC-NAC image (M1098651329LE).

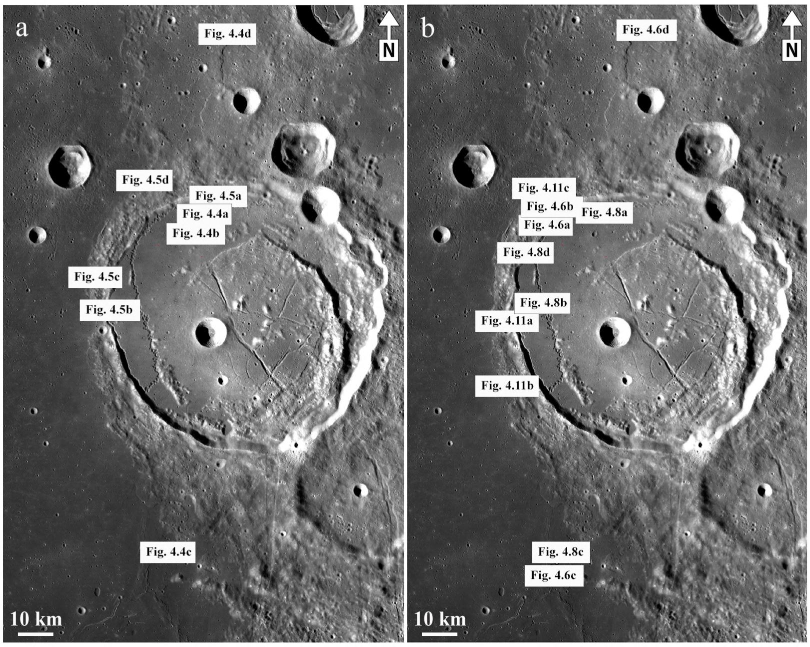

Figure AII-9: LROC-WAC mosaic images showing the locations of the LROC-NAC images shown in the manuscript figures.

Appendix-III

Table AIII-1: NAC ids utilized in this study.

NAC ID	Incident Angle	Resolution	NAC ID	Incident Angle	Resolution
	deg	m/pixel		deg	m/pixel
M181459858LE	68	1.5	M1152158374RE	53	1.4
M181459858RE	68	1.5	M1185115900LE	74	1.3
M190888252LE	55	1.5	M1185115900RE	74	1.3
M190888252RE	55	1.5	M1234553109LE	70	1.3
M1119179101LE	38	1.4	M1333294118LE	52	1.0
M1119179101RE	38	1.4	M1333294118RE	52	1.0
M1152158374LE	53	1.4	M1333301164LE	53	1.0

Table AIII-2: Material properties information.

Parameter (Unit)	Value
Young's Modulus (GPa)	30
Poisson's ratio	0.3

Table AIII-3: Details on 29 collapsed pits.

Pit No	Model No	Lat	Lon	Major axis	Minor axis	Ellipticity	Depth
		deg	deg	km	km		m
Pit Chain 1							
1	7	35.27	-43.91	1.05	0.78	0.26	100
2	6	35.25	-43.81	2.42	1.46	0.39	35
3	7	35.24	-43.67	1.70	1.60	0.06	150
4	2	35.11	-43.73	3.73	0.38	0.90	45
5	4	35.00	-43.65	1.42	0.62	0.57	90
6	4	34.92	-43.66	1.16	0.99	0.15	155
7	4	34.84	-43.59	0.93	0.28	0.70	55
8	16	34.78	-43.56	1.45	0.49	0.66	70
9	13	34.72	-43.52	1.38	0.16	0.88	30
10	4	34.67	-43.47	1.35	0.58	0.57	110
11	16	34.61	-43.45	1.59	0.56	0.65	115
12	7	34.56	-43.46	0.73	0.38	0.48	65
13	7	34.51	-43.44	0.67	0.28	0.58	45
14	4	34.45	-43.40	1.31	0.26	0.80	60
15	4	34.40	-43.36	1.31	0.60	0.54	95
16	4	34.35	-43.33	1.43	0.55	0.62	160
17	13	34.28	-43.33	1.22	0.17	0.86	30
18	7	34.20	-43.33	1.16	0.37	0.68	65
19	13	34.14	-43.37	0.94	0.71	0.25	105
20	13	34.08	-43.39	1.40	0.51	0.64	130
21	18	34.01	-43.39	1.69	0.95	0.44	225

Table AIII-3: Continuation.....

Pit No	Model No	NAC ID	Descriptions
Pit Chain 1			
1	7	M1234553109LE	Partially collapsed and raised features
2	6	M1234553109LE, M181459858LE	Collapsed with one side displaying a steeper slope
3	7	M181459858LE	Partially collapsed and raised features
4	2	M181459858LE	Channel shape collapsed
5	4	M181459858LE	Alternating collapsed and raised features
6	4	M181459858LE	Alternating collapsed and raised features
7	4	M181459858LE	Alternating collapsed and raised features
8	16	M181459858LE	One side exhibiting a more pronounced collapse
9	13	M181459858RE	Collapsed surrounded by raised features
10	4	M181459858RE	Alternating collapsed and raised features
11	16	M181459858RE	One side exhibiting a more pronounced collapse
12	7	M181459858RE	Partially collapsed and raised features
13	7	M181459858RE	Partially collapsed and raised features
14	4	M181459858RE	Alternating collapsed and raised features
15	4	M181459858RE	Alternating collapsed and raised features
16	4	M181459858RE	Alternating collapsed and raised features
17	13	M181459858RE	Collapsed surrounded by raised features
18	7	M181459858RE	Partially collapsed and raised features
19	13	M181459858RE	Collapsed with a mound
20	13	M181459858RE	Collapsed with a mound
21	18	M190888252RE	Two fused collapsed

Table AIII-3: Continuation.....

Pit No	NAC ID	Lat	Lon	Major axis	Minor axis	Ellipticity	Depth
		deg	deg	km	km		m
Pit Chain 2							
22	M1152158374RE, M1152158374LE	33.89	-43.55	1.81	1.56	0.13	100
23		33.93	-43.67	1.57	0.63	0.60	80
24		33.96	-43.70	0.83	0.40	0.51	15
25		34.01	-43.77	0.69	0.49	0.29	25
26		34.04	-43.80	0.42	0.29	0.31	20
27		34.07	-43.82	0.31	0.22	0.30	20
28		34.08	-43.84	0.14	0.11	0.19	5
Isolated pit							
29	M1333294118LE, M1185115900RE	32.42	-42.74	8.26	4.28	0.48	110
Potential Eruptive vent							
-	M1119179101LE, M1119179101RE	35.33	-44.19	-	-	-	610

Table AIII-4: Raised feature details.

Raised No	Lat	Lon	Raised Elevation	Floor Elevation	Height
	deg	deg	m	m	m
1	35.04	-43.69	-2045	-2080	35
2	34.96	-43.64	-2040	-2090	50
3	34.89	-43.63	-2065	-2110	45
4	34.81	-43.57	-2090	-2145	55
5	34.72	-43.52	-2085	-2125	40
6	34.65	-43.45	-2090	-2130	40
7	34.53	-43.43	-2045	-2115	70
8	34.43	-43.38	-2065	-2110	45
9	34.37	-43.34	-2080	-2130	50
10	34.25	-43.33	-2050	-2100	50
11	34.11	-43.39	-2060	-2100	40
12	34.05	-43.38	-2070	-2110	40
13	33.70	-43.16	-2075	-2160	85

Table AIII-5: Wrinkle ridges length and Azimuth information.

No	Length	Start_lon	End_lon	Start_lat	End_lat	Azimuth
	km	km	km	km	km	deg
1	7.61	-1297.43	-1297.50	1069.00	1061.38	0.48
2	4.26	-1298.86	-1297.56	1054.86	1050.80	-17.81
3	2.01	-1359.07	-1358.00	1062.42	1064.42	28.05
4	2.18	-1346.83	-1350.76	1067.82	1065.97	64.71
5	1.90	-1341.94	-1343.26	1068.31	1066.30	33.14
6	5.72	-1359.74	-1358.39	1071.17	1065.63	-13.72
7	4.82	-1335.69	-1339.78	1067.31	1062.16	38.41
8	9.14	-1365.60	-1365.43	1059.80	1050.35	-1.04
9	15.07	-1360.19	-1351.41	1050.51	1037.30	-33.62
10	4.91	-1270.62	-1273.06	1023.94	1018.57	24.43
11	14.55	-1317.46	-1324.71	1045.70	1030.62	25.70
12	7.84	-1312.95	-1313.52	1022.77	1014.56	3.94
13	57.37	-1314.63	-1300.55	1011.10	955.17	-14.12
14	26.56	-1343.28	-1338.98	992.72	966.41	-9.29
15	6.27	-1357.06	-1355.26	993.84	987.75	-16.39
16	7.57	-1273.14	-1271.43	1032.86	1025.43	-13.00

Table AIII-6: Details of the strain and stress values estimated from the wrinkle ridge.

No.	Lat	Lon	Cross Length (Lt)	Horizontal Length (Lo)	Change Length (ΔL)	Strain (ϵ)	Stress (σ)
	deg	deg	km	km	km		GPa
1	33.287	-43.409	5.209	5.197	0.012	2.37E-03	7.12E-02
2	33.101	-43.389	4.401	4.392	0.009	2.05E-03	6.14E-02
3	32.898	-43.354	4.938	4.932	0.006	1.29E-03	3.86E-02
4	32.732	-43.334	4.630	4.610	0.020	4.23E-03	1.27E-01
5	32.509	-43.177	10.630	10.615	0.015	1.37E-03	4.12E-02
6	32.324	-43.072	5.037	5.017	0.020	3.97E-03	1.19E-01
7	32.151	-42.989	6.525	6.509	0.016	2.51E-03	7.53E-02
8	31.956	-42.973	5.500	5.482	0.018	3.32E-03	9.95E-02
9	31.765	-42.959	5.217	5.211	0.006	1.18E-03	3.55E-02
10	31.585	-42.944	4.571	4.568	0.003	7.23E-04	2.17E-02

Table AIII-7: Results obtained from the 3D simulated model.

Deformation Mode/Model	GiF	Description
1	S14	Consecutive sagging and hogging of the lava tube roof
2	S15	Consecutive sagging and hogging of the lava tube roof
3	S16	Alternate sagging and hogging of the lava tube roof in elliptical shape
4	S17	Alternate sagging and hogging of the lava tube roof in elliptical shape
5	S18	Partially sagging and hogging of the lava tube roof in elliptical shape
6	S19	Partially sagging and hogging of the lava tube roof
7	S20	Partially sagging and hogging of the lava tube roof in elliptical shape
8	S21	Multiple alternate sagging and hogging of the lava tube roof in elliptical shape
9	S22	Multiple partially sagging and hogging of the lava tube roof in elliptical shape
10	S23	Multiple alternate sagging and hogging of the lava tube roof in elliptical shape
11	S24	Multiple partially sagging and hogging of the lava tube roof in elliptical shape
12	S25	Pair of sagging and hogging of the lava tube roof
13	S26	Hogging within the sagging of the lava tube and vice-versa
14	S27	Complex hogging within the sagging of the lava tube and vice-versa
15	S28	Multiple sagging and hogging of the lava tube roof
16	S29	Sagging of one side more pronouncedly than the other and hogging in the middle
17	S30	Complex sagging of one side more pronouncedly than the other and hogging in the middle
18	S31	Multiple pair of hogging and sagging alternatingly
19	S32	Multiple pair of hogging and sagging alternatingly
20	S33	Multiple pairs of partially sagging and hogging of the lava tube roof in elliptical shape accompanied by additional smaller deformations concentrated at the center.

Table AIII-7: Continuation.....

Deformation Mode/Model	Load Multiplier	Force (±X)	**Total Displacement**				
					X		
			Max.	Avg.	Max.	Min.	Avg.
		N	m	m	m	m	m
1	12.512	1.752E+15	1.030	0.402	0.248	-0.285	-1.21E-02
2	15.756	2.206E+15	1.001	0.236	0.254	-0.265	-2.69E-02
3	16.425	2.300E+15	1.002	0.054	0.245	-0.245	-1.18E-09
4	19.5	2.730E+15	1.001	0.027	0.166	-0.201	-1.46E-03
5	19.513	2.732E+15	1.025	0.114	0.464	-0.464	-1.24E-09
6	19.899	2.786E+15	1.100	0.354	0.346	-0.542	-8.04E-03
7	23.71	3.319E+15	1.019	0.050	0.531	-0.402	1.25E-03
8	24.193	3.387E+15	1.004	0.020	0.193	-0.193	-8.06E-11
9	28.498	3.990E+15	1.018	0.053	0.463	-0.463	-2.66E-10
10	30.776	4.309E+15	1.014	0.012	0.181	-0.184	-6.76E-04
11	34.643	4.850E+15	1.030	0.029	0.463	-0.370	1.03E-03
12	37.954	5.314E+15	1.005	0.085	0.239	-0.301	-2.71E-02
13	38.248	5.355E+15	1.026	0.085	0.251	-0.251	-3.49E-09
14	39.302	5.502E+15	1.052	0.141	0.483	-0.483	3.34E-09
15	39.568	5.540E+15	1.106	0.218	0.694	-0.396	1.56E-02
16	40.547	5.677E+15	1.078	0.165	0.341	-0.341	-5.14E-10
17	42.13	5.898E+15	1.004	0.126	0.444	-0.444	-2.50E-09
18	42.183	5.906E+15	1.004	0.031	0.238	-0.257	-3.34E-03
19	46.341	6.488E+15	1.023	0.111	0.305	-0.305	-4.58E-10
20	46.6	6.524E+15	1.031	0.062	0.446	-0.333	2.00E-03

Table AIII-7: Continuation.....

Deformation Mode/Model	Total Displacement					
	Y			Z		
	Max.	Min.	Avg.	Max.	Min.	Avg.
	m	m	m	m	m	m
1	1	-9.81E-03	0.385	5.42E-02	-5.42E-02	4.71E-10
2	1	-4.78E-01	-0.182	9.05E-02	-9.05E-02	3.95E-09
3	1	-1.00E+00	-4.83E-09	9.05E-02	-0.101	-2.68E-02
4	1	-7.88E-01	1.25E-02	0.135	-0.135	4.94E-09
5	1	-1.00E+00	7.47E-09	0.115	-0.216	-1.33E-02
6	1	-4.88E-01	0.31256	0.154	-0.154	-4.64E-10
7	1	-9.56E-01	-1.73E-02	0.179	-0.179	1.15E-09
8	1	-1.00E+00	6.54E-10	0.177	-0.138	-5.23E-03
9	1	-1.00E+00	7.59E-11	0.168	-0.250	-8.56E-03
10	1	-6.80E-01	5.99E-04	0.220	-0.220	-3.70E-11
11	1	-9.30E-01	6.69E-04	0.259	-0.259	1.90E-09
12	1	-1.02E-01	-6.24E-03	0.141	-0.141	-2.41E-08
13	1	-1.00E+00	1.22E-09	0.242	-0.187	5.97E-02
14	1	-1.00E+00	1.62E-08	0.375	-0.335	0.102
15	1	-5.35E-01	7.82E-02	0.237	-0.237	-6.19E-08
16	1	-1.00E+00	-5.52E-09	0.138	-0.389	-3.89E-02
17	1	-1.00E+00	3.90E-09	0.162	-0.363	-2.97E-02
18	1	-7.61E-01	2.04E-03	0.170	-0.170	1.77E-08
19	1	-1.00E+00	-3.80E-09	0.159	-0.293	-8.38E-02
20	1	-8.28E-01	2.58E-02	0.253	-0.253	-1.70E-08

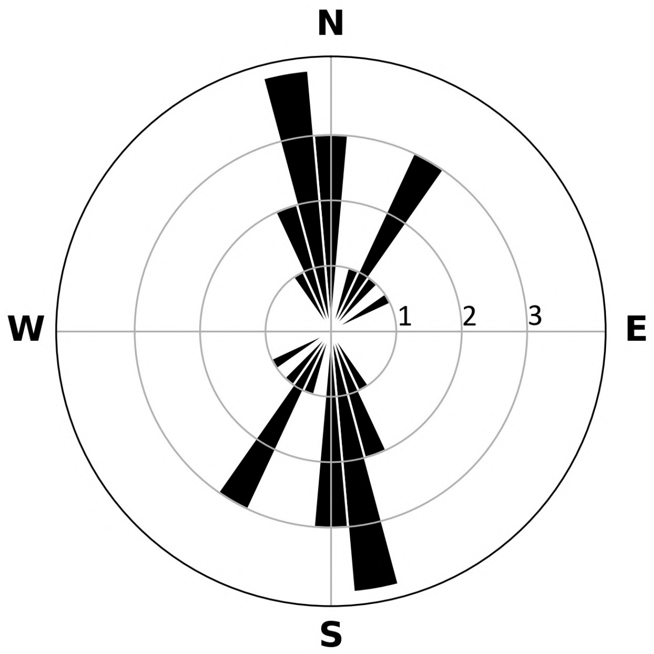

Figure AIII-1: Orientations of the wrinkle ridges predominantly trended northward.

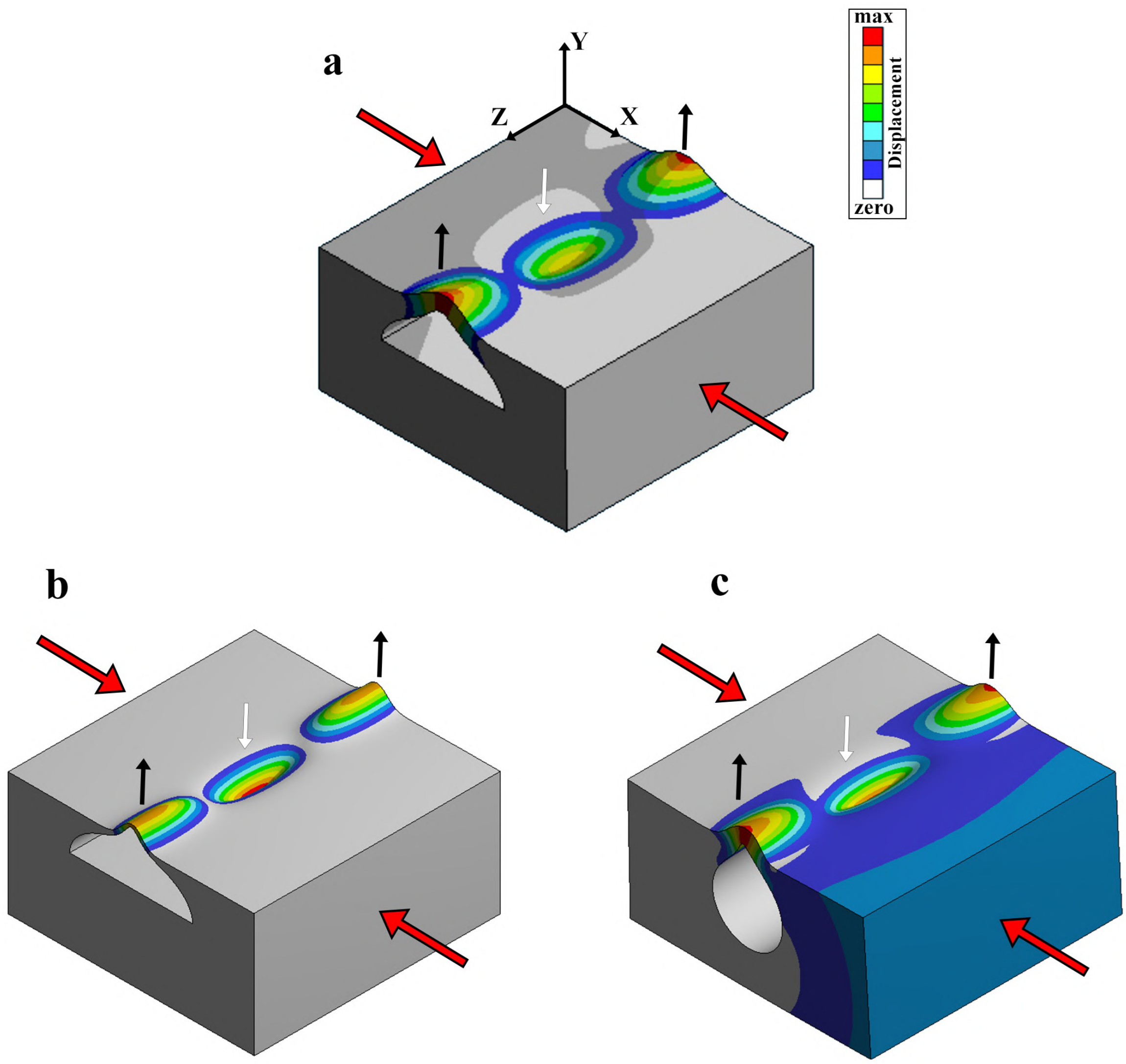

Figure AIII-2: Comparison of models in response to changes in lava tube roof thickness and tube cross-section compared to the model used in the study. All models have dimensions of 2X2X1 km³. a) The original model of the study with a lava roof thickness of 100m and a semi-elliptical cross-section. b) The model with a reduced lava roof thickness of 20m shows a similar deformation pattern to the original model. However, the deformation occurred at a smaller load multiplier, and the features became narrow, indicating that collapse may occur earlier than in the original model. The roof thickness of 20 m over 1000 m wide is unstable and will collapse due to gravity (Theinat et al., 2020). The goal of this model is to assess sensitivity to thickness. c) The Model maintaining a 100m lava roof thickness with a circular tube shape also has similar deformation, but deformation occurred at a higher load multiplier and showed narrow features. Here, we considered the simplest tube cross-section, which is circular, for simplicity. However, it can vary to more complex shapes (For details on the cross-section, please refer to (Chwała et al., 2024)). The GIFs of models can be found at https://doi.org/10.5281/zenodo.11075944

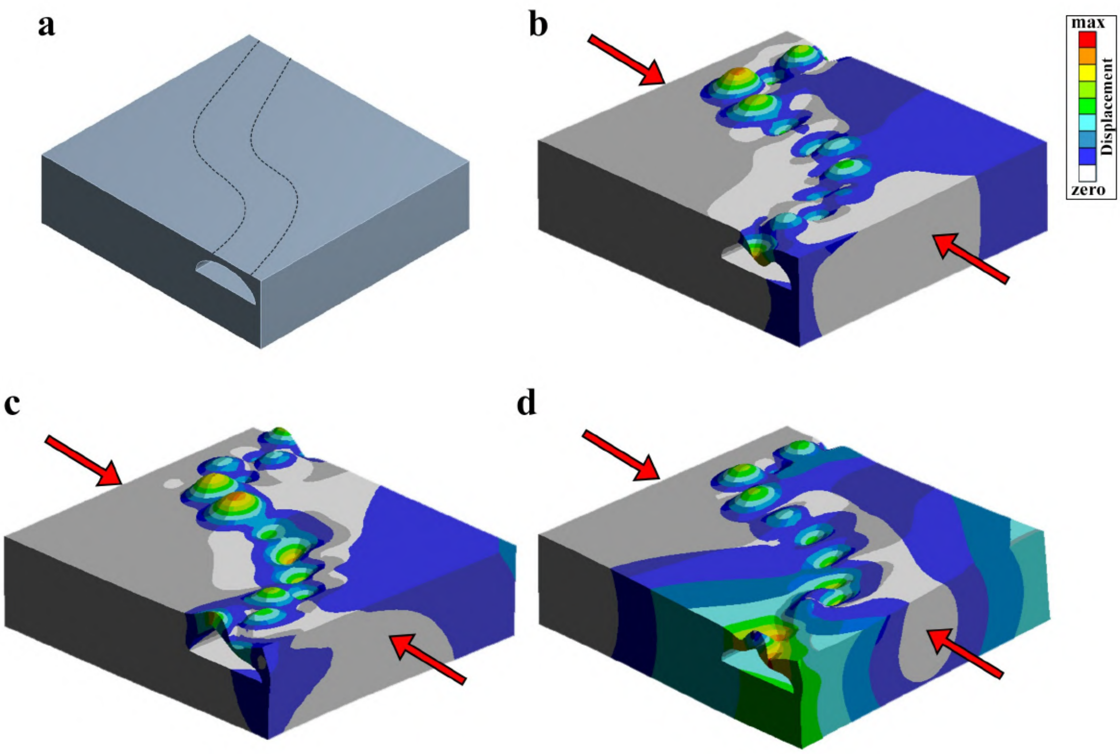

Figure AIII-3: a) An illustration of a simple curved lava tube with dimensions identical to the straight lava tube within 3500mX3700mX1000m (lXbXh) block. b-d) Highlights different deformation patterns in the curved lava tube, which incorporates deformation features observed in the straight tube. The GIFs of models can be found at https://doi.org/10.5281/zenodo.11075944

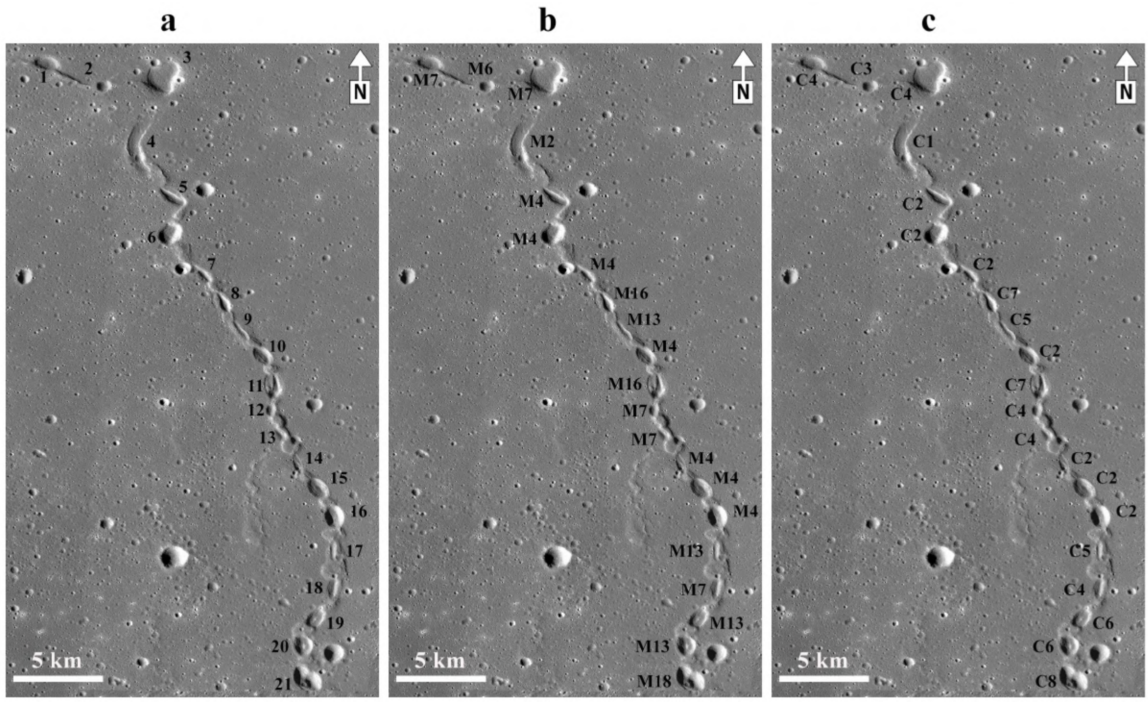

Figure AIII-4: a) Pits number and locations. b) The model aligned with the pits and associated raised features. Capital M stands for model. c) The type/characteristics of the pits and associated raised features. Capital C stands for type/characteristic. An explanation of the types can be found in the manuscript.

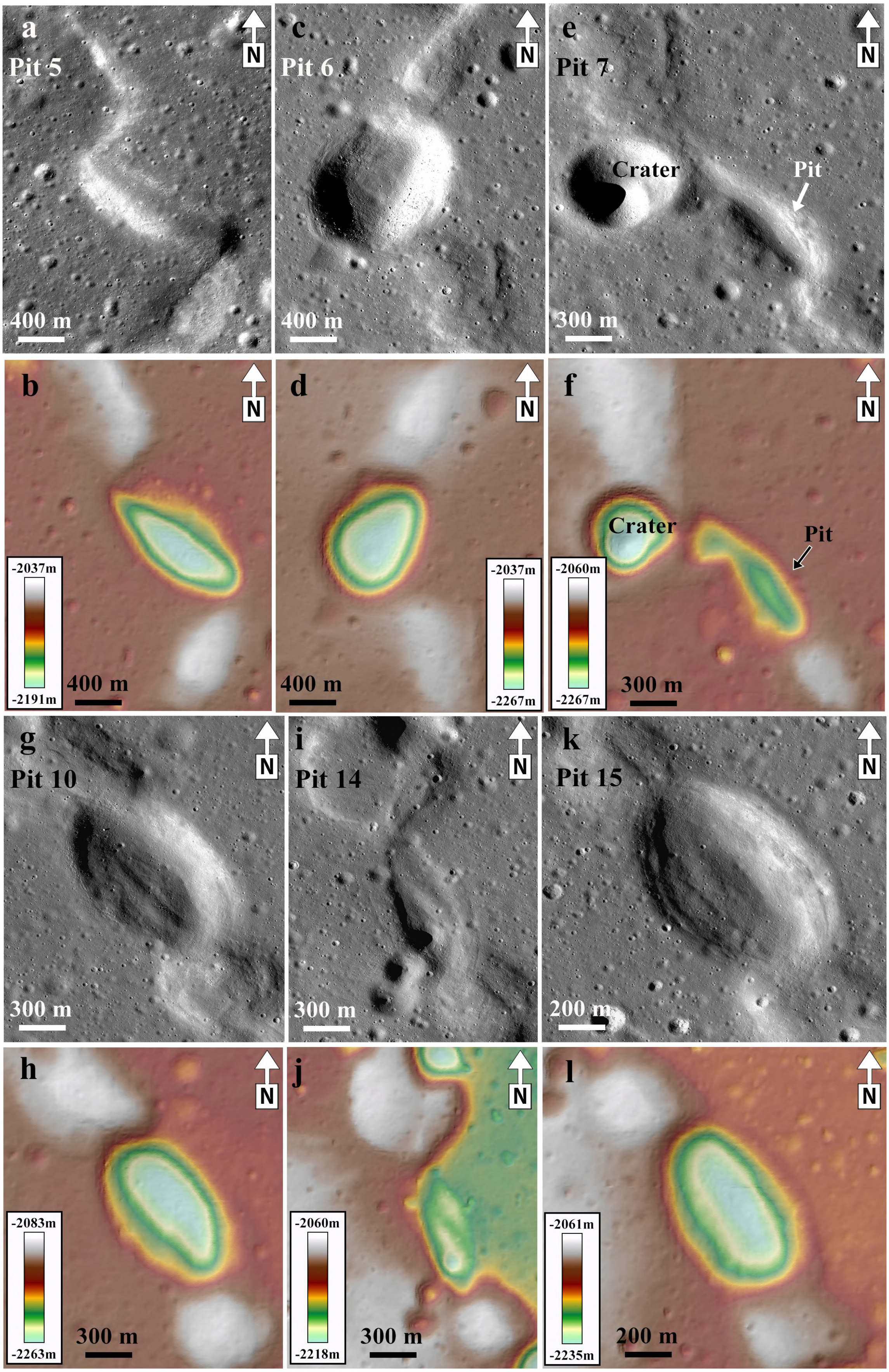

Figure AIII-5: Pits 5, 6, 7, 10, 14, and 15 with alternating collapses and raises shown in LROC–NAC images and NAC DTM.

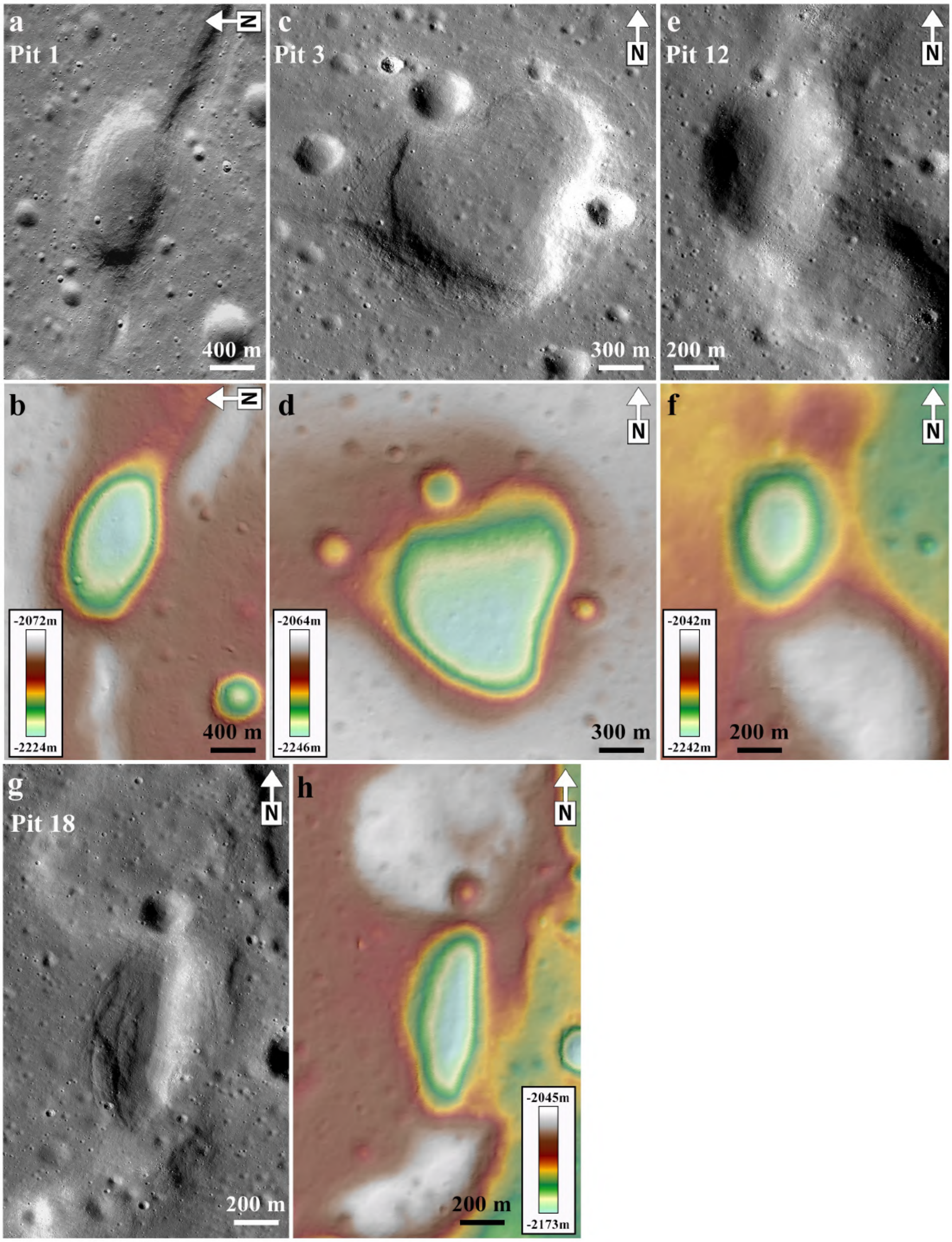

Figure AIII-6: Pits 1, 3, 12, and 18 have partially collapsed pits and raised features shown in LROC-NAC images and NAC DTM.

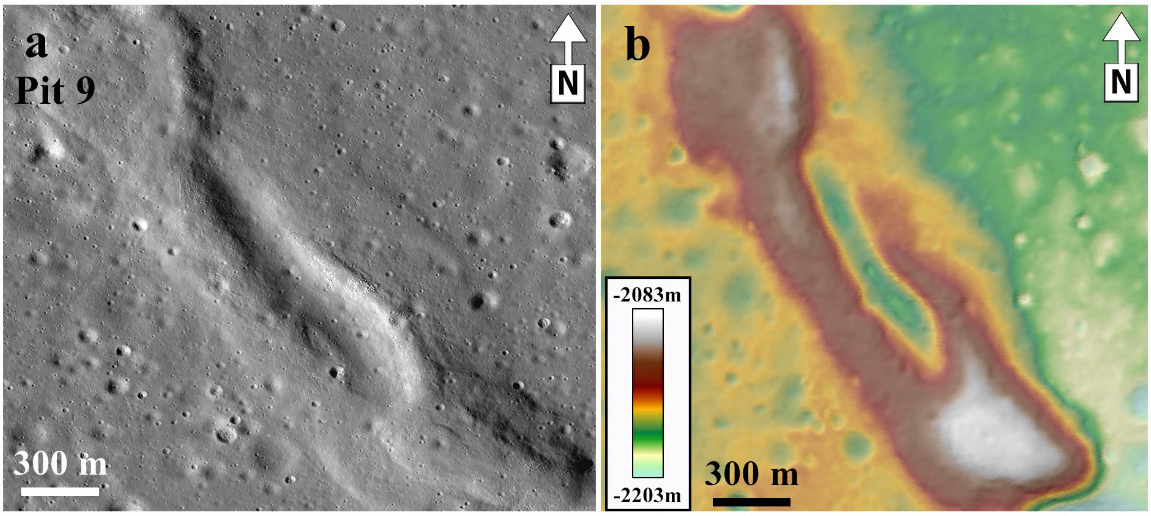

Figure AIII-7: Collapsed pit 9 surrounded by raised features shown in LROC-NAC images and NAC DTM.

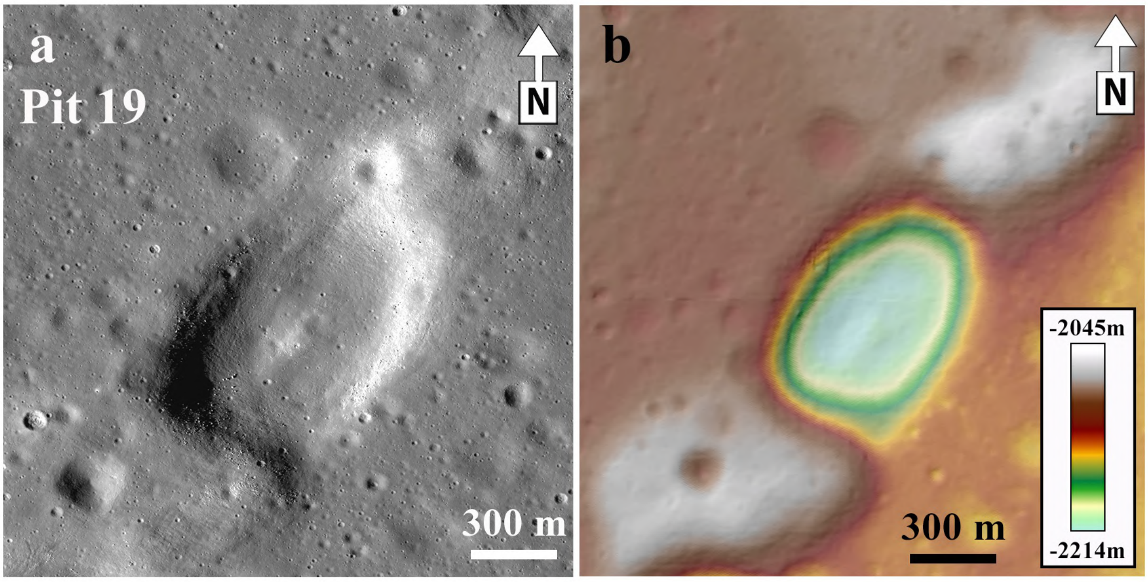

Figure AIII-8: Collapsed pit 19 with raised features at the centre shown in LROC-NAC images and NAC DTM.

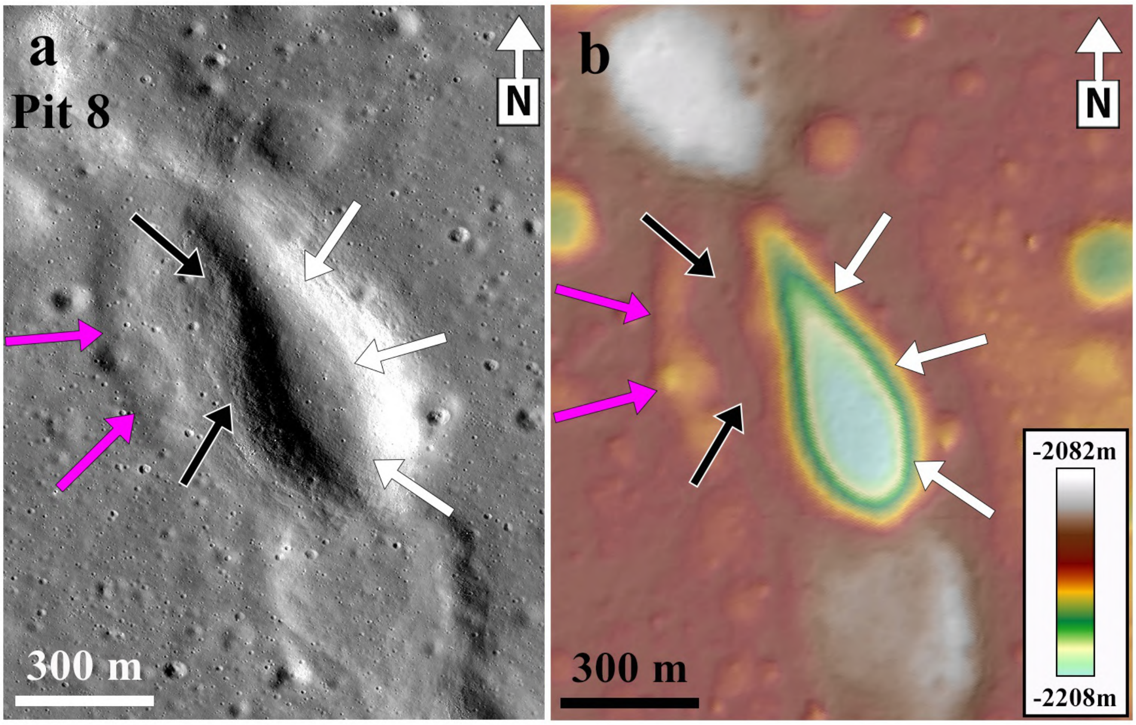

Figure AIII-9: Collapsed pit 8, with one side exhibiting a more pronounced collapse (white arrows) than the other half (pink arrows) shown in LROC-NAC images and NAC DTM.

Bibliography

Ai, H. (2006). *Shock-induced damage in rocks: Application to impact cratering*. California Institute of Technology.

Anderson, K. R., Johanson, I. A., Patrick, M. R., Gu, M., Segall, P., Poland, M. P., Montgomery-Brown, E. K., and Miklius, A. (2019). Magma reservoir failure and the onset of caldera collapse at kīlauea volcano in 2018. *Science*, 366(6470):eaaz1822.

Andrews-Hanna, J. C., Besserer, J., Head III, J. W., Howett, C. J., Kiefer, W. S., Lucey, P. J., McGovern, P. J., Melosh, H. J., Neumann, G. A., Phillips, R. J., et al. (2014). Structure and evolution of the lunar procellarum region as revealed by grail gravity data. *Nature*, 514(7520):68–71.

Andrews-Hanna, J. C., Head, J. W., Johnson, B. C., Keane, J. T., Kiefer, W. S., McGovern, P. J., Neumann, G. A., Wieczorek, M. A., and Zuber, M. T. (2018). Ring faults and ring dikes around the orientale basin on the moon. *Icarus*, 310:1–20.

Baker, D. M., Head, J. W., Fassett, C. I., Kadish, S. J., Smith, D. E., Zuber, M. T., and Neumann, G. A. (2011). The transition from complex crater to peak-ring basin on the moon: New observations from the lunar orbiter laser altimeter (lola) instrument. *Icarus*, 214(2):377–393.

Baldwin, R. B. (1971). On the history of lunar impact cratering: The absolute time scale and the origin of planetesimals. *Icarus*, 14(1):36–52.

Bamberg, M., Jaumann, R., Asche, H., Kneissl, T., and Michael, G. (2014). Floor-fractured craters on mars–observations and origin. *Planetary and Space Science*, 98:146–162.

Banks, M. E., Watters, T. R., Robinson, M. S., Tornabene, L. L., Tran, T., Ojha, L., and Williams, N. (2012). Morphometric analysis of small-scale lobate scarps on the moon using data from the lunar reconnaissance orbiter. *Journal of Geophysical Research: Planets*, 117(E12).

Barker, M., Mazarico, E., Neumann, G., Zuber, M., Haruyama, J., and Smith, D. (2016). A new lunar digital elevation model from the lunar orbiter laser altimeter and selene terrain camera. *Icarus*, 273:346–355.

Basilevskii, A. (1976). On the evolution rate of small lunar craters. In *In: Lunar Science Conference, 7th, Houston, Tex., March 15-19, 1976, Proceedings. Volume 1.(A77-34651 15-91) New York, Pergamon Press, Inc., 1976, p. 1005-1020.*, volume 7, pages 1005–1020.

Beck, A. R., Morgan, Z. T., Liang, Y., and Hess, P. C. (2006). Dunite channels as viable pathways for mare basalt transport in the deep lunar mantle. *Geophysical research letters*, 33(1).

Binder, A. B. and Lange, M. A. (1980). On the thermal history, thermal state, and related tectonism of a moon of fission origin. *Journal of Geophysical Research: Solid Earth*, 85(B6):3194–3208.

Blamont, J. (2014). A roadmap to cave dwelling on the moon and mars. *Advances in Space Research*, 54(10):2140–2149.

Braden, S., Stopar, J., Robinson, M., Lawrence, S., Van Der Bogert, C., and Hiesinger, H. (2014). Evidence for basaltic volcanism on the moon within the past 100 million years. *Nature Geoscience*, 7(11):787–791.

Bray, V. J., Collins, G. S., Morgan, J. V., and Schenk, P. M. (2008). The effect of target properties on crater morphology: Comparison of central peak craters on the moon and ganymede. *Meteoritics & Planetary Science*, 43(12):1979–1992.

Buczkowski, D. L., Sizemore, H. G., Bland, M. T., Scully, J. E., Quick, L. C., Hughson, K. H., Park, R. S., Preusker, F., Raymond, C. A., and Russell, C. T. (2018). Floor-fractured craters on ceres and implications for interior processes. *Journal of Geophysical Research: Planets*, 123(12):3188–3204.

Calvari, S. and Pinkerton, H. (1998). Formation of lava tubes and extensive flow field during the 1991–1993 eruption of mount etna. *Journal of Geophysical Research: Solid Earth*, 103(B11):27291–27301.

Carr, M. H. (1974). The role of lava erosion in the formation of lunar rilles and martian channels. *Icarus*, 22(1):1–23.

Chappaz, L., Sood, R., Melosh, H. J., Howell, K. C., Blair, D. M., Milbury, C., and Zuber, M. T. (2017). Evidence of large empty lava tubes on the moon using grail gravity. *Geophysical Research Letters*, 44(1):105–112.

Chowdhury, A. R., Patel, V. D., Joshi, S., Arya, A. S., Kumar, A., Paul, S., Shah, D., Soni, P., Karelia, J., Sampat, M., et al. (2020). Terrain mapping camera-2 onboard chandrayaan-2 orbiter. *Current Science*, 118(4):566–572.

Chwała, M., Komatsu, G., and Haruyama, J. (2024). Structural stability of lunar lava tubes with consideration of variable cross-section geometry. *Icarus*, 411:115928.

Cintala, M. J., Wood, C. A., and Head, J. W. (1977). The effects of target characteristics on fresh crater morphology-preliminary results for the moon and mercury. In *In: Lunar Science Conference, 8th, Houston, Tex., March 14-18, 1977, Proceedings. Volume 3.(A78-41551 18-91) New York, Pergamon Press, Inc., 1977, p. 3409-3425.*, volume 8, pages 3409–3425.

Clark, J., van der Bogert, C., Hiesinger, H., and Bernhardt, H. (2017). Wrinkle ridge-lobate scarp transition of west serenitatis: Indications for recent tectonic activity. In *48th Annual Lunar and Planetary Science Conference*, number 1964, page 1001.

Clark, J. D., Bernhardt, H., and Robinson, M. S. (2022). Extensional features at east serenitatis wrinkle ridge-lobate scarp transition indicate recent tectonic activity. Technical report, Copernicus Meetings.

Collins, G. C., McKinnon, W. B., Moore, J. M., Nimmo, F., Pappalardo, R. T., Prockter, L. M., and Schenk, P. M. (2009). Tectonics of the outer planet satellites. *Planetary tectonics*, 11(264):229.

Coombs, C. R. and Hawke, B. (1992). A search for intact lava tubes on the moon: Possible lunar base habitats. In *NASA. Johnson Space Center, The Second Conference on Lunar Bases and Space Activities of the 21st Century, Volume 1*, number HIG-CONTRIB-2165.

Cushing, G. E., Okubo, C. H., and Titus, T. N. (2015). Atypical pit craters on mars: New insights from themis, ctx, and hirise observations. *Journal of Geophysical Research: Planets*, 120(6):1023–1043.

Edwards, C., Bandfield, J., Christensen, P., and Rogers, A. (2014). The formation of infilled craters on mars: Evidence for widespread impact induced decompression of the early martian mantle? *Icarus*, 228:149–166.

French, B. M. (1998). Traces of catastrophe: A handbook of shock-metamorphic effects in terrestrial meteorite impact structures. Technical report.

French, R. A., Bina, C. R., Robinson, M. S., and Watters, T. R. (2015). Small-scale lunar graben: Distribution, dimensions, and formation processes. *Icarus*, 252:95–106.

Frueh, T., Clark, J., Hetzel, R., Hiesinger, H., and van der Bogert, C. (2022). Young compressional tectonic activity and associated formation of small graben on the moon. In *53rd Lunar and Planetary Science Conference*, volume 2678, page 1994.

Geshi, N., Ruch, J., and Acocella, V. (2014). Evaluating volumes for magma chambers and magma withdrawn for caldera collapse. *Earth and Planetary Science Letters*, 396:107–115.

Greeley, R. (1971). Lunar hadley rille: Considerations of its origin. *Science*, 172(3984):722–725.

Greenhagen, B. T., Neish, C. D., Williams, J.-P., Cahill, J. T., Ghent, R. R., Hayne, P. O., Lawrence, S. J., Petro, N. E., and Bandfield, J. L. (2016). Origin of the anomalously rocky appearance of tsiolkovskiy crater. *Icarus*, 273:237–247.

Hartmann, W. and Kuiper, G. P. (1962). Concentric structures surrounding lunar basins. *Communications of the Lunar and Planetary Laboratory*, 1:51–66.

Hartmann, W. K. (1973). Martian cratering, 4, mariner 9 initial analysis of cratering chronology. *Journal of Geophysical Research*, 78(20):4096–4116.

Hartmann, W. K. and Wood, C. A. (1971). Moon: Origin and evolution of multi-ring basins. *The moon*, 3(1):3–78.

Haruyama, J., Hioki, K., Shirao, M., Morota, T., Hiesinger, H., van der Bogert, C. H., Miyamoto, H., Iwasaki, A., Yokota, Y., Ohtake, M., et al. (2009). Possible lunar lava tube skylight observed by selene cameras. *Geophysical Research Letters*, 36(21).

Haruyama, J., Matsunaga, T., Ohtake, M., Morota, T., Honda, C., Yokota, Y., Torii, M., Ogawa, Y., and Group, L. W. (2008). Global lunar-surface mapping experiment using the lunar imager/spectrometer on selene. *Earth, planets and space*, 60:243–255.

Haruyama, J., Morota, T., Kobayashi, S., Sawai, S., Lucey, P. G., Shirao, M., and Nishino, M. N. (2012). Lunar holes and lava tubes as resources for lunar science and exploration. *Moon: Prospective Energy and Material Resources*, pages 139–163.

Havlin, C., Parmentier, E., and Hirth, G. (2013). Dike propagation driven by melt accumulation at the lithosphere–asthenosphere boundary. *Earth and Planetary Science Letters*, 376:20–28.

Head, J. (1975). Lunar mare deposits: Areas, volumes, sequence, and implication for melting in source areas. In *Origins of Mare Basalts and their Implications for Lunar Evolution*, volume 234, page 66.

Head, J. W. and Wilson, L. (2017). Generation, ascent and eruption of magma on the moon: New insights into source depths, magma supply, intrusions and effusive/explosive eruptions (part 2: Predicted emplacement processes and observations). *Icarus*, 283:176–223.

Head III, J. W. (1979). Serenitatis multi-ringed basin: Regional geology and basin ring interpretation. *The moon and the planets*, 21(4):439–462.

Heiken, G., Vaniman, D., and French, B. M. (1991). *Lunar sourcebook: A user's guide to the Moon*. Number 1259. Cup Archive.

Henriksen, M., Manheim, M., Burns, K., Seymour, P., Speyerer, E., Deran, A., Boyd, A., Howington-Kraus, E., Rosiek, M. R., Archinal, B. A., et al. (2017). Extracting accurate and precise topography from lroc narrow angle camera stereo observations. *Icarus*, 283:122–137.

Hiesinger, H., Head, J., Wolf, U., Jaumann, R., and Neukum, G. (2011). Ages and stratigraphy of lunar mare basalts: A synthesis. *Recent advances and current research issues in lunar stratigraphy*, 477:1–51.

Hiesinger, H., Head III, J., Wolf, U., Jaumann, R., and Neukum, G. (2003). Ages and stratigraphy of mare basalts in oceanus procellarum, mare nubium, mare cognitum, and mare insularum. *Journal of Geophysical Research: Planets*, 108(E7).

Hirabayashi, M., Minton, D. A., and Fassett, C. I. (2017). An analytical model of crater count equilibrium. *Icarus*, 289:134–143.

Hon, K., Kauahikaua, J., Denlinger, R., and Mackay, K. (1994). Emplacement and inflation of pahoehoe sheet flows: Observations and measurements of active lava flows on kilauea volcano, hawaii. *Geological Society of America Bulletin*, 106(3):351–370.

Hulme, G. (1973). Turbulent lava flow and the formation of lunar sinuous rilles. *Modern Geology*, 4:107–117.

Hurwitz, D. M., Head, J. W., and Hiesinger, H. (2013). Lunar sinuous rilles: Distribution, characteristics, and implications for their origin. *Planetary and Space Science*, 79:1–38.

Hurwitz, D. M., Head, J. W., Wilson, L., and Hiesinger, H. (2012). Origin of lunar sinuous rilles: Modeling effects of gravity, surface slope, and lava composition on erosion rates during the formation of rima prinz. *Journal of Geophysical Research: Planets*, 117(E12).

Ivanov, B. and Melosh, H. (2003). Impacts do not initiate volcanic eruptions: Eruptions close to the crater. *Geology*, 31(10):869–872.

Johnson, A. M. and Pollard, D. D. (1973). Mechanics of growth of some laccolithic intrusions in the henry mountains, utah, i: field observations, gilbert's model, physical properties and flow of the magma. *Tectonophysics*, 18(3-4):261–309.

Jozwiak, L., Head Iii, J., Neumann, G., and Wilson, L. (2017). Observational constraints on the identification of shallow lunar magmatism: Insights from floor-fractured craters. *Icarus*, 283:224–231.

Jozwiak, L. M., Head, J. W., and Wilson, L. (2015). Lunar floor-fractured craters as magmatic intrusions: Geometry, modes of emplacement, associated tectonic and volcanic features, and implications for gravity anomalies. *Icarus*, 248:424–447.

Jozwiak, L. M., Head, J. W., Zuber, M. T., Smith, D. E., and Neumann, G. A. (2012). Lunar floor-fractured craters: Classification, distribution, origin and implications for magmatism and shallow crustal structure. *Journal of Geophysical Research: Planets*, 117(E11).

Kaku, T., Haruyama, J., Miyake, W., Kumamoto, A., Ishiyama, K., Nishibori, T., Yamamoto, K., Crites, S. T., Michikami, T., Yokota, Y., et al. (2017). Detection of intact lava tubes at marius hills on the moon by selene (kaguya) lunar radar sounder. *Geophysical Research Letters*, 44(20):10–155.

Kimi, K., Vijayan, S., et al. (2023). Mare filled craters on the moon. *Icarus*, 390:115298.

Kneissl, T., van Gasselt, S., and Neukum, G. (2011). Map-projection-independent crater size-frequency determination in gis environments—new software tool for arcgis. *Planetary and Space Science*, 59(11-12):1243–1254.

Komatsu, G. and Baker, V. (1992). Venusian sinuous rilles. In *International Colloquium on Venus*, volume 789.

Krüger, T., Hergarten, S., and Kenkmann, T. (2018). Deriving morphometric parameters and the simple-to-complex transition diameter from a high-resolution, global database of fresh lunar impact craters (d˜ 3 km). *Journal of Geophysical Research: Planets*, 123(10):2667–2690.

Kumar, P. S. (2005). Structural effects of meteorite impact on basalt: Evidence from lonar crater, india. *Journal of Geophysical Research: Solid Earth*, 110(B12).

Kumar, P. S. and Kring, D. A. (2008). Impact fracturing and structural modification of sedimentary rocks at meteor crater, arizona. *Journal of Geophysical Research: Planets*, 113(E9).

Lu, Y., Wu, Y., Michael, G. G., Basilevsky, A. T., and Li, C. (2019). Young wrinkle ridges in mare imbrium: Evidence for very recent compressional tectonism. *Icarus*, 329:24–33.

Marsh, B. and Watts, A. (2007). Magmatism, magma, and magma chambers. *Treatise on Geophysics: Crust and Lithosphere Dynamics; Watts, AB, Ed*, pages 275–333.

Martellato, E., Foing, B., and Benkhoff, J. (2013). Numerical modelling of impact crater formation associated with isolated lunar skylight candidates on lava tubes. *Planetary and Space Science*, 86:33–44.

Maurice, M., Tosi, N., Schwinger, S., Breuer, D., and Kleine, T. (2020). A long-lived magma ocean on a young moon. *Science advances*, 6(28):eaba8949.

Mazarico, E., Rowlands, D., Neumann, G., Smith, D., Torrence, M., Lemoine, F., and Zuber, M. (2012). Orbit determination of the lunar reconnaissance orbiter. *Journal of Geodesy*, 86:193–207.

Melosh, H. (1978). The tectonics of mascon loading. In *In: Lunar and Planetary Science Conference, 9th, Houston, Tex., March 13-17, 1978, Proceedings. Volume 3.(A79-39253 16-91) New York, Pergamon Press, Inc., 1978, p. 3513-3525.*, volume 9, pages 3513–3525.

Melosh, H. (1980). Tectonic patterns on a tidally distorted planet. *Icarus*, 43(3):334–337.

Melosh, H. and Ivanov, B. (1999). Impact crater collapse. *Annual Review of Earth and Planetary Sciences*, 27(1):385–415.

Melosh, H. J. (1989). Impact cratering: A geologic process. *New York: Oxford University Press; Oxford: Clarendon Press*.

Meyer, H., Mahanti, P., Joshi, B., and Robinson, M. (2018). Quantifying the effect of slope on age determination for a single geologic event. *The First Billion Years: Bombardment*, 2107:2017.

Michael, G., Kneissl, T., and Neesemann, A. (2016). Planetary surface dating from crater size-frequency distribution measurements: Poisson timing analysis. *Icarus*, 277:279–285.

Michael, G. and Neukum, G. (2010). Planetary surface dating from crater size–frequency distribution measurements: Partial resurfacing events and statistical age uncertainty. *Earth and Planetary Science Letters*, 294(3-4):223–229.

Michael, G., Platz, T., Kneissl, T., and Schmedemann, N. (2012). Planetary surface dating from crater size–frequency distribution measurements: Spatial randomness and clustering. *Icarus*, 218(1):169–177.

Michaut, C. and Pinel, V. (2018). Magma ascent and eruption triggered by cratering on the moon. *Geophysical Research Letters*, 45(13):6408–6416.

Moore, H., Boyce, J., and Hahn, D. (1980). Small impact craters in the lunar regolith—their morphologies, relative ages, and rates of formation. *The moon and the planets*, 23:231–252.

Morota, T., Haruyama, J., Ohtake, M., Matsunaga, T., Honda, C., Yokota, Y., Kimura, J., Ogawa, Y., Hirata, N., Demura, H., et al. (2011). Timing and characteristics of the latest mare eruption on the moon. *Earth and Planetary Science Letters*, 302(3-4):255–266.

Nahm, A. L., Oehman, T., and Kring, D. A. (2013). Normal faulting origin for the cordillera and outer rook rings of orientale basin, the moon. *Journal of Geophysical Research: Planets*, 118(2):190–205.

Nelson, D., Koeber, S., Daud, K., Robinson, M., Watters, T., Banks, M., and Williams, N. (2014). Mapping lunar maria extents and lobate scarps using lroc image products. In *45th annual lunar and planetary science conference*, number 1777, page 2861.

Neukum, G. (1983). Meteoritenbombardement und datierung planetarer oberflachen. *Habilitation Dissertation for Faculty Membership, Ludwig-Maximilians-Univ.*

Neukum, G. (1984). Meteorite bombardment and dating of planetary surfaces. Technical report.

Neukum, G. and Horn, P. (1976). Effects of lava flows on lunar crater populations. *The Moon*, 15(3):205–222.

Neukum, G., Ivanov, B. A., and Hartmann, W. K. (2001). Cratering records in the inner solar system in relation to the lunar reference system. In *Chronology and Evolution of Mars: Proceedings of an ISSI Workshop, 10–14 April 2000, Bern, Switzerland*, pages 55–86. Springer.

Neukum, G., König, B., and Arkani-Hamed, J. (1975). A study of lunar impact crater size-distributions. *The moon*, 12(2):201–229.

Neukum, G. and Wise, D. (1976). Mars: A standard crater curve and possible new time scale: Cratering links to lunar time suggest that mars died long ago. *Science*, 194(4272):1381–1387.

Neumann, G., Smith, D., Scott, S., Slavney, S., and Grayzek, E. (2011). Lunar reconnaissance orbiter lunar orbiter laser altimeter reduced data record and derived products software interface specification, version 2.42. *National Aeronautics and Space Administration Planetary Data System. https://lunar. gsfc. nasa. gov/lol a/images/LOLA_RDRSIS. pdf.(Accessed 20 August 2021).*

Neumann, G. A., Zuber, M. T., Wieczorek, M. A., Head, J. W., Baker, D. M., Solomon, S. C., Smith, D. E., Lemoine, F. G., Mazarico, E., Sabaka, T. J., et al. (2015). Lunar impact basins revealed by gravity recovery and interior laboratory measurements. *Science advances*, 1(9):e1500852.

Nypaver, C. A. and Thomson, B. J. (2022). New observations of recently active wrinkle ridges in the lunar mare: Implications for the timing and origin of lunar tectonics. *Geophysical Research Letters*, 49(17):e2022GL098975.

Osinski, G. R. and Pierazzo, E. (2013). Impact cratering: Processes and products. *Impact Cratering*, pages 1–20.

Pasckert, J. H., Hiesinger, H., and van der Bogert, C. H. (2015). Small-scale lunar farside volcanism. *Icarus*, 257:336–354.

Pasckert, J. H., Hiesinger, H., and van der Bogert, C. H. (2018). Lunar farside volcanism in and around the south pole–aitken basin. *Icarus*, 299:538–562.

Peterson, D. W., Holcomb, R. T., Tilling, R. I., and Christiansen, R. L. (1994). Development of lava tubes in the light of observations at mauna ulu, kilauea volcano, hawaii. *Bulletin of Volcanology*, 56:343–360.

Pike, R. J. (1974). Depth/diameter relations of fresh lunar craters: Revision from spacecraft data. *Geophysical Research Letters*, 1(7):291–294.

Pike, R. J. (1977). Size-dependence in the shape of fresh impact craters on the moon. In *Impact and explosion cratering: Planetary and terrestrial implications*, pages 489–509.

Plescia, J. and Golombek, M. (1986). Origin of planetary wrinkle ridges based on the study of terrestrial analogs. *Geological Society of America Bulletin*, 97(11):1289–1299.

Polanskey, C. A. and Ahrens, T. J. (1990). Impact spallation experiments: Fracture patterns and spall velocities. *Icarus*, 87(1):140–155.

Richter, F. M. and McKenzie, D. (1984). Dynamical models for melt segregation from a deformable matrix. *The Journal of Geology*, 92(6):729–740.

Robbins, S. J. (2019). A new global database of lunar impact craters¿ 1–2 km: 1. crater locations and sizes, comparisons with published databases, and global analysis. *Journal of Geophysical Research: Planets*, 124(4):871–892.

Robinson, M., Ashley, J., Boyd, A., Wagner, R., Speyerer, E., Hawke, B. R., Hiesinger, H., and Van Der Bogert, C. (2012). Confirmation of sublunarean voids and thin layering in mare deposits. *Planetary and Space Science*, 69(1):18–27.

Robinson, M. S., Brylow, S., Tschimmel, M. e., Humm, D., Lawrence, S., Thomas, P., Denevi, B. W., Bowman-Cisneros, E., Zerr, J., Ravine, M., et al. (2010). Lunar reconnaissance orbiter camera (lroc) instrument overview. *Space science reviews*, 150:81–124.

Salem, I. B., Sharma, M., Kumaresan, P., Karthi, A., Howari, F. M., Nazzal, Y., and Xavier, C. M. (2022). An investigation on the morphological and mineralogical characteristics of posidonius floor fractured lunar impact crater using lunar remote sensing data. *Remote Sensing*, 14(4):814.

Sauro, F., Pozzobon, R., Massironi, M., De Berardinis, P., Santagata, T., and De Waele, J. (2020). Lava tubes on earth, moon and mars: A review on their size and morphology revealed by comparative planetology. *Earth-Science Reviews*, 209:103288.

Schultz, P. and Orphal, D. (1978). Floor-fractured craters on the moon and mars. In *Meteoritical Society, Annual Meeting, 41st, Sudbury, Ontario, Canada, Aug. 14-17, 1978. Meteoritics, vol. 13, Dec. 31, 1978, p. 622-625. Abridged.*, volume 13, pages 622–625.

Schultz, P. H. (1976). Floor-fractured lunar craters. *The Moon*, 15(3):241–273.

Schultz, P. H., Staid, M. I., and Pieters, C. M. (2006). Lunar activity from recent gas release. *Nature*, 444(7116):184–186.

Schultz, R. A. (2000). Localization of bedding plane slip and backthrust faults above blind thrust faults: Keys to wrinkle ridge structure. *Journal of Geophysical Research: Planets*, 105(E5):12035–12052.

Senft, L. E. and Stewart, S. T. (2007). Modeling impact cratering in layered surfaces. *Journal of Geophysical Research: Planets*, 112(E11).

Shearer, C. K., Hess, P. C., Wieczorek, M. A., Pritchard, M. E., Parmentier, E. M., Borg, L. E., Longhi, J., Elkins-Tanton, L. T., Neal, C. R., Antonenko, I., et al. (2006). Thermal and magmatic evolution of the moon. *Reviews in Mineralogy and Geochemistry*, 60(1):365–518.

Shirley, K., Zanetti, M., Jolliff, B. v., van Der Bogert, C., and Hiesinger, H. (2016). Crater size-frequency distribution measurements and age of the compton–belkovich volcanic complex. *Icarus*, 273:214–223.

Silber, E. A., Osinski, G. R., Johnson, B. C., and Grieve, R. A. (2017). Effect of impact velocity and acoustic fluidization on the simple-to-complex transition of lunar craters. *Journal of Geophysical Research: Planets*, 122(5):800–821.

Smith, D. E., Zuber, M. T., Jackson, G. B., Cavanaugh, J. F., Neumann, G. A., Riris, H., Sun, X., Zellar, R. S., Coltharp, C., Connelly, J., et al. (2010a). The lunar orbiter laser altimeter investigation on the lunar reconnaissance orbiter mission. *Space science reviews*, 150:209–241.

Smith, D. E., Zuber, M. T., Neumann, G. A., Lemoine, F. G., Mazarico, E., Torrence, M. H., McGarry, J. F., Rowlands, D. D., Head III, J. W., Duxbury, T. H., et al. (2010b). Initial observations from the lunar orbiter laser altimeter (lola). *Geophysical Research Letters*, 37(18).

Solomon, S. C. (1978). On volcanism and thermal tectonics on one-plate planets. *Geophysical Research Letters*, 5(6):461–464.

Solomon, S. C. and Chaiken, J. (1976). Thermal expansion and thermal stress in the moon and terrestrial planets-clues to early thermal history. In *In: Lunar Science Conference, 7th, Houston, Tex., March 15-19, 1976, Proceedings. Volume 3.(A77-34651 15-91) New York, Pergamon Press, Inc., 1976, p. 3229-3243.*, volume 7, pages 3229–3243.

Solomon, S. C. and Head, J. W. (1979). Vertical movement in mare basins: Relation to mare emplacement, basin tectonics, and lunar thermal history. *Journal of Geophysical Research: Solid Earth*, 84(B4):1667–1682.

Solomon, S. C. and Head, J. W. (1980). Lunar mascon basins: Lava filling, tectonics, and evolution of the lithosphere. *Reviews of Geophysics*, 18(1):107–141.

Solomon, S. C. and Longhi, J. (1977). Magma oceanography. i-thermal evolution. In *In: Lunar Science Conference, 8th, Houston, Tex., March 14-18, 1977, Proceedings. Volume 1.(A78-41551 18-91) New York, Pergamon Press, Inc., 1977, p. 583-599.*, volume 8, pages 583–599.

Speyerer, E., Robinson, M., Denevi, B., Team, L. S., et al. (2011). Lunar reconnaissance orbiter camera global morphological map of the moon. In *42nd annual lunar and planetary science conference*, number 1608, page 2387.

Spudis, P. D. (1993). *The geology of multi-ring impact basins*.

Spudis, P. D., Swann, G. A., and Greeley, R. (1988). The formation of hadley rille and implications for the geology of the apollo 15 region. In *IN: Lunar and Planetary Science Conference, 18th, Houston, TX, Mar. 16-20, 1987, Proceedings (A89-10851 01-91). Cambridge and New York/Houston, TX, Cambridge University Press/Lunar and Planetary Institute, 1988, p. 243-254. NASA-supported research.*, volume 18, pages 243–254.

Strain, P. L. and El Baz, F. (1980). The geology and morphology of ina.

Theinat, A. K., Modiriasari, A., Bobet, A., Melosh, H. J., Dyke, S. J., Ramirez, J., Maghareh, A., and Gomez, D. (2020). Lunar lava tubes: Morphology to structural stability. *Icarus*, 338:113442.

Thesniya, P., Rajesh, V., and Flahaut, J. (2020). Ages and chemistry of mare basaltic units in the grimaldi basin on the nearside of the moon: Implications for the volcanic history of the basin. *Meteoritics & Planetary Science*, 55(11):2375–2403.

Thompson, T., Robinson, M., Watters, T., and Johnson, M. (2017). Global lunar wrinkle ridge identification and analysis. In *48th Annual Lunar and Planetary Science Conference*, number 1964, page 2665.

Thorey, C. and Michaut, C. (2014). A model for the dynamics of crater-centered intrusion: Application to lunar floor-fractured craters. *Journal of Geophysical Research: Planets*, 119(1):286–312.

Tonello, M. (2017). Origin and evolution of an inflated lava tube between the mio-pliocene volcanic complex of famara and the quaternary lava flows of la corona in lanzarote.

Trask, N. (1971). Geologic comparison of mare materials in the lunar equatorial belt, including apollo 11 and apollo 12 landing sites. *US Geol. Surv. Prof. Pap., 750D*, pages 2645–2662.

Valantinas, A. and Schultz, P. (2020). The origin of neotectonics on the lunar nearside. *Geology*, 48(7):649–653.

Van Der Bogert, C. H., Clark, J. D., Hiesinger, H., Banks, M. E., Watters, T. R., and Robinson, M. S. (2018). How old are lunar lobate scarps? 1. seismic resetting of crater size-frequency distributions. *Icarus*, 306:225–242.

Wagner, R. V. and Robinson, M. S. (2014). Distribution, formation mechanisms, and significance of lunar pits. *Icarus*, 237:52–60.

Walwer, D., Michaut, C., Pinel, V., and Adda-Bedia, M. (2021). Magma ascent and emplacement below floor fractured craters on the moon from floor uplift and fracture length. *Physics of the Earth and Planetary Interiors*, 312:106658.

Watters, T. R. (1993). Compressional tectonism on mars. *Journal of Geophysical Research: Planets*, 98(E9):17049–17060.

Watters, T. R. (2022). Lunar wrinkle ridges and the evolution of the nearside lithosphere. *Journal of Geophysical Research: Planets*, 127(3):e2021JE007058.

Watters, T. R. and Robinson, M. S. (1997). Radar and photoclinometric studies of wrinkle ridges on mars. *Journal of Geophysical Research: Planets*, 102(E5):10889–10903.

Watters, T. R., Robinson, M. S., Banks, M. E., Tran, T., and Denevi, B. W. (2012). Recent extensional tectonics on the moon revealed by the lunar reconnaissance orbiter camera. *Nature Geoscience*, 5(3):181–185.

Watters, T. R., Robinson, M. S., Beyer, R. A., Banks, M. E., Bell III, J. F., Pritchard, M. E., Hiesinger, H., Van Der Bogert, C. H., Thomas, P. C., Turtle, E. P., et al. (2010). Evidence of recent thrust faulting on the moon revealed by the lunar reconnaissance orbiter camera. *Science*, 329(5994):936–940.

Watters, T. R., Robinson, M. S., Collins, G. C., Banks, M. E., Daud, K., Williams, N. R., and Selvans, M. M. (2015). Global thrust faulting on the moon and the influence of tidal stresses. *Geology*, 43(10):851–854.

Watters, T. R., Weber, R. C., Collins, G. C., Howley, I. J., Schmerr, N. C., and Johnson, C. L. (2019). Shallow seismic activity and young thrust faults on the moon. *Nature Geoscience*, 12(6):411–417.

Wessel, P., Smith, W. H., Scharroo, R., Luis, J., and Wobbe, F. (2013). Generic mapping tools: improved version released. *Eos, Transactions American Geophysical Union*, 94(45):409–410.

Whitten, J., Head, J. W., Staid, M., Pieters, C. M., Mustard, J., Clark, R., Nettles, J., Klima, R. L., and Taylor, L. (2011). Lunar mare deposits associated with the orientale impact basin: New insights into mineralogy, history, mode of emplacement, and relation to orientale basin evolution from moon mineralogy mapper (m3) data from chandrayaan-1. *Journal of Geophysical Research: Planets*, 116(E6).

Wichman, R. and Schultz, P. (1993). Floor-fractured crater models of the sudbury structure, canada: Implications for initial crater size and crater modification. *Meteoritics*, 28(2):222–231.

Wichman, R. and Schultz, P. (1995). Floor-fractured craters in mare smythii and west of oceanus procellarum: Implications of crater modification by viscous relaxation and igneous intrusion models. *Journal of Geophysical Research: Planets*, 100(E10):21201–21218.

Wieczorek, M. A., Neumann, G. A., Nimmo, F., Kiefer, W. S., Taylor, G. J., Melosh, H. J., Phillips, R. J., Solomon, S. C., Andrews-Hanna, J. C., Asmar, S. W., et al. (2013). The crust of the moon as seen by grail. *Science*, 339(6120):671–675.

Wieczorek, M. A., Zuber, M. T., and Phillips, R. J. (2001). The role of magma buoyancy on the eruption of lunar basalts. *Earth and Planetary Science Letters*, 185(1-2):71–83.

Williams, D. A., Fagents, S. A., and Greeley, R. (2000). A reassessment of the emplacement and erosional potential of turbulent, low-viscosity lavas on the moon. *Journal of Geophysical Research: Planets*, 105(E8):20189–20205.

Williams, N., Watters, T. R., Pritchard, M., Banks, M. E., and Bell III, J. (2013). Fault dislocation modeled structure of lobate scarps from lunar reconnaissance orbiter camera digital terrain models. *Journal of Geophysical Research: Planets*, 118(2):224–233.

Williams, N. R., Bell III, J. F., Watters, T. R., Banks, M. E., Daud, K., and French, R. A. (2019). Evidence for recent and ancient faulting at mare frigoris and implications for lunar tectonic evolution. *Icarus*, 326:151–161.

Wilson, L. and Head, J. W. (2017). Generation, ascent and eruption of magma on the moon: New insights into source depths, magma supply, intrusions and effusive/explosive eruptions (part 1: Theory). *Icarus*, 283:146–175.

Wilson, L. and Head, J. W. (2018). Lunar floor-fractured craters: Modes of dike and sill emplacement and implications of gas production and intrusion cooling on surface morphology and structure. *Icarus*, 305:105–122.

Wilson, L. and Head III, J. W. (1981). Ascent and eruption of basaltic magma on the earth and moon. *Journal of Geophysical Research: Solid Earth*, 86(B4):2971–3001.

Wyrick, D., Ferrill, D. A., Morris, A. P., Colton, S. L., and Sims, D. W. (2004). Distribution, morphology, and origins of martian pit crater chains. *Journal of Geophysical Research: Planets*, 109(E6).

Zhang, F., Pizzi, A., Ruj, T., Komatsu, G., Yin, A., Dang, Y., Liu, Y., and Zou, Y. (2023). Evidence for structural control of mare volcanism in lunar compressional tectonic settings. *Nature Communications*, 14(1):2892.

Zhu, K., Yang, M., Yan, X., Li, W., Feng, W., and Zhong, M. (2024). Grail gravity gradients evidence for a potential lava tube at marius hills on the moon. *Icarus*, 408:115814.